

Direct Numerical Simulation of Turbulent Flow and Heat Transfer in a Concentric Annular Pipe

by

Edris Bagheri

A thesis
presented to the University of Manitoba
in partial fulfilment of the
thesis requirement for the degree of
Doctor of Philosophy
in
Mechanical Engineering

Winnipeg, Manitoba, Canada 2021

June 2021

©Edris Bagheri 2021

Abstract

In this thesis, the effects of computational domain size and radius ratio on fully developed turbulent flow and heat transfer in a concentric annular pipe are investigated using direct numerical simulation (DNS). To perform DNS, a new parallel computer code based on the pseudo-spectral method was developed using the FORTRAN 90/95 programming language and the message passing interface (MPI) libraries .

In order to study the effects of computational domain size on the turbulence statistics, twelve test cases ($L_\theta = \pi/6-2\pi$ and $L_z = \pi\delta-30\pi\delta$) of different domain sizes are compared. The effects of radius ratio are investigated through a systematic comparative study of four radius ratios of a concentric pipe (for $R_i/R_o = 0.1-0.7$). The characteristics of the velocity and temperature fields are examined at two Reynolds number of $Re_{D_h} = 8900$ and 17700 . Here, R_i and R_o are the radii of the inner and outer pipes, respectively, and D_h is the hydraulic diameter. The radius ratio affects the interaction between the two boundary layers of the concentric annular pipe, and has a significant impact on turbulent flow structures and dynamics. The characteristics of the flow and temperature fields are investigated in both physical and spectral spaces, which include the analyses of the first- and second-order statistical moments, budget balance of the transport equation of Reynolds stresses, two-point correlation coefficients, premultiplied spectra of velocity, vorticity, and temperature fluctuations. It is observed that the scales and dynamics of turbulence structures vary with the radius ratio as well as the surface curvature of the concave and convex walls. The characteristic length scales of the turbulence structures are identified precisely through a spectral analysis.

Acknowledgments

I would like to express my gratitude to my supervisor, Professor Bing-Chen Wang, who guided me throughout this program. I would also like to thank my committee members, Professor Scott Ormiston and Professor Ian Jeffrey for their advice. I thank my friends and fellows in the research group of Professor Wang for the stimulating discussions and for the friendly time during my Ph.D. program. Last but not the least, I would like to thank my parents, Hemmat Bagheri and Soror Amini-Rad, for their unconditional love and support.

Contents

Abstract	ii
Acknowledgments	iii
Table of Contents	vi
List of Tables	vii
List of Figures	ix
Nomenclature	xx
1 Introduction	1
1.1 Background and motivation	1
1.2 Literature review	2
1.2.1 Influence of domain size on direct numerical simulation of turbulent flow in a moderately-curved concentric annular pipe	3
1.2.2 The effects of radius ratio on turbulent concentric annular pipe flow and structures	5
1.2.3 The effects of radius ratio on turbulent heat transfer in concentric annular pipe flows	6
1.3 Objectives	8
1.4 Outlines of the proposed thesis	8
2 Influence of Domain Size on Direct Numerical Simulation of Turbulent Flow in a Moderately-Curved Concentric Annular Pipe	10
2.1 Test case and numerical algorithm	12

2.2	Turbulence statistics in physical space	17
2.2.1	Mean velocity	17
2.2.2	Reynolds stresses	20
2.2.3	Higher-order statistics	25
2.2.4	Two-point correlation	29
2.3	Turbulence structures and spectral analysis	31
2.3.1	Scales of hairpin structures and near-wall streaks	31
2.3.2	Axial premultiplied energy spectra	40
2.3.3	Azimuthal premultiplied energy spectra	47
3	The Effects of Radius Ratio on Turbulent Concentric Annular Pipe Flow and Structures	53
3.1	Test cases and numerical algorithm	54
3.2	Results and discussions	57
3.2.1	Computational domain sizes	57
3.2.2	Flow statistics	65
3.2.3	Interaction of the inner and outer boundary layers	71
3.3	Turbulence structures	76
4	Direct Numerical Simulation of Turbulent Heat Transfer in Concentric Annular Pipe Flows	83
4.1	Test cases and numerical algorithm	84
4.1.1	Justification of domain size for DNS of turbulent heat transfer	88
4.2	Results and discussions	91
4.2.1	Temperature statistics	91
4.2.2	Interaction of the inner and outer thermal boundary layers . .	96
4.2.3	Budget balance of transport equations	97
4.3	Coherent structures associated with the temperature field	103

5	Conclusions and Future Work	109
5.1	Conclusions	109
5.1.1	Influence of domain size on DNS of turbulent flow in a moderately-curved concentric annular pipe	109
5.1.2	The effects of radius ratio on turbulent concentric annular pipe flow and structures	112
5.1.3	Direct numerical simulation of turbulent heat transfer in concentric annular pipe flows	114
5.2	Future work	116
	Bibliography	123
A	Computer Code and Numerical Algorithm	124
A.1	Test cases and numerical algorithm	125
A.2	Spatial discretization	127
A.3	Temporal discretization	128
A.4	Implementation of boundary conditions	131
A.5	Validation based on concentric annular pipe with $R_i/R_o = 0.5$	133
A.6	Implementation of the P3DFFT library	135
A.7	Scalability of the code	139

List of Tables

2.1	Summary of test cases and grid resolutions. The nominal Reynolds number is $Re_{D_h} = 8900$ for the A-, B- and C-series test cases, and is $Re_{D_h} = 17700$ for case D.	12
2.2	Mean flow parameters calculated from DNS.	16
3.1	Summary of four test cases of different radius ratios and grid resolutions associated with each case. Here, $\delta = (R_o - R_i)/2$ is one half the cylinder gap.	57
3.2	Mean flow parameters of all four test cases of different radius ratios. .	65
4.1	Summary of test cases, grid resolutions, wall friction velocity [m/s] and friction temperature [°C].	87
4.2	Mean temperature field parameters of all four test cases of different radius ratios.	90
4.3	Budget terms of transport Eq. (4.25) for temperature variance k_Θ , axial turbulent heat flux $\langle u'_z \Theta' \rangle$, and radial turbulent heat flux $\langle u'_r \Theta' \rangle$	98
5.1	Summary of the minimum computational domain sizes required for performing DNS for accurate calculations of different types of turbulence statistics at the nominal Reynolds number of $Re_{D_h} = 8900$	110
A.1	Scheme coefficient.	129

A.2	Summary of test cases and grid resolutions. The nominal Reynolds number is $Re_{D_h} = 8900$ for the C and Ca test cases.	134
A.3	Arguments of <code>p3dfft_setup</code>	137
A.4	Arguments of <code>p3dfft_get_dims(start, end, size, ip)</code>	138
A.5	Arguments of <code>p3dfft_ftran_r2c (in, out, opt)</code>	139
A.6	Arguments of <code>p3dfft_ftran_c2r (in, out, opt)</code>	139

List of Figures

2.1	Computational domain and coordinate system.	11
2.2	Cross-sectional view of the mesh for case B4.	14
2.3	Profiles of the mean axial velocity $\langle u_z \rangle^+$. (a) in global coordinate for A-, B-, C- and D-series test cases, and (b) in wall coordinate for cases A6 and D. To facilitate the comparison of cases of the lower nominal Reynolds number, their profiles are partially enlarged and shown in an inset graph in (a).	19
2.4	Profiles of Reynolds stresses $\langle u'_i u'_j \rangle^+$ predicted based on various computational domain sizes of the A-series test cases in comparison with those of the C- and D-series test cases. (a) $\langle u'_z u'_z \rangle^+$, (b) $\langle u'_\theta u'_\theta \rangle^+$, (c) $\langle u'_r u'_r \rangle^+$, and (d) $\langle u'_z u'_r \rangle^+$	21
2.5	Profiles of Reynolds stresses $\langle u'_i u'_j \rangle^+$ predicted based on various computational domain sizes of the A-series test cases in comparison with those of the C- and D-series test cases. (a) $\langle u'_z u'_z \rangle^+$, (b) $\langle u'_\theta u'_\theta \rangle^+$, (c) $\langle u'_r u'_r \rangle^+$, and (d) $\langle u'_z u'_r \rangle^+$	22

2.6	Profiles of the mean axial velocity $\langle u_z \rangle$ and budget balance of total shear stress ($\tau_{\text{tot}} = \tau_{\text{vis}} + \tau_{\text{tur}}$) displayed in the global coordinate based on the DNS results of case A6. Considering the large differences in their absolute magnitudes, the mean axial velocity $\langle u_z \rangle$ is non-dimensionalized using the bulk mean velocity U_b , while the shear stresses are non-dimensionalized based on the mean wall friction velocity u_τ	25
2.7	Skewness factors of the velocity field on the convex and concave sides of the concentric annular pipe for cases A6 and D. (a) convex side, and (b) concave side. The vertical dashed lines demarcate the zero-crossing points of the skewness factors for $S(u'_z) = 0$ and $S(u'_r) = 0$. Near-wall regions featuring the sweeping and ejection events are labeled using “S” and “E”, in either green or black color corresponding to either case A6 or D, respectively. The skewness factor of the ideal Gaussian distribution is also plotted using a thin dashed line, which is $S(u'_i) \equiv 0$	26
2.8	Flatness factors of the velocity field on the convex and concave sides of the concentric annular pipe for cases A6 and D. (a) convex side, and (b) concave side. The flatness factor of the ideal Gaussian distribution is also plotted using a thin dashed line, which is $F(u'_i) \equiv 3$	27
2.9	Profiles of normalized two-point correlation coefficient R_{zz} of the axial velocity fluctuations (u'_z) calculated over the cylindrical surface located at $r^+ = 15$ from the convex and concave walls, where the Reynolds normal stress $\langle u'_z u'_z \rangle$ reaches its peak value. (a) axial correlations for A- and D-series test cases (convex side), (b) axial correlations for A- and D-series test cases (concave side), (c) azimuthal correlations for B- and D-series test cases (convex side), and (d) azimuthal correlations for B- and D-series test cases (concave side).	29

2.10 Contours of the non-dimensionalized axial velocity fluctuations $u_z'^+$ of case B4, plotted at $r^+ = 15$ on the convex and concave sides, where the maximum TKE occurs. (a) convex side, and (b) concave side. The contours are colored using the magnitude of the instantaneous axial velocity fluctuations $u_z'^+$. To enhance the visual clarity of near-wall structures, only a portion of the computational domain of case B4 is plotted. The plotted domain sizes are $L_z = 6\pi\delta$ and $L_\theta = \pi/2$ 32

2.11 Premultiplied 2D spectra $k_z^+ k_\theta^+ \check{E}_{zz}^+$ of axial velocity fluctuations on the convex and concave sides of the concentric annular pipe for case B4, which vary with the axial and azimuthal wavelengths. (a) $r^+ = 15$ on the convex side, (b) $r^+ = 15$ on the concave side, (c) $(R - r)/\delta = 0.5$ on the convex side, and (d) $(R - r)/\delta = 0.5$ on the concave side. In each figure panel, the wavelength is given both as λ_z^+ (bottom) and as λ_z/δ (top). Similarly, the azimuthal coordinate is given both as λ_θ^+ (left) and as λ_θ/δ (right). The computational domain of case B4 (i.e., $L_z = 12\pi\delta$ and $L_\theta = 3\pi/4$) are shown as the boundaries in Fig. 2.11. For the purpose of comparison, smaller axial and azimuthal domain sizes used in other test cases are also labeled in the figure. The figure presentations are made at two radial positions: close to the wall at $r^+ = 15$, where $\langle u_z' u_z' \rangle^+$ peaks; and at one quarter the cylinder gap (or, $\delta/2$) away from the wall (i.e., $(R - r)/2 = 0.5$ from the convex wall or $(r - R)/2 = 0.5$ from the concave wall). Three energy levels are distinguished, and the innermost, intermediate and outermost isopleths correspond to $0.875 \max(k_z^+ k_\theta^+ \check{E}_{ii}^+)$, $0.625 \max(k_z^+ k_\theta^+ \check{E}_{ii}^+)$ and $0.375 \max(k_z^+ k_\theta^+ \check{E}_{ii}^+)$, respectively. 34

- 2.12 Contours of swirling strength ($\lambda_{ci} = 1.0$) for case B4. (a) convex side, and (b) concave side. The contours are colored with instantaneous axial vorticity $\omega_z'^+$. To enhance the visual clarity of near-wall structures, only a portion of the computational domain is plotted for $L_z = 6\pi\delta$ and $L_\theta = \pi/2$ 38
- 2.13 Side view of hairpin structures on the concave side of the concentric pipe for case B4. (a) contours of the swirling strength of $\lambda_{ci} = 1.0$ colored using the strength of $\omega_z'^+$, (b) contours of conditional averaging of axial velocity fluctuations $\langle u_z'^+ | Q2 \rangle$ in the z - r plane located at $\theta = 0^\circ$. In panel (a), the hairpin structures are obtained by projecting the selected domain from Fig. 2.12(b) (indicated using a 3D green box) into a 2D z - r plane here. The green and black dashed lines in panel (a) show the positions of the PHV and SHV, respectively. The wavelength of both PHV and SHV is approximately $\lambda_z^+ = 400$ 39
- 2.14 Contours of premultiplied 1D axial energy spectra of $k_z^+ \tilde{E}_{zz}^+(\lambda_z^+, r^+)$, $k_z^+ \tilde{E}_{rr}^+(\lambda_z^+, r^+)$, and $k_z^+ \tilde{E}_{\theta\theta}^+(\lambda_z^+, r^+)$ of case A6, non-dimensionalized by u_τ^2 . (a) $k_z^+ \tilde{E}_{zz}^+$ on the convex side, (b) $k_z^+ \tilde{E}_{zz}^+$ on the concave side, (c) $k_z^+ \tilde{E}_{rr}^+$ on the convex side, (d) $k_z^+ \tilde{E}_{rr}^+$ on the concave side, (e) $k_z^+ \tilde{E}_{\theta\theta}^+$ on the convex side, and (f) $k_z^+ \tilde{E}_{\theta\theta}^+$ on the concave side. The value of u_τ equals to either $u_{\tau i}$ or $u_{\tau o}$, depending on the convex or the concave cylinder side in consideration. In each figure panel, the wavelength is given both as λ_z^+ (bottom) and as λ_z/δ (top). Similarly, the radial coordinate is given both as r^+ (left) and as $(R - r)/\delta$ or $(r - R)/\delta$ (right, for convex or concave side, respectively). The cross symbol '×' pinpoints the location of the mode. 41

2.15	Profiles of non-dimensionalized premultiplied 1D axial energy spectra $k_z^+ \tilde{E}_{zz}^+$ of the A- and D-series test cases at the cylindrical surface located at $r^+ = 15$ from the convex and concave walls. (a) convex side, and (b) concave side. Vertical dashed lines demarcate the axial computational sizes (i.e., L_z values) for cases A1-A6 and D.	45
2.16	Contours of premultiplied 1D axial energy spectra of $k_\theta^+ \tilde{E}_{zz}^+(\lambda_z^+, r^+)$, $k_\theta^+ \tilde{E}_{rr}^+(\lambda_z^+, r^+)$, and $k_\theta^+ \tilde{E}_{\theta\theta}^+(\lambda_z^+, r^+)$ of case B5, non-dimensionalized by u_τ^2 . (a) $k_\theta^+ \tilde{E}_{zz}^+$ on the convex side, (b) $k_\theta^+ \tilde{E}_{zz}^+$ on the concave side, (c) $k_\theta^+ \tilde{E}_{rr}^+$ on the convex side, (d) $k_\theta^+ \tilde{E}_{rr}^+$ on the concave side, (e) $k_\theta^+ \tilde{E}_{\theta\theta}^+$ on the convex side, and (f) $k_\theta^+ \tilde{E}_{\theta\theta}^+$ on the concave side. The value of u_τ equals to either $u_{\tau i}$ or $u_{\tau o}$, depending on the convex or the concave cylinder side in consideration. In each figure panel, the wavelength is given both as λ_θ^+ (bottom) and as λ_θ/δ (top). Similarly, the radial coordinate is given both as r^+ (left) and as $(R - r)/\delta$ or $(r - R)/\delta$ (right, for convex or concave side, respectively). The cross symbol ‘ \times ’ pinpoints the location of the mode.	48
2.17	Profiles of non-dimensionalized premultiplied 1D azimuthal energy spectra $k_\theta^+ \tilde{E}_{\theta\theta}^+$ of the B- and D-series test cases at the cylindrical surface located at $r^+ = 30$ from the convex and concave walls. (a) convex side, and (b) concave side. Vertical dashed lines demarcate the azimuthal computational sizes (i.e., L_θ values) for cases B1-B5 and D.	50
3.1	Computational domain and coordinates.	55
3.2	Profiles of 1D two-point correlation coefficients (R_{zz} and $R_{\theta\theta}$) for all test cases on the inner and outer cylinder sides. (a) The value of R_{zz} is calculated at $r^+ = 15$, where the Reynolds normal stress component $\langle u'_z u'_z \rangle$ peaks. (b) The value of $R_{\theta\theta}$ is calculated at $r^+ = 30$, where the Reynolds normal stress component $\langle u'_\theta u'_\theta \rangle$ peaks.	58

3.3	Contours of premultiplied 1D axial energy spectra of $k_z^+ \tilde{E}_{zz}^+(\lambda_z^+, r^+)$ and $k_\theta^+ \tilde{E}_{\theta\theta}^+(\lambda_z^+, r^+)$ of the case of $R_i/R_o = 0.1$. In the non-dimensionalization, the value of u_τ equals to either u_{τ_i} or u_{τ_o} , depending on the convex (inner) or the concave (outer) cylinder side in consideration. The cross symbol ‘×’ pinpoints the location of the mode. Three energy levels are distinguished, and the innermost, middle and outermost isopleths correspond to $0.875 \max(k_z^+ \tilde{E}_{ii}^+)$, $0.625 \max(k_z^+ \tilde{E}_{ii}^+)$ and $0.375 \max(k_z^+ \tilde{E}_{ii}^+)$, respectively. Besides these three isopleths which show three magnitude levels of the premultiplied spectrum relative to its peak value, the absolute magnitude of the non-dimensionalized premultiplied spectrum is also shown using a color legend.	61
3.4	Profiles of premultiplied 1D spectra of axial velocity fluctuations (u'_z) $k_z^+ \tilde{E}_{zz}^+(k_z, r)$ and azimuthal velocity fluctuations (u'_θ) $k_\theta^+ \tilde{E}_{\theta\theta}^+(k_\theta, r)$ for all test cases on the inner and outer cylinder sides. (a) The value of $k_z^+ \tilde{E}_{zz}^+(k_z, r)$ is calculated at $r^+ = 15$, where the Reynolds normal stress component $\langle u'_z u'_z \rangle$ peaks. (b) The value of $k_\theta^+ \tilde{E}_{\theta\theta}^+(k_\theta, r)$ is calculated at $r^+ = 30$, where the Reynolds normal stress component $\langle u'_\theta u'_\theta \rangle$ peaks.	63
3.5	Profiles of skin friction coefficient and boundary layer thickness of the inner and outer cylindrical walls in concentric annular pipe for all four test cases.	67
3.6	Values of constants κ and B of the logarithmic law of the wall associated with the mean axial flow in a concentric annular pipe for all cases.	67
3.7	Profile of the mean axial velocity $\langle u_z \rangle^+$. (a) in wall coordinate for case $R_i/R_o = 0.1$, and (b) in non-dimensionalized global coordinate $(r - R)/\delta$ for all test cases.	68
3.8	Profiles of Reynolds normal stresses at various radius ratios. Arrow points to the direction of an increasing radius ration R_i/R_o	70

3.9	Profiles of Reynolds shear stress $\langle u'_z u'_r \rangle^+$ at various radius ratios with respect to (a) wall-normal distance h/δ (measured from the inner wall, the Reynolds shear stress is non-dimensionalized by the average wall friction velocity u_τ), (b) wall coordinate (both the Reynolds shear stress and wall coordinate are non-dimensionalized based on the local wall friction velocity, i.e. $u_{\tau i}$ or $u_{\tau o}$ for the inner or outer cylinder side, respectively). Arrow points to the direction of an increasing radius ratio R_i/R_o	72
3.10	Profiles of the budget term of Reynolds shear stress $\langle u'_z u'_r \rangle$ of cases $R_i/R_o = 0.1$ and $R_i/R_o = 0.7$. All budget terms have been non-dimensionalized using local friction velocity ($u_{\tau i}$ or $u_{\tau o}$) and ν	74
3.11	Contours of $\overline{\omega'_z}^+$ superimposed with velocity vectors composed of $\overline{u'_\theta}$ and $\overline{u'_r}$, averaged in time and axial domain for cases $R_i/R_o = 0.1$ and 0.7 . For clarity, only one-quarter of the cross-section is shown.	76
3.12	Profiles of $\omega_{z,rms}^+$ for various radius ratios.	77
3.13	Profiles of the premultiplied 1D spectra of axial vorticity fluctuations $k_z^+ \tilde{\phi}_z^+(k_z, r)$ and $k_\theta^+ \tilde{\phi}_\theta^+(k_\theta, r)$ in the axial and azimuthal directions for the four test cases at surface located at wall-normal position $r^+ = 20$	79
3.14	Contours of swirling strength ($\lambda_{ci} = 1.25$) of cases $R_i/R_o = 0.1$ and 0.7 . The contours are colored with instantaneous axial vorticity ω'_z^+ . For clarity, only a portion of the computational domain is displayed with $L_z = 6\pi\delta$ and $L_\theta = \pi/2$ for all four panels.	81
3.15	Profiles of the premultiplied 1D spectra of axial velocity fluctuations $(u'_z) k_z^+ \tilde{E}_{zz}^+(k_z, r)$ and $k_\theta^+ \tilde{E}_{zz}^+(k_z, r)$ in the axial and azimuthal directions for the four cases at $\delta_{ti}/2$ and $\delta_{to}/2$ in core turbulence region relatively far above the inner and outer cylinder walls, respectively.	82

4.1	Computational domain and coordinate system. The flow is heated under a uniform wall heat flux condition ($\dot{q}_w = \dot{q}_{wi} = \dot{q}_{wo}$) through the inner and outer cylinder walls.	84
4.2	Profiles of the premultiplied 1D spectra of temperature fluctuations, (a) in the axial direction, and (b) azimuthal direction for the four cases at $r^+ = 15$, where the temperature variance peaks.	89
4.3	Effects of radius ratio on Nusselt number Nu and the skin friction coefficient C_f on the inner and outer cylinder sides.	91
4.4	Values of constants κ_Θ and B_Θ of the logarithmic law of the wall associated with the mean axial flow in a concentric annular pipe for all cases. Arrow points to the direction of an increasing value of the radius ratio R_i/R_o	93
4.5	Profile of the mean temperature $\langle \Theta \rangle^+$. (a) Displayed with respect to the wall coordinate for the case of $R_i/R_o = 0.1$, and (b) displayed with respect to the non-dimensionalized global coordinate $(r - R)/\delta$ for all test cases of $R_i/R_o = 0.1-0.7$. Arrow points to the direction of an increasing value of the radius ratio R_i/R_o . In panel (b), the thermal boundary layer thicknesses, δ_{ti}^* and δ_{to}^* are labeled for the case of $R_i/R_o = 0.1$	94
4.6	Profiles of RMS values of temperature fluctuation and axial turbulent heat flux at various radius ratios. Arrow points to the direction of an increasing value of the radius ratio R_i/R_o	96

4.7	Profiles of radial turbulent heat flux $-\langle\Theta'u'_r\rangle^+$ at various radius ratios with respect to (a) wall-normal distance h/δ (measured from the inner cylinder wall, the radial turbulent heat flux is non-dimensionalized by the average friction temperature $T_\tau u_\tau$), (b) wall coordinate (both the radial turbulent flux and wall coordinate are non-dimensionalized based on the local wall friction velocity and local friction temperature, i.e. $T_{\tau i} u_{\tau i}$ or $T_{\tau o} u_{\tau o}$ for the inner or outer cylinder side, respectively). Arrow points to the direction of an increasing radius ratio R_i/R_o	99
4.8	Profiles of the budget terms of temperature variance (k_Θ^+), axial turbulent heat flux ($\langle\Theta'u'_z\rangle^+$) and radial turbulent heat flux ($\langle\Theta'u'_r\rangle^+$) on the inner and outer cylinder sides of the case $R_i/R_o = 0.1$. The budget terms of the temperature variance is non-dimensionalized by $u_{\tau i}^2 T_{\tau i}^2/\nu$ or $u_{\tau o}^2 T_{\tau o}^2/\nu$, and those of the turbulent heat fluxes are non-dimensionalized by $u_{\tau i}^3 T_{\tau i}/\nu$ or $u_{\tau o}^3 T_{\tau o}/\nu$ on the inner or the outer cylinder side, respectively.	100
4.9	Contours of the instantaneous non-dimensionalized temperature fluctuations Θ'^+ , displayed over the cylindrical surface (or, z - θ plane) located at $r^+ = 15$ on the inner inside, and over the z - r and r - θ planes on the boundaries for cases of (a) $R_i/R_o = 0.1$ and (b) $R_i/R_o = 0.7$	103

4.10 Contours of 1D premultiplied spectra of temperature fluctuations ($k_z^+ \tilde{E}_{\Theta\Theta}^+$) and ($k_\theta^+ \tilde{E}_{\Theta\Theta}^+$) in the axial and azimuthal directions, respectively, for cases of $R_i/R_o = 0.1$ and $R_i/R_o = 0.7$. The cross symbol ‘×’ pinpoints the location of the mode. Three energy levels are distinguished, and the innermost, middle and outermost isopleths correspond to $0.875 \max(k_i^+ \tilde{E}_{\Theta\Theta}^+)$, $0.625 \max(k_i^+ \tilde{E}_{\Theta\Theta}^+)$ and $0.375 \max(k_i^+ \tilde{E}_{\Theta\Theta}^+)$, respectively. Besides these three isopleths which show three magnitude levels of the premultiplied spectrum relative to its peak value, the absolute magnitude of the non-dimensionalized premultiplied spectrum is also shown using a color legend. In the non-dimensionalization, the value of the wall friction velocity and temperature equal to either $u_{\tau i}$ and $T_{\tau i}$, or $u_{\tau o}$ and $T_{\tau o}$ depending on the convex (inner) or the concave (outer) cylinder side in consideration. The horizontal black dashed line demarcates the border that separates premultiplied spectrum on the inner and outer cylinder sides. 105

4.11 Premultiplied 2D spectra $k_z^+ k_\theta^+ \check{E}_{\Theta\Theta}^+$ on the inner and outer cylinder sides of the concentric annular pipe for the case of $R_i/R_o = 0.1$ at one-half the thermal boundary layer from the inner or outer cylinder wall (i.e., at $\delta_{ii}^*/\delta = 0.5$ or $\delta_{to}^*/\delta = 0.5$). The cross symbol ‘×’ pinpoints the location of the mode. Three energy levels are distinguished, and the innermost, middle and outermost isopleths correspond to $0.875 \max(k_z^+ k_\theta^+ \check{E}_{\Theta\Theta}^+)$, $0.625 \max(k_z^+ k_\theta^+ \check{E}_{\Theta\Theta}^+)$ and $0.375 \max(k_z^+ k_\theta^+ \check{E}_{\Theta\Theta}^+)$, respectively. In the non-dimensionalization, the value of the wall friction velocity and temperature equal to either $u_{\tau i}$ and $T_{\tau i}$, or $u_{\tau o}$ and $T_{\tau o}$ depending on the convex (inner) or the concave (outer) cylinder side in consideration. 108

A.1	Comparison of wall-normal profile of mean velocity and Reynolds normal stress against the DNS results by Chung et al. (2002), labeled as the case of Ca.	134
A.2	Comparison of wall-normal profile of mean velocity and Reynolds normal stress against the DNS results by Chung et al. (2002)	135
A.3	The pencil decomposition of data.	138
A.4	Scalability of the parallel code obtained on the WestGrid (Orcinus) server.	140

Nomenclature

English Symbols:

B	additive constant of the logarithmic law of the wall
B_{Θ}	additive constant of the logarithmic law of the wall
C_f	skin friction coefficient: $\tau_w/(\rho U_b^2/2)$
D_h	hydraulic diameter: 4δ
D_i	viscous diffusion term for turbulent heat flux $\langle \Theta' u_i' \rangle$
D_{Θ}	viscous diffusion term for temperature variance k_{Θ}
D_{zr}	viscous dissipation term for the budget balance of Reynolds-shear stress
\check{E}_{ij}	two-dimensional velocity spectrum
\tilde{E}_{ij}	one-dimensional velocity spectrum
$\check{E}_{\Theta\Theta}$	two-dimensional temperature spectrum
$\tilde{E}_{\Theta\Theta}$	one-dimensional temperature spectrum
\hat{e}_z	base unit vector of the z -direction
k_z, k_{θ}	wavenumbers in the axial and azimuthal directions
$k_{z0}, k_{\theta0}$	free-space wavenumbers in the axial and azimuthal directions
k_{Θ}	temperature variance: $\langle \Theta' \Theta' \rangle / 2$
L_z	computational domain length in the z direction
L_{θ}	computational domain length in the θ direction
N_z, N_{θ}, N_r	grid points in z, θ, r directions, respectively

n_z, n_θ	integer indices for the axial and azimuthal wavenumbers
Nu	Nusselt number
p	pressure
P_Θ	production term for temperature variance k_Θ
P_i	production term for turbulent heat flux $\langle \Theta' u_i' \rangle$
$Pe_{\tau i}$	Péclet number: $u_\tau \delta_{ti}^* / \alpha$
$Pe_{\tau o}$	Péclet number: $u_\tau \delta_{to}^* / \alpha$
Pr	Prandtl number: ν / α
R	midsection radius of annular pipe
P_{zr}	production term for the budget balance of Reynolds shear stress
R_i, R_o	radii of the inner and outer pipes, respectively
$Re_{\tau i}$	Reynolds number: $u_\tau \delta_{ti} / \nu$
$Re_{\tau o}$	Reynolds number: $u_\tau \delta_{to} / \nu$
Re_{D_h}	Reynolds number: $U_b D_h / \nu$
Re_δ	Reynolds number: $U_b \delta / \nu$
$R_{zz}(\Delta z)$	two-point correlation of streamwise velocity fluctuations in the z direction
$R_{\theta\theta}(r\Delta\theta)$	two-point correlation of azimuthal velocity fluctuations in the θ direction
t	time
T_{zr}	turbulent diffusion term for the budget balance of Reynolds-shear stress
T	temperature
T_w	the local mean wall temperature of the inner and outer side
T_{wi}	the local mean wall temperature of the inner side
T_{wo}	the local mean wall temperature of the outer side
T_Θ	turbulent diffusion term for temperature variance k_Θ
T_i	turbulent diffusion term for turbulent heat flux $\langle \Theta' u_i' \rangle$

T_τ	wall friction temperature: $(\dot{q}_{wi}R_i + \dot{q}_{wo}R_o)/(\rho C_p u_\tau (R_i + R_o))$
$T_{\tau i}$	wall friction temperature of the inner wall: $\dot{q}_{wi}/\rho C_p u_{\tau i}$
$T_{\tau o}$	wall friction temperature of the outer wall: $\dot{q}_{wo}/\rho C_p u_{\tau o}$
u_τ	mean friction velocity: $\sqrt{\tau_w/\rho}$
$u_{\tau i}$	inner wall friction velocity: $\sqrt{\tau_{wi}/\rho}$
$u_{\tau o}$	outer wall friction velocity: $\sqrt{\tau_{wo}/\rho}$
U_b	bulk mean velocity
u_z, u_θ, u_r	velocity components in the z, θ, r directions, respectively
z, θ, r	coordinates of the z, θ, r directions, respectively

Greek Symbols:

α	thermal diffusion coefficient
δ	half width between inner and outer cylinder walls: $(R_o - R_i)/2$
δ_{ti}	boundary layer thickness on the inner cylinder side
δ_{to}	boundary layer thickness on the outer cylinder side
δ_{ti}^*	thermal boundary layer thickness on the inner cylinder side
δ_{to}^*	thermal boundary layer thickness on the outer cylinder side
Δr_{min}	minimum grid spacing in the radial direction
Δr_{max}	maximum grid spacing in the radial direction
$\Delta z, \Delta \theta$	grid spacing in axial and azimuthal directions, respectively
ν	kinematic viscosity
Π	constant mean axial pressure gradient
Π_{zr}	velocity-pressure-gradient term for the budget balance of Reynolds shear stress
Π_Θ	velocity-pressure-gradient term for temperature variance k_Θ
Π_i	velocity-pressure-gradient term for turbulent heat flux $\langle \Theta' u_i' \rangle$
ρ	density of fluid

τ_{tot}	total shear stress
τ_{wi}	mean wall shear stress on the inner wall
τ_{wo}	mean wall shear stress on the outer wall
λ_{ci}	swirling strength
λ_z	wavelength in the axial direction
λ_θ	wavelength in the azimuthal direction
κ	von Kármán constant
κ_Θ	thermal von Kármán constant
$\check{\phi}$	two-dimensional vorticity spectrum
$\tilde{\phi}$	one-dimensional vorticity spectrum
$\omega_z, \omega_\theta, \omega_r$	vorticity fluctuations in the z, θ, r directions, receptively
ε_{zr}	dissipation term for the budget balance of Reynolds shear stress
ε_Θ	dissipation term for temperature variance k_Θ
ε_i	dissipation term for turbulent heat flux $\langle \Theta' u_i' \rangle$
Θ	temperature deviation from the local wall temperature : $\Theta = T_w - T$
Θ_m	mixed mean temperature

Subscripts and Superscripts:

$(\cdot)'$	fluctuating component
$(\cdot)^+$	wall coordinate
$\overline{(\cdot)}$	time averaging
$\tilde{(\cdot)}$	one-dimensional spectrum
$\check{(\cdot)}$	two-dimensional spectrum
$(\cdot)_i, (\cdot)_o$	values at the inner and outer walls, respectively
$(\cdot)_{max}, (\cdot)_{min}$	maximum and minimum values, respectively

- $(\cdot)_{rms}$ root-mean-square value
 $(\cdot)_w$ value at the wall
 $\langle \cdot \rangle$ averaging over time and the homogeneous z - θ directions

Abbreviations:

- 1D one-dimensional
2D two-dimensional
CFL Courant-Friedrichs-Lewy
DNS direct numerical simulation
LDV laser Doppler velocimetry
RMS root mean square
RANS Reynolds-averaged Navier–Stokes
TSE turbulent scalar energy
TKE turbulence kinematics energy
ZPG zero-pressure gradient

Chapter 1

Introduction

1.1 Background and motivation

Turbulent flow and heat transfer in a concentric annular pipe flow has many engineering applications, such as heat exchangers, jet engine diffusers and oil drilling processes (Nouri et al., 1993). The transports of momentum and thermal energy in a concentric annular pipe are affected by the transverse curvatures of the inner (convex) and outer (concave) walls. In response to the difference in transverse curvature of the inner and outer walls, the spatial and temporal scales of turbulence are different near these two curved walls of a concentric pipe. This further results in an asymmetry in the radial profiles of the statistical moments of the velocity and temperature fields, making the physics of turbulent flow and heat transfer more complex than that of in a circular pipe flow or plane-channel flow. Furthermore, the case of concentric annular pipe flow is general because both plane-channel and round pipe flows are special cases of concentric annular pipe flows under the condition of $R_i/R_o \rightarrow 1$ and $R_i/R_o \rightarrow 0$, respectively. Here, R_i and R_o (with $0 \leq R_i \leq R_o$) are the radii of the inner or outer pipes, respectively. The current research focuses on Poiseuille-type turbulent concentric annular pipe flow driven by a constant axial pressure gradient, which is different from the classical Taylor-Couette flow driven by wall shear due to relative

rotation of the inner and outer cylinder surfaces (Taylor, 1923, 1936; Grossmann et al., 2016).

1.2 Literature review

Thus far, previous experimental and numerical studies of Poiseuille-type concentric annular pipe flow have primarily focused on the characteristics of the first- and second-order flow statistics (such as the locations corresponding to the maximum mean velocity and the zero mean Reynolds shear stress studied by Knudsen and Katz (1950), Brighton and Jones (1964), Rehme (1974), Nouri et al. (1993), and Chung et al. (2002)). In the current literature, there has been a disagreement on whether the radial position corresponding to the maximum velocity collocates with that of the zero mean shear stress. The experiments of Knudsen and Katz (1950) and Brighton and Jones (1964) on concentric annular pipe water flows indicated that the maximum velocity and the zero mean shear stress coincide. However, Rehme (1974) reported that the radial position of the zero mean shear stress is closer to the inner wall than that of the maximum velocity based on their measurements of annular concentric pipe airflows using a double Pitot tube and hot-wire anemometry. Nouri et al. (1993) conducted comprehensive laser-Doppler velocimetry (LDV) measurements of the flow fields in both concentric and eccentric annuli for both Newtonian and Non-Newtonian fluids. They showed that the radial positions of the maximum velocity and zero shear stress are not collocated. This contradiction is also seen among numerical simulations. Chung et al. (2002) performed DNS of a concentric annular pipe flow at Reynolds number $Re_{D_h} = U_b D_h / \nu = 8900$ similar to the experimental conditions of Nouri et al. (1993), using a second-order finite difference method. Later Chung and Sung (2003) extended their DNS study to also include turbulent heat transfer under a constant wall heat flux ratio. Here, U_b represents the bulk mean velocity, D_h is the hydraulic diameter, and ν is the kinematic viscosity of the fluid. The DNS result of Chung

et al. (2002) indicated that the deviation in the radial positions of the maximum mean axial velocity and zero shear stress is less than 1%. However, a more recent DNS study of Boersma and Breugem (2011) based on a second-order finite volume method code (conducted under conditions of $R_i/R_o = 0.1$ and $Re_{D_i} = 8900\text{--}13940$) further showed the collocation of these two positions.

1.2.1 Influence of domain size on direct numerical simulation of turbulent flow in a moderately-curved concentric annular pipe

Over the past three decades, various DNS studies were performed to understand circular pipe flows and structures, which feature two-dimensional (2D) statistical homogeneity over an axial-azimuthal cylindrical surface. In the homogeneous directions, typically, periodical boundary conditions are implemented. The minimum computational domain size over which a periodic boundary condition can be used for conducting DNS with sufficient predictive accuracy is a critical issue. In their pioneering DNS study of the minimum computational domain for near-wall turbulence, Jiménez and Moin (1991) revealed that the prediction of turbulence statistics would not be accurate if the size of the computational domain is smaller than that of the so-called “minimal channel”. Chin et al. (2010) performed DNS to investigate the influence of computational domain size on the first- and second-order turbulence statistics and axial velocity spectrum of turbulent circular pipe flows. They applied periodic boundary conditions to the axial and azimuthal directions for a wide range of pipe lengths for $L_z = \pi R\text{--}20\pi R$, where R is the radius of the circular pipe. In their DNS study of a turbulent plane Couette flow, Avsarkison et al. (2014) kept a computational domain length at $L_z = 20\pi\delta$ to ensure capture of streamwise-elongated flow structures. Here, δ is one-half the plane channel height. Very recently, Yang and Wang (2018) conducted a DNS study of streamwise rotating turbulent channel

flow at a low Reynolds number of $Re_\tau = u_\tau \delta / \nu = 180$ in conjunction with a wide range of rotation numbers. They discovered that the wavelength of the streamwise elongated Taylor-Görtler-like (TG-like) structures increases significantly with the rotation number. At their highest rotation number tested, an extremely long domain of $L_z = 512\pi\delta$ was used in order to correctly capture TG-like vortices.

Although there are many DNS investigations into the effects of computational domain size on the predictive accuracy of channel and pipe flows (see, for example, Jiménez and Moin (1991) and Chin et al. (2010)), the number of systematic studies on the proper computational domain size for transient simulation of turbulent concentric annular pipe flow is still very limited in the current literature. In the DNS studies of Chung et al. (2002) and Boersma and Breugem (2011), the concentric pipe length was set to $L_z = 6\pi\delta$ and $10R_o$, respectively, based on an analysis of the two-point correlation coefficient of axial velocity fluctuations. Here, δ is one-half the cylinder gap, i.e. $\delta = (R_o - R_i)/2$, defined in analogy to the usual convention for a plane-channel flow (in which one-half the channel height between two planes is often used as a basic measurement length scale). Quadrio and Luchini (2002) performed DNS study of turbulent concentric annular pipe flow, with the radius ratio kept at $R_i/R_o = 0.33$ and 0.5 , and the axial pipe length set to $L_z = 4\pi\delta$. They examined the first- and second-order flow statistics and studied the effect of transverse curvature on the peak value of Reynolds shear stresses. In this chapter, the goal is to conduct a systematic study of the minimum computational domain for DNS of concentric pipe flow in both physical and spectral spaces. The evidence is shown to confirm a much longer concentric pipe is needed in order to obtain accurate DNS results of flow statistics. To this purpose, a comparative study based on different domain sizes in the axial and azimuthal directions is conducted. The largest computational domain size ($L_z = 30\pi\delta$ and $L_\theta = 2\pi$) tested here far exceeds those reported in the literature. Furthermore, based on the aforementioned investigation of the minimum computational domain size, highly accurate DNS datasets are compiled and used for studying turbulence

statistical moments and coherent structures of the concentric annular pipe flow, which is an other objective of this research.

1.2.2 The effects of radius ratio on turbulent concentric annular pipe flow and structures

In a concentric annular pipe flow, the radius ratio not only alters the transverse curvature of the inner and outer cylinder walls, but also drastically affects the characteristics of turbulent boundary layers developed over the inner and outer cylinder walls. Closely related to this subject, in the current literature, there are studies of flows over a single concave or convex curved surface. For instance, So and Mellor (1973) conducted an experiment in a wind tunnel of curved surfaces to study curvature effects on turbulent flow field. They reported that turbulence intensities are higher on the concave wall than on the convex wall. Neves et al. (1994) conducted DNS to study the effects of transverse curvature on the turbulent boundary layer developed over a convex surface. They showed that as the transverse curvature increases, the slope of the mean axial velocity in the logarithmic region and the turbulent intensities reduce. They also showed that turbulence structures remain unaffected unless the ratio of boundary layer thickness to the radius of transverse curvature is large.

As reviewed above, although there are a couple of experimental and numerical studies of the concentric annular pipe flow of different radius ratios (Nouri et al., 1993; Chung et al., 2002), the number of detailed DNS studies of the effects of radius ratio on the turbulent flow in a concentric annular pipe is still rather limited in the current literature.

In view of this, the goal is to conduct a systematic DNS study of turbulent concentric annular pipe flow based on various radius ratios ($R_i/R_o = 0.1-0.7$). Specifically, the effects of radius ratio are examined on the first- and second-order statistical moments of the velocity field, the interaction of the boundary layers developed over the

inner and outer cylinder walls, spectra of the velocity and vorticity fields, the budget balance of Reynolds shear stress, and the length scales of the streamwise vortical structures near the inner and outer cylinder walls.

1.2.3 The effects of radius ratio on turbulent heat transfer in concentric annular pipe flows

In the literature, extensive experimental and theoretical studies have been reported to understand the characteristics of turbulent heat transfer in a Taylor-Poiseuille flow. However, most of these studies were concentrated on experimental measurements, developments of semi-empirical correlations, and Reynolds-averaged Navier-Stokes (RANS) simulations. Kays and Leung (1963) conducted an experiment to study turbulent flow and heat transfer in a concentric annular pipe under the conditions of a fully-developed velocity profile and constant surface heat flux. They reported first- and second-order statistics of temperature field for a wide range of radius ratios, Reynolds numbers and Prandtl numbers. Wilson and Medwell (1968) used the van Driest model in their numerical simulation of the temperature field in a turbulent concentric annular pipe with a heated inner wall. Heikal et al. (1977) conducted hot-wire measurements of turbulent heat transfer in a concentric annular pipe flow. They studied the mean characteristic of temperature field and rate of heat transfer. Mujeeb and Richard (1981) conducted RANS simulations based on three different turbulence models to study the temperature field in a concentric annular pipe flow. They improved the performance of their RANS simulations by using the transport equation of turbulence kinetic energy and characteristic mixing length scale in turbulence modeling. Later, Kaneda et al. (2003) derived a numerical predictive method by using a semi-empirical model for the radial heat flux. They evaluated the value of Nusselt number as the Prandtl number varies. Yu et al. (2005) proposed a new modeling equations for computing the values of Nusselt number for fully-developed

turbulent convection in a concentric annular pipe, under the condition that the inner cylinder wall is uniformly heated. They studied the Nusselt number for a wide range of radius ratios and Reynolds numbers. Although RANS studies have provided important insights into the first- and second-order statistical moments of the flow, they have many limitations. For instance, high-order statistical moments (such as skewness and flatness factors) and detailed transport processes of the Reynolds stress tensor and heat flux vector cannot be well studied using a RANS approach.

In comparison with the RANS studies briefly reviewed above, so far, there have been only a few DNS studies devoted to investigating turbulent heat transfer in concentric annular pipe flows. Chung and Sung (2003) performed DNS to study the transverse curvature effects on the turbulent heat transfer in a concentric annular pipe flow at a Reynolds number of $Re_{D_h} = 8900$. To this purpose, they compared the turbulence statistics of the velocity and temperature fields on the inner and outer cylinder sides. Ould-Rouiss et al. (2009) performed a DNS study of a heated concentric annular pipe flow at $Re_\delta = 3500$ and $Pr = 0.71$. Here, the Reynolds number is defined based on the half-width between the inner and outer walls, $\delta = (R_o - R_i)/2$. They studied the effect of heat flux ratio with boundary conditions identical to those used by Chung and Sung (2003). Later, Ould-Rouiss et al. (2010) investigated the effects of Prandtl number on turbulent heat transfer in a concentric annular pipe using DNS. They observed that the turbulent heat transfer rate reduces near both walls as the Prandtl number decreases from 1 to 0.026. Fukuda and Tsukahara (2020) conducted a DNS study of passive heat transfer in Taylor-Poiseuille flow at two radius ratios of $R_i/R_o = 0.5$ and 0.8 for $Re_\tau = 150$ and $Pr = 0.71$. They investigated the dependence of heat transfer on the radius ratio and the thermal boundary condition.

As reviewed above, although there are has been multiple experimental and RANS studies of turbulent heat transfer in concentric annular pipe flow for different radius ratios, the number of detailed DNS studies is still rather limited. In view of this, I aim at conducting a systematic comparative DNS study of the turbulent heat transfer

in concentric annular pipe flow based on four radius ratios (for $R_i/R_o = 0.1, 0.3, 0.5$ and 0.7) at a nominal Reynolds number of $Re_{D_h} = 17700$. Specifically, I will examine the effects of radius ratio on the first- and second-order statistical moments of the temperature field, interaction of the thermal boundary layers developed over the inner and outer cylinder walls, spectra of the temperature fields, budget balance of temperature variance and turbulent heat fluxes, and the length scales of the thermal structures near the inner and outer cylinder walls.

1.3 Objectives

The major objectives of this research are given presented as follows:

1. Develop, optimize and validate a new pseudo-spectral code using FORTRAN 90/95 programming language and message passing interface (MPI) libraries to perform DNS study of turbulent flow and heat transfer in a concentric annular pipe. This objective is to provide an innovative tool to numerically study the complex flow physics and the effects of surface curvature on turbulent heat and fluid flows.
2. Systematically investigate the effects of the computational domain size on the predictive accuracy of turbulence statistics and flow structures.
3. Systematically investigate the effects of the radius ratio on turbulence statistics and flow structures.
4. Systematically investigate the effects of the radius ratio on turbulent heat transfer and turbulence structures associated with temperature field.

1.4 Outlines of the proposed thesis

The remainder of this thesis is organized as follows:

- In Chapter 2, DNS study on effect of computational domain size in a moderately-curved turbulent concentric annular pipe flow for a wide range of computational domain sizes is presented.
- In Chapter 3, DNS study of radius ratio effects on turbulence statistics and structures in concentric annular pipe flow for a wide range of radius ratios at is presented.
- In Chapter 4, the DNS study of radius ratio effects on turbulent heat transfer and turbulence structures associated with temperature field in concentric annular pipe flow for a wide range of radius ratios at is presented.
- In Chapter 5, major conclusions of this thesis and the recommended future works are presented.
- In Appendix A, detailed numerical algorithms of the pseudo-spectra code are presented. For the testing run, a DNS of turbulent concentric annular flow at $Re_{D_h} = 8900$ was conducted using the pseudo-spectra code, and the results are validated against Chung and Sung (2003).
- In Appendix B, Implementation of Pseudo-spectral code in FORTRAN 90/95 programming language is presented.

Chapter 2

Influence of Domain Size on Direct Numerical Simulation of Turbulent Flow in a Moderately-Curved Concentric Annular Pipe

In this chapter, we aim at conducting a systematic study of the minimum computational domain for DNS of concentric pipe flow in both physical and spectral spaces. New evidence will be shown to prove that a much longer concentric pipe than those reported in the literature is needed in order to obtain accurate DNS results of flow statistics. To this purpose, a comparative study based on different domain sizes in the axial and azimuthal directions is conducted. Furthermore, based on the aforementioned investigation of the minimum computational domain size, highly accurate DNS datasets are compiled and used for studying turbulence statistical moments and coherent structures of the concentric annular pipe flow, which is the third objective of this research. A new highly-accurate pseudo-spectral method computer code is used for performing DNS, which was developed using the FORTRAN 90/95 programming

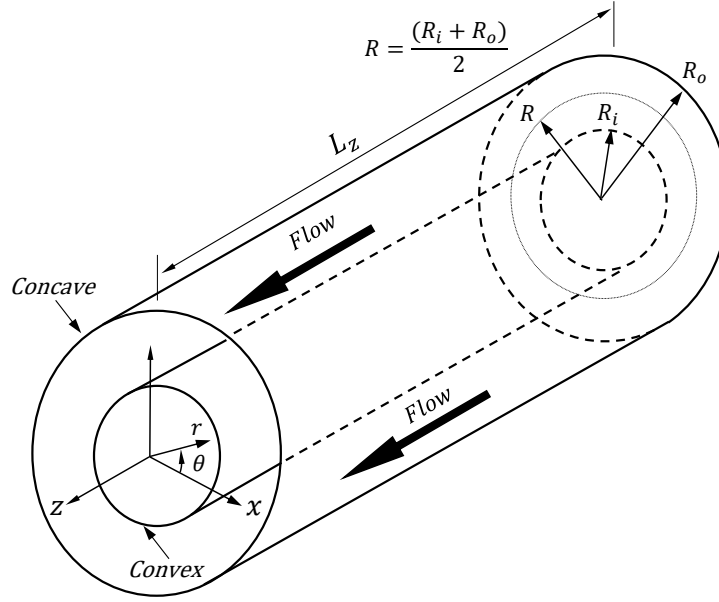


Figure 2.1: Computational domain and coordinate system.

languages and the message passing interface (MPI) libraries. The algorithms of this computer code are given in Appendices A and B. The content and results of following chapter is published in Bagheri et al. (2020).

The remainder of this chapter is organized as follows: in section 2.1, the test cases and the numerical algorithm for solving the governing equations are described. In section 2.2, the DNS results in the physical space are analyzed, including the first-, second-, third- and fourth-order statistical moments of the velocity field, and the two-point correlation functions of velocity fluctuations. In section 2.3, turbulent coherent structures are investigated and their scales are studied based on calculation of both two-dimensional (2D) and one-dimensional (1D) energy spectra. The scales of energetic eddies and the corresponding domain size for capturing them are examined through analyses conducted in both physical and spectral spaces.

Table 2.1: Summary of test cases and grid resolutions. The nominal Reynolds number is $Re_{D_h} = 8900$ for the A-, B- and C-series test cases, and is $Re_{D_h} = 17700$ for case D.

Cases	$L_z \times L_\theta \times L_r$	$N_z \times N_\theta \times N_r$	Δz^+	$(R_o \Delta \theta)^+$	Δr_{\min}^+	Δr_{\max}^+
A1	$\pi\delta \times 2\pi \times 2\delta$	$36 \times 512 \times 64$	12.819	7.214	0.180	7.376
A2	$2\pi\delta \times 2\pi \times 2\delta$	$64 \times 512 \times 64$	14.528	7.267	0.182	7.431
A3	$6\pi\delta \times 2\pi \times 2\delta$	$192 \times 512 \times 64$	14.422	7.215	0.180	7.377
A4 (B5)	$12\pi\delta \times 2\pi \times 2\delta$	$384 \times 512 \times 64$	14.390	7.198	0.180	7.360
A5	$18\pi\delta \times 2\pi \times 2\delta$	$580 \times 512 \times 64$	14.361	7.234	0.181	7.396
A6	$30\pi\delta \times 2\pi \times 2\delta$	$960 \times 512 \times 64$	14.461	7.234	0.181	7.396
B1	$12\pi\delta \times \pi/6 \times 2\delta$	$384 \times 42 \times 64$	14.679	7.459	0.184	7.508
B2	$12\pi\delta \times \pi/4 \times 2\delta$	$384 \times 64 \times 64$	14.489	7.248	0.181	7.411
B3	$12\pi\delta \times \pi/2 \times 2\delta$	$384 \times 128 \times 64$	14.475	7.241	0.181	7.404
B4	$12\pi\delta \times 3\pi/4 \times 2\delta$	$384 \times 192 \times 64$	14.431	7.219	0.181	7.381
C	$6\pi\delta \times \pi/2 \times 2\delta$	$192 \times 128 \times 64$	14.422	7.215	0.180	7.377
Ca	$6\pi\delta \times \pi/2 \times 2\delta$	$192 \times 128 \times 65$	14.30	7.11	0.12	12.96
D	$8\pi\delta \times \pi/2 \times 2\delta$	$500 \times 280 \times 144$	13.878	6.199	0.069	6.100

2.1 Test case and numerical algorithm

Figure 2.1 shows the schematic diagram of concentric annular pipe flow with respect to the cylindrical coordinate system. In this figure, z , θ , and r , denote the axial (streamwise), azimuthal and radial coordinates, respectively, and u_z , u_θ and u_r represent velocity components in the corresponding directions. The radius of the cylindrical channel center is $R = (R_i + R_o)/2$. The equations that govern an incompressible flow with respect to a cylindrical coordinate system read

$$\nabla \cdot \vec{u} = 0 \quad , \quad (2.1)$$

$$\frac{\partial \vec{u}}{\partial t} + \vec{u} \cdot \nabla \vec{u} = -\frac{1}{\rho} \nabla p + \nu \nabla^2 \vec{u} - \frac{\Pi}{\rho} \hat{\mathbf{e}}_z \quad , \quad (2.2)$$

where p , ρ and ν denote the pressure, density and kinematic viscosity, respectively. Π is the constant mean axial pressure gradient that drives the flow, and $\hat{\mathbf{e}}_z$ is the base unit vector of the z -direction, with $|\hat{\mathbf{e}}_z| \equiv 1$. The details of numerical algorithm to solve the governing equations of the problem are presented in appendix A.

Table 2.1 summarizes the computational domain sizes and grid resolutions for the 14 test cases of two nominal Reynolds numbers of $Re_{D_h} = 8900$ and 17700. In order to facilitate our comparative study of the domain size effect on the predictive accuracy of flow statistics and coherent structures, the radius ratio is kept at $R_i/R_o = 0.5$ for all 14 test cases. This radius ratio and lower nominal Reynolds number ($Re_{D_h} = 8900$) considered here are identical to those used in Chung et al. (2002) and Nouri et al. (1993). The test cases are categorized and labeled using four initial letters: A, B, C and D. Six different axial domain sizes with a full cross-sectional domain (referred to as the A-series test cases) are compared to examine the influence of axial computational domain size on the predictive accuracy of turbulent statistics in both physical and spectral spaces. In these six test cases, the axial domain size varies from $L_z = \pi\delta$ to $30\pi\delta$, while the azimuthal domain size is fixed to $L_\theta = 2\pi$. The reason that a full azimuthal domain size is used in the A-series test cases is that this can completely shield off the effect of the azimuthal domain size on the flow statistics. The next group is the five B-series test cases, which examine the influence of azimuthal domain size L_θ on turbulent statistics. Five different azimuthal domain sizes ranging from $L_\theta = \pi/6$ to 2π are compared. For the five B-series test cases, the axial domain size is fixed at $L_z = 12\pi\delta$ based on the conclusion obtained from the above comparative study of the A-series test cases. Case A4 (of A-series) is also case B5 (of B-series). For the purpose of comparison and code validation, the computational domain size of Chung et al. (2002) is also considered, which leads to the C-series test cases. In Table 2.1, our DNS run with a finer radial grid resolution is labeled as case C, and that of Chung et al. (2002) is referred to as case Ca. In order to study the Reynolds number effect on the statistical moments of the velocity field, a higher nominal Reynolds number of $Re_{D_h} = 17700$ is also considered, which is referred to as case D.

As shown in Table 2.1, in all our 12 test cases of A, B and C series, the axial grid resolution ranges from $\Delta z^+ = 12.819$ for case A1 to 14.679 for case B1, and the azimuthal grid resolutions range from $(R_i\Delta\theta)^+ = 3.599$ for case A4 (or B5) to

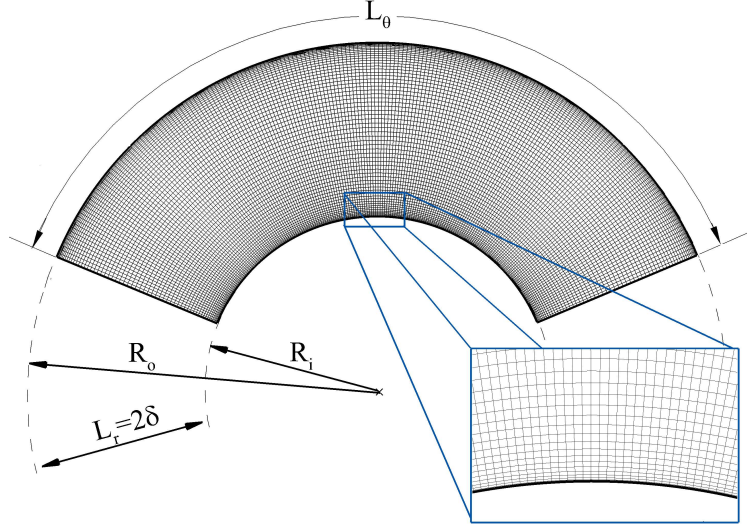


Figure 2.2: Cross-sectional view of the mesh for case B4.

$(R_o\Delta\theta)^+ = 7.459$ for case B1. From Table 2.1, it is clear that the axial and azimuthal grid resolutions are close to those used in Chung et al. (2002). The grid resolution of case D is slightly finer than those of the other test cases in general. As an example for showing the grid system, Fig. 2.2 provides a cross-sectional view of the mesh used for performing DNS of case B4. The finest radial grid resolution for the first node off the wall ranges from $\Delta r_{\min}^+ = 0.180$ to 0.184 , which is slightly larger than that used in Chung et al. (2002) but satisfies the need for performing rigorous DNS of wall-bounded turbulence. More importantly, the maximum radial grid resolution in our DNS is restricted to $\Delta r_{\max}^+ = 7.376$ – 7.508 , which is much finer than that ($\Delta r_{\max}^+ = 12.96$) used in Chung et al. (2002). In Table 2.1, the wall unit is defined based on the kinematic viscosity ν of the fluid, and averaged wall friction velocity $u_\tau = \sqrt{\tau_w/\rho}$, where τ_w is the mean wall shear stress based on weighted averaging over the concave and convex walls, i.e.

$$\tau_w = \frac{R_i\tau_{wi} + R_o\tau_{wo}}{R_i + R_o} . \quad (2.3)$$

The grid resolutions listed in Table 2.1 are calculated based on the averaged

wall friction velocity u_τ . The wall frictional velocity can also be defined locally as $u_{\tau_i} = \sqrt{\tau_{wi}/\rho}$ and $u_{\tau_o} = \sqrt{\tau_{wo}/\rho}$, with $\tau_{wi} = \rho\nu(d\langle u_z \rangle/dr)_{r=R_i}$ and $\tau_{wo} = -\rho\nu(d\langle u_z \rangle/dr)_{r=R_o}$ at the inner and outer cylinder walls, respectively. The values of u_{τ_i} and u_{τ_o} are different due to the surface curvature of the inner and outer cylinders. The ratio between these two wall friction velocities is $u_{\tau_i}/u_{\tau_o} = 1.0596$ under the test conditions. In this chapter, unless otherwise noted, we use the local wall friction velocities u_{τ_i} and u_{τ_o} in the non-dimensionalization of various quantities.

In our analysis, an instantaneous flow variable (for example, u_z) is decomposed into an averaged and a fluctuating component, i.e. $u_z = \langle u_z \rangle + u'_z$, where a pair of angular brackets $\langle \cdot \rangle$ represent temporal and spatial averaging over the homogeneous directions. Specifically, the spatial averaging is performed over a z - θ cylindrical surface at an arbitrary radial position r , and temporal averaging was performed over 35 large-eddy turnover times (LETOTs). Here, one LETOT is defined as δ/u_τ , which is a measure of the required time for large-scale structures with scale of δ to be uncorrelated. According to Adrian (2007), the length scale of large-scale motions (or “turbulent bulges”) is approximately $2\text{--}3\delta$ in a wall-bounded flow. Thus, an extended duration of 35 LETOTs facilitates the evolution of large-scale structures and achieving good convergence in the calculation of the statistics of the velocity field. The computational time step was kept at $0.001\delta/U_b$ to keep the Courant-Friedrichs-Lewy (CFL) number less than 0.8. All computations were performed on the WestGrid (Western Canada Research Grid) supercomputers. Furthermore, spectral accuracy was also ensured during the computation of flow statistics. Required CPU hours to conduct a DNS varies depending on the number of grid points. Test cases A1 and A6 using 384 and 14,400 CPU hours are the least and the most expensive among all the test cases, which were performed using 384 and 14,400 CPU hours, respectively.

Table 2.2 lists the mean flow parameters calculated from DNS for different test cases. In the table, Reynolds numbers $Re_{\tau_i} = u_{\tau_i}\delta_{ti}/\nu$ and $Re_{\tau_o} = u_{\tau_o}\delta_{to}/\nu$ are defined based on the wall friction velocities (u_{τ_i} and u_{τ_o}) and boundary layer thicknesses (δ_{ti}

Table 2.2: Mean flow parameters calculated from DNS.

Cases	δ_{ti}/δ	δ_{to}/δ	Re_{τ_i}	Re_{τ_o}	Re_{D_h}
A1	0.867	1.133	130.91	164.24	8944
A2	0.887	1.113	136.86	161.29	8953
A3	0.880	1.120	134.14	161.55	8926
A4 (B5)	0.877	1.123	133.12	161.79	8935
A5	0.880	1.120	134.30	162.15	8926
A6	0.881	1.119	134.69	161.82	8917
B1	0.893	1.107	139.77	161.75	9042
B2	0.878	1.122	134.25	162.71	8962
B3	0.877	1.123	133.89	162.75	8944
B4	0.879	1.121	133.82	161.98	8944
C	0.880	1.120	134.14	161.55	8935
D	0.882	1.118	253.02	302.87	17770

and δ_{to}) over the inner and outer cylinder walls, respectively. The boundary layer thickness, δ_t , is the wall-normal distance across a boundary layer from either the inner or the outer wall to the point where the mean axial velocity reaches its maximum (correspondingly, the Reynolds shear stress is zero). The exact wall-normal position of this point will be investigated separately in section 2.2.2. The numerical simulations were set up under the condition of a constant mean streamwise pressure gradient (Π), which can be determined as

$$\Pi = -\frac{2(\tau_{wi}R_i + \tau_{wo}R_o)}{(R_o^2 - R_i^2)} . \quad (2.4)$$

In the above equation, the values of τ_{wi} and τ_{wo} can be further determined based on the values the skin friction coefficients (C_{fi} and C_{fo}) at the inner the outer cylinder walls, respectively. Two nominal Reynolds numbers are tested, i.e. $Re_{D_h} = 8900$ and 17700. In order to set up the numerical simulation, we used the skin friction coefficient values given in the DNS study of Chung et al. (2002) for the lower Reynolds number case of $Re_{D_h} = 8900$, which is $C_{fi} = 0.00941$ and $C_{fo} = 0.00849$ at the inner and outer cylinder walls, respectively. From Eq. (2.4), it is straightforward that the value of the mean streamwise pressure gradient can be alternatively determined

as $\Pi = -C_f \rho U_b^2 / (R_o - R_i)$, based on the averaged friction coefficient defined as $C_f = C_{f_i} R_i / (R_i + R_o) + C_{f_o} R_o / (R_i + R_o)$. The value of C_f can be determined from the empirical equation given by Nouri et al. (1993), i.e. $C_f = 0.36(Re_{D_h})^{-0.39}$. We used this method to set up the numerical simulation for the higher Reynolds number case of $Re_{D_h} = 17700$. Test runs were conducted and minor adjustments to the value of Π were made to ensure that the value of Re_{D_h} calculated from DNS converges to its nominal value within a reasonable range of error tolerance. As is clear in Table 2.2, the values of Re_{D_h} calculated from DNS of cases of relatively large domains (such as cases A3-A6, B3, B4, C and D) are satisfactory, which have a very small error of less than 0.4% in comparison with the nominal Reynolds values (of $Re_{D_h} = 8900$ and 17700). However, the values of Re_{D_h} calculated from DNS of cases of small domain sizes (such as cases A1, A2, B1 and B2) are less satisfactory. The values of Re_{D_h} as well as U_b calculated from the DNS are determined by the mean velocity field, and the influence of domain size on the predictive accuracy of DNS on the mean velocity field will be examined systematically in the following section.

2.2 Turbulence statistics in physical space

2.2.1 Mean velocity

Figure 2.3(a) compares the mean velocity profiles of A-, B-, C- and D-series test cases along with the DNS data of Chung et al. (2002) under the testing conditions of two nominal Reynolds numbers of $Re_{D_h} = 8900$ and 17700. To facilitate a fair comparison between the convex and concave sides, the mean axial velocity is plotted in the “global coordinate” (non-dimensionalized by one-half the cylinder gap δ), i.e. $(r - R)/\delta$, and scaled based on the mean friction velocity u_τ . The distributions of the mean axial velocity is asymmetric in the radial direction, which is a distinctive feature of a concentric annular pipe flow. As is evident in Fig. 2.3(a), for the lower nominal

Reynolds number cases, the velocity profiles collapse well for cases A2-A6 and B2-B4. An excellent agreement between the results of case C and the reference data of case Ca is observed, which confirms the predictive accuracy of the computer code in terms of the generation of reliable DNS data of the mean velocity of the concentric turbulent annular pipe flow. However, from Fig. 2.3(a), it is seen that the value of the mean axial velocity $\langle u_z \rangle^+$ is slightly overpredicted by about 2.7% in case A1 and slightly underpredicted by 1.3% in cases B1, respectively. As shown in Table 2.1, case A1 has the smallest axial domain size (which is $L_z = \pi\delta$) and case B1 has the smallest azimuthal domain size (which is $L_\theta = \pi/6$). This indicates that if we solely focus on the mean velocity profiles and accept an arbitrary error tolerance up to 3%, it would be very tempting to conclude that the axial and azimuthal domain sizes $L_z = \pi\delta$ and $L_\theta = \pi/6$ are sufficient for conducting DNS of the current concentric annular pipe flow. In other words, the criterion based on the predictive accuracy of the first-order statistical moment of the velocity field can be very tolerant, and literally, all 12 test cases of the lower nominal Reynolds number can well predict the value of $\langle u_z \rangle^+$. However, in the following sections, it will be shown that this conclusion is, in fact, incorrect with respect to the prediction of the second-order statistical moments and spectral analysis of the velocity field.

It should be indicated that the above observations were made by investigating the effects of the axial and azimuthal domain sizes independently through A- and B-series test cases. The reason that cases A1 fails is that its domain size $L_z = \pi\delta$ is too small to capture the characteristic axial length scales of flow structures, and similarly, case B1 fails because its azimuthal domain size is too small to capture the characteristic azimuthal length scales of flow structures. Therefore, the performance of a combined case of $\pi\delta \times \pi/6 \times 2\delta$ is expected to be even worse, as it is too small to capture flow structures in both axial and azimuthal directions. Later in section 2.3, concrete evidence will be provided to support this physical analysis. We will explain rigorously why these two small axial and azimuthal domain sizes ($L_z = \pi\delta$ and

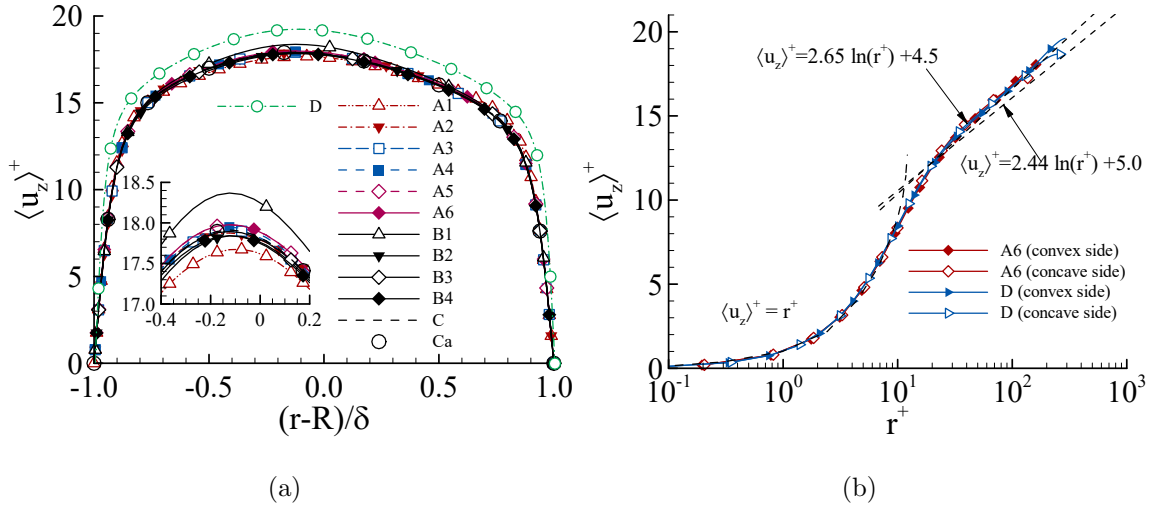


Figure 2.3: Profiles of the mean axial velocity $\langle u_z \rangle^+$. (a) in global coordinate for A-, B-, C- and D-series test cases, and (b) in wall coordinate for cases A6 and D. To facilitate the comparison of cases of the lower nominal Reynolds number, their profiles are partially enlarged and shown in an inset graph in (a).

$L_\theta = \pi/6$) fail to capture the characteristic wavelengths of the most energetic eddies, either independently or in combination, through analyses of 1D and 2D premultiplied spectra of turbulence.

Figure 2.3(b) compares the profiles of the mean axial velocity on the convex and concave sides of cases A6 and D for two different nominal Reynolds numbers of $Re_{D_n} = 8900$ and 17700 . Among the twelve A-, B- and C-series test cases for the lower nominal Reynolds number, case A has the longest axial domain size of $L_z = 30\pi\delta$ and a full azimuthal domain size of $L_\theta = 2\pi$. As such, the influence of the axial domain size on the numerical results is the minimum, and the influence from the azimuthal domain size is completely shielded off. The exceptionally large computational domain of case A6 is also the largest in the current literature for concentric annular pipe flows, which is five times that used by Chung et al. (2002) under a similar testing condition. The DNS result of the velocity field is the most accurate in case A6, and here we use this test case to demonstrate the transverse curvature effect on the wall scaling of the mean axial velocity profile. To this purpose, the mean axial velocity and wall

coordinates are scaled based on the local wall friction velocities of the convex ($u_{\tau i}$) and concave ($u_{\tau o}$) walls in Fig. 2.3(b). The profile of the standard law-of-the-wall based on von Kármán’s two-layer model for a zero-pressure-gradient (ZPG) boundary layer over a flat plate is also displayed for the purpose of comparison.

From Fig. 2.3(a), it is seen that as the nominal Reynolds number increases from $Re_{D_h} = 8900$ to 17700, the magnitude of $\langle u_z \rangle^+$ increases slightly when they are displayed in the global coordinate $(r - R)/\delta$. However, the profiles of $\langle u_z \rangle^+$ of these two Reynolds numbers collapse once they are plotted in wall coordinate r^+ in Fig. 2.3(b). Apparently, the velocity magnitudes on both concave and convex sides of the concentric pipe are slightly larger than that prescribed by the classical log-law for a ZPG boundary layer over a flat plate, $\langle u_z \rangle^+ = 2.44 \ln(r^+) + 5.0$. Furthermore, through a linear regression analysis, it is observed that the velocity profiles at two Reynolds number collapse well on a log-law of $\langle u_z \rangle^+ = 2.65 \ln(r^+) + 4.5$. Owing to the curvature difference between the two cylinder surfaces, the mean velocity profile of concentric annular pipe flow is asymmetrical in the radial direction (Fig. 2.3(a)), which leads to differences in the velocity profiles plotted in the wall coordinates measured from the convex and concave walls in Fig. 2.3(b). From Fig. 2.3(b), it is clear that the differences are the most apparent in the channel center. This is because not only the values of $u_{\tau i}$ and $u_{\tau o}$ are different (with $u_{\tau i}/u_{\tau o} = 1.057$), but also the peak position of $\langle u_z \rangle^+$ deviates from the domain center of $(r - R)/\delta = 0$. Specifically, from Fig. 2.3(a) and Table 2.2, it is seen that the profile of $\langle u_z \rangle^+$ peaks at $(r - R)/\delta = -0.119$. In the following, the mechanism underlying the shift of the peak position of $\langle u_z \rangle^+$ towards the inner cylinder wall will be further analyzed from the point of view of the balance of viscous and turbulent shear stresses.

2.2.2 Reynolds stresses

Figures 2.4 and 2.5 show the profiles of all four non-trivial Reynolds stresses at two nominal Reynolds numbers of $Re_{D_h} = 8900$ and 17700 (including the reference

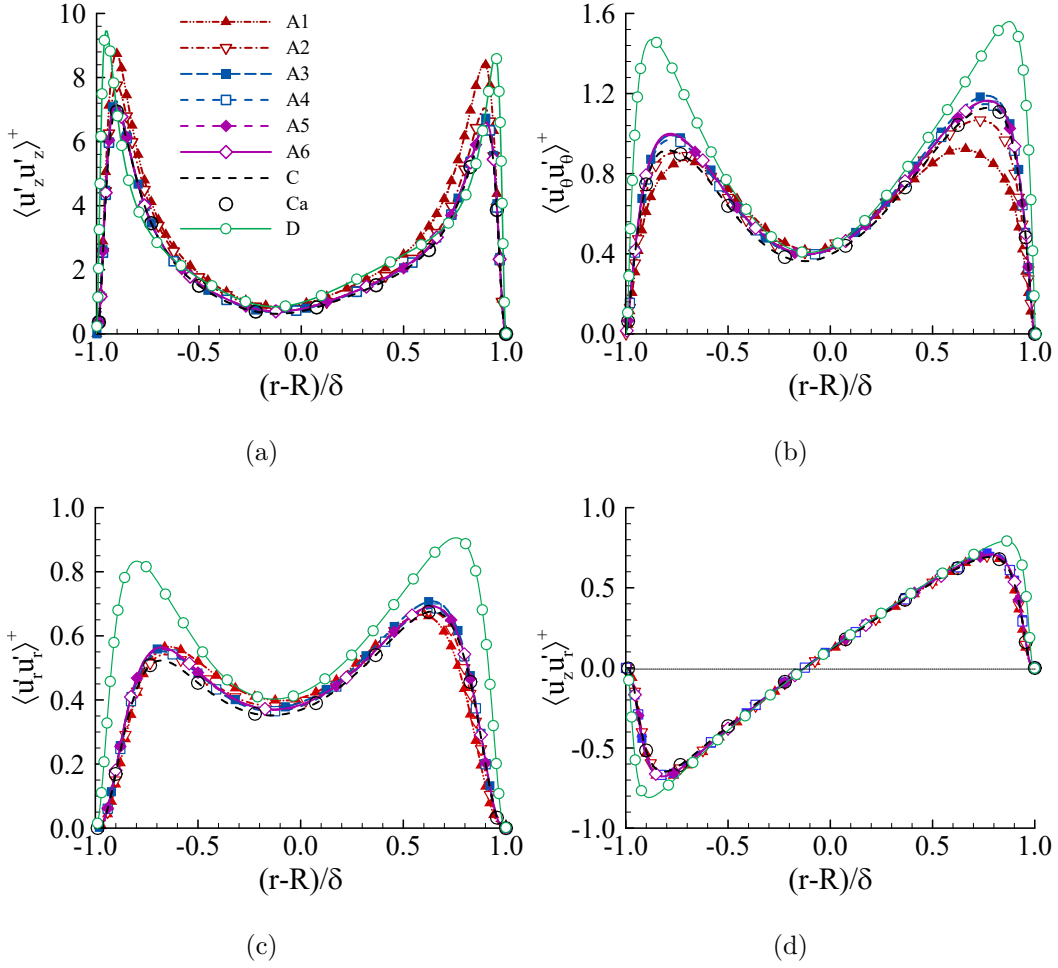


Figure 2.4: Profiles of Reynolds stresses $\langle u'_i u'_j \rangle^+$ predicted based on various computational domain sizes of the A-series test cases in comparison with those of the C- and D-series test cases. (a) $\langle u'_z u'_z \rangle^+$, (b) $\langle u'_\theta u'_\theta \rangle^+$, (c) $\langle u'_r u'_r \rangle^+$, and (d) $\langle u'_z u'_r \rangle^+$.

case Ca) in the global coordinate. In order to facilitate a clear comparison of all 14 test cases under the influences of different axial and azimuthal domain sizes and Reynolds numbers, the results of A-series test cases are compared with those of C- and D-series test cases in Fig. 2.4, while those of B-series test cases are compared with those of C- and D-series test cases in Fig. 2.5. All Reynolds stresses have been non-dimensionalized by the mean wall friction velocity (u_τ). From Figs. 2.4 and 2.5, it is apparent that the profiles of all Reynolds normal and shear components are asymmetrical in the radial direction at both Reynolds numbers. By comparing the

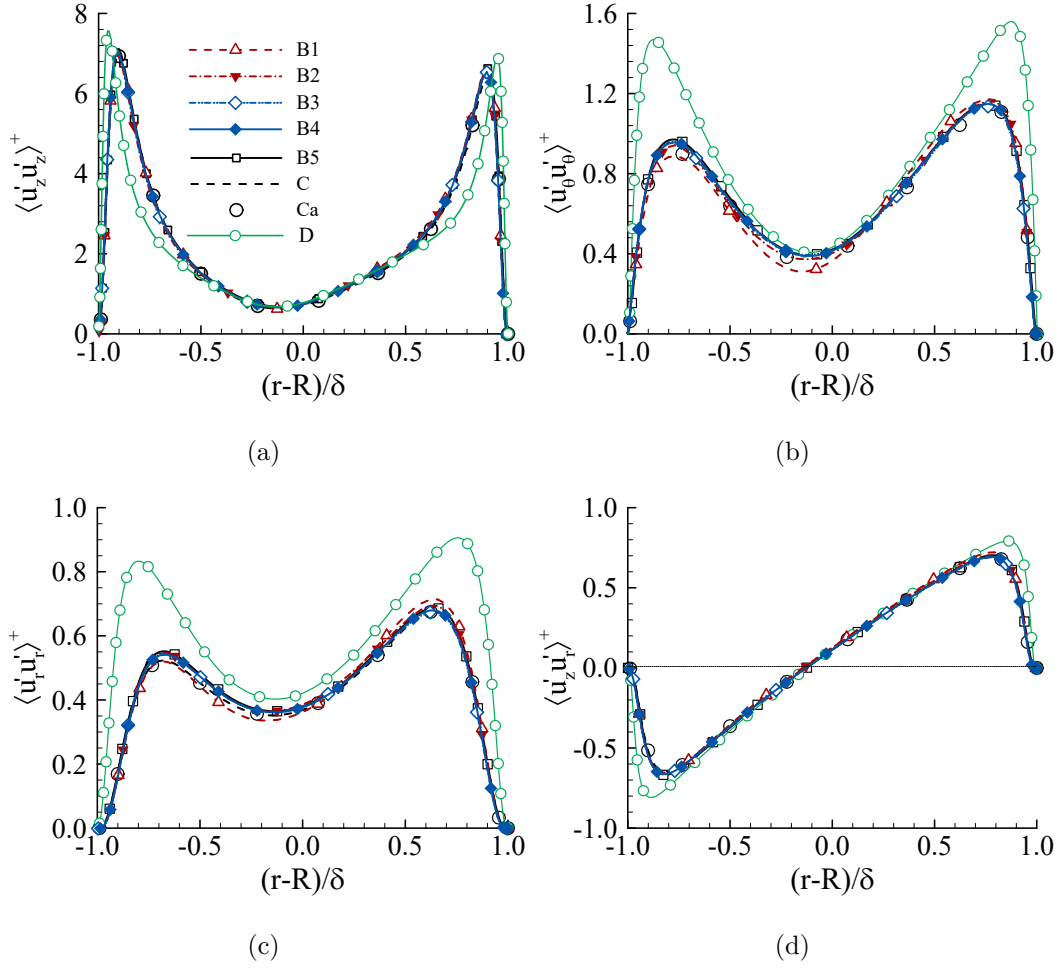


Figure 2.5: Profiles of Reynolds stresses $\langle u'_i u'_j \rangle^+$ predicted based on various computational domain sizes of the A-series test cases in comparison with those of the C- and D-series test cases. (a) $\langle u'_z u'_z \rangle^+$, (b) $\langle u'_\theta u'_\theta \rangle^+$, (c) $\langle u'_r u'_r \rangle^+$, and (d) $\langle u'_z u'_r \rangle^+$.

results of cases C and Ca, it is evident that in either Fig. 2.4 or Fig. 2.5, the profiles of Reynolds normal and shear stresses obtained in the current DNS agree well with those of Chung et al. (2002). In Fig. 2.4, the Reynolds stress profiles of the A-series test cases collapse except for cases A1 and A2. As is seen in Fig. 2.4a, the magnitudes of the axial Reynolds normal stress of cases A1 and A2 are over-predicted in the near-wall region on both sides of the concentric annular pipe. Meanwhile, Fig. 2.4b shows that in cases A1 and A2, not only the value of $\langle u'_\theta u'_\theta \rangle^+$ is underpredicted, but also the locations of the near-wall peaks on both sides of the concentric annular pipe

are incorrectly predicted, which shift towards the center of the channel. In view of this, it is concluded that in order to correctly predict the Reynolds stress level, the minimal axial computational domain size must be kept at $L_z = 6\pi\delta$ (or approximately, $L_z^+ = 2800$). The influence of azimuthal computational domain size on the predictive accuracy of Reynolds stresses can be identified by comparing the DNS results of the five B-series cases with those of cases C and Ca at a lower nominal Reynolds number of $Re_{D_h} = 8900$ in Fig. 2.5. From Fig. 2.5a, it is observed that the prediction of the profile of $\langle u'_z u'_z \rangle^+$ is satisfactory, which is in an excellent agreement with the results of cases C and Ca in all five B-series cases. However, as is clear from Figs. 2.5b and 2.5c, the values of $\langle u'_\theta u'_\theta \rangle^+$ and $\langle u'_r u'_r \rangle^+$ of case B1 are underpredicted on the convex side and in central region of the concentric annular passage. Clearly, based on the prediction of Reynolds stresses, the minimal azimuthal computational size must be stretched from $L_\theta = \pi/6$ (which is the previous conclusion based on the prediction of the mean axial velocity profiles shown in Fig. 2.3) to $L_\theta = \pi/4$.

From Figs. 2.4 and 2.5, it is seen that the Reynolds number has a significant influence on the predicted value of Reynolds stresses. Clearly, as the nominal Reynolds number increases from $Re_{D_h} = 8900$ to 17700, the magnitudes of $\langle u'_\theta u'_\theta \rangle^+$ and $\langle u'_r u'_r \rangle^+$ vary significantly. By contrast, those of $\langle u'_z u'_z \rangle^+$ and $\langle u'_z u'_r \rangle^+$ are less sensitive. Furthermore, it is interesting to observe from both Figs. 2.4d and 2.5d that the Reynolds shear stress $\langle u'_z u'_r \rangle^+$ is the least sensitive to the axial and azimuthal computational domain sizes. A further study of the transport equation of the mean axial velocity facilitates a better understanding of this invariant behavior of the Reynolds shear stress. Considering that the flow is statistically stationary and homogeneous in the r - θ cylindrical surface, the following equation that expresses the viscous and turbulent shear stresses can be derived from the momentum equation:

$$\frac{\tau_{\text{tot}}}{\rho} = \nu \frac{d\langle u_z \rangle}{dr} - \langle u'_z u'_r \rangle = \frac{\Pi}{2\rho} r + \frac{D}{r} \quad , \quad (2.5)$$

where τ_{tot} denotes the total shear stress (as the summation of the viscous and turbu-

lent shear stresses), and D is a constant of integration given as

$$D = \frac{R_o^2 R_i u_{\tau i}^2 + R_i^2 R_o u_{\tau o}^2}{R_o^2 - R_i^2} \quad . \quad (2.6)$$

From Eq. (2.5), it is straightforward that at the radial position of $r = r_m = \sqrt{-2\rho D/\Pi}$, the total shear stress vanishes, i.e. $\tau_{\text{tot}} = 0$. Consequently, $\nu d\langle u_z \rangle/dr - \langle u'_z u'_r \rangle = 0$. In other words, at radial position r_m , if $\langle u'_z u'_r \rangle = 0$, then it is guaranteed that $d\langle u_z \rangle/dr = 0$; or vice versa. From this analysis, it is clear that the radial position for zero Reynolds shear stress is strictly collocated with that for the maximum of mean velocity (where $d\langle u_z \rangle/dr = 0$) at radial position r_m in a concentric annular pipe flow. The above analytical approach for deriving this conclusion is not complex, however, it helps to clear the disagreement on this issue seen in the literature (as reviewed in section 1.1). Now we can say with certainty that, the experimental observations of Knudsen and Katz (1950) and Brighton and Jones (1964) and DNS results of Boersma and Breugem (2011) are accurate on this issue. The thicknesses of boundary layers developed over the inner and outer cylinder walls are different to reflect the difference in the surface curvature of these two walls, and their values can be determined as $\delta_{ti} = \delta + r_m$ and $\delta_{to} = \delta - r_m$, respectively. The values of δ_{ti} and δ_{to} calculated from DNS for all test cases are presented in Table 2.2.

To further verify the above analysis using DNS, the shear stress balance of case A6 (which has the largest computational domain) is shown in Fig. 2.6. This figure shows the profiles of the mean axial velocity, viscous Reynolds shear stress $\tau_{\text{vis}}/\rho = \nu d\langle u_z \rangle/dr$, turbulent Reynolds shear stress $\tau_{\text{tur}}/\rho = -\langle u'_z u'_r \rangle$, and total Reynolds shear stress $\tau_{\text{tot}} = \tau_{\text{vis}} + \tau_{\text{tur}}$. In Fig. 2.6, all shear stress terms have been non-dimensionalized using the mean friction velocity. Clearly, at the radial position demarcated by the black dashed line, the axial mean velocity $\langle u_z \rangle$ reaches its maximum, and Reynolds shear stress $\langle u'_z u'_r \rangle$ becomes zero concurrently. Specifically, at the lower nominal Reynolds number $Re_{D_h} = 8900$, the radial position where $\tau_{\text{tot}}^+ = 0$, $\langle u'_z u'_r \rangle^+ = 0$ and $d\langle u_z \rangle/dr = 0$, deviates from the domain center and occurs instead

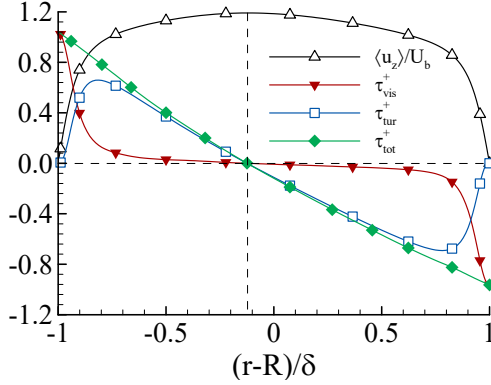


Figure 2.6: Profiles of the mean axial velocity $\langle u_z \rangle$ and budget balance of total shear stress ($\tau_{\text{tot}} = \tau_{\text{vis}} + \tau_{\text{tur}}$) displayed in the global coordinate based on the DNS results of case A6. Considering the large differences in their absolute magnitudes, the mean axial velocity $\langle u_z \rangle$ is non-dimensionalized using the bulk mean velocity U_b , while the shear stresses are non-dimensionalized based on the mean wall friction velocity u_τ .

at $(r - R)/\delta = -0.119$. Further from Table 2.2, it can be inferred that this special radial position remains almost unchanged as the nominal Reynolds number increases to $Re_{D_h} = 17700$, which is located at $(r - R)/\delta = -0.118$.

2.2.3 Higher-order statistics

Thus far, the effects of surface curvature and Reynolds number on the turbulent flow field have been examined through the first- and second-order flow statistics. In order to develop a deeper understanding of these effects on the transport of momentum, the third- and fourth-order statistical moments of the velocity field can be examined. Because the higher-order statistical moments of the velocity field are more sensitive than the lower-order ones in the calculations, we restrict our examination of the domain size effects on the predictive accuracy of DNS to the study of the first- and second-order statistical moments (e.g., mean velocity, Reynolds stresses, two-point correlations, and energy spectra) in both physical and spectral spaces, which represents a usual practice in the literature on the study of the minimum domains for DNS Jiménez and Moin (1991); Yang and Wang (2018). In the following, we focus

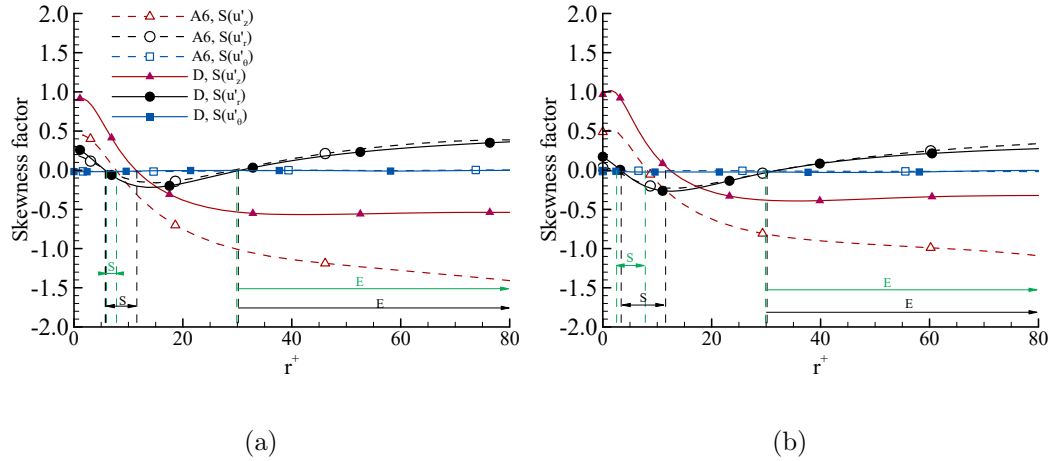


Figure 2.7: Skewness factors of the velocity field on the convex and concave sides of the concentric annular pipe for cases A6 and D. (a) convex side, and (b) concave side. The vertical dashed lines demarcate the zero-crossing points of the skewness factors for $S(u'_z) = 0$ and $S(u'_r) = 0$. Near-wall regions featuring the sweeping and ejection events are labeled using “S” and “E”, in either green or black color corresponding to either case A6 or D, respectively. The skewness factor of the ideal Gaussian distribution is also plotted using a thin dashed line, which is $S(u'_i) \equiv 0$.

our attention on the physics of the flow while we study the properties of the skewness and flatness factors. Specifically, we intend to examine the Reynolds number effects on the skewness and flatness factors by comparing their values of cases A6 and D; and furthermore, we study the curvature effects on the skewness and flatness factors by comparing their values on the convex and concave sides of the concentric annular pipe. The velocity skewness and flatness factors are defined as Kim et al. (1987):

$$S(u'_i) = \frac{\langle u_i'^3 \rangle}{\langle u_i'^2 \rangle^{3/2}} \quad \text{and} \quad F(u'_i) = \frac{\langle u_i'^4 \rangle}{\langle u_i'^2 \rangle^2} \quad , \quad (2.7)$$

respectively. Figures 2.7 and 2.8 compare the skewness and flatness factors of all three velocity fluctuating components at two nominal Reynolds numbers of $Re_{D_h} = 8900$ and 17700 through cases A6 and D.

For turbulence signals obeying the ideal Gaussian distribution, $S(u'_i) \equiv 0$. From Fig. 2.7, it is clear the value of the skewness factor of azimuthal velocity fluctuations follows the Gaussian distribution (i.e., $S(u'_\theta) = 0$), which reflects the fact that flow is

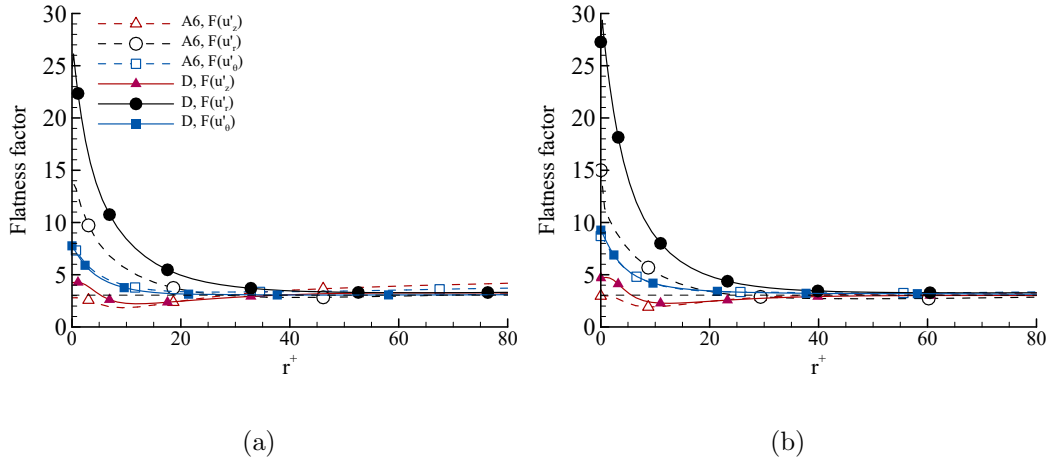


Figure 2.8: Flatness factors of the velocity field on the convex and concave sides of the concentric annular pipe for cases A6 and D. (a) convex side, and (b) concave side. The flatness factor of the ideal Gaussian distribution is also plotted using a thin dashed line, which is $F(u'_i) \equiv 3$.

statistically axial-symmetric, and therefore, homogeneous in the azimuthal direction. However, the skewness factors of the other two components ($S(u'_z)$ and $S(u'_r)$) of the velocity field deviate significantly from the Gaussian distribution as a result of wall anisotropy. As the nominal Reynolds number increases from $Re_{D_n} = 8900$ to 17700, the amplitude of $S(u'_r)$ varies little, but that of $S(u'_z)$ increases significantly.

The flow physics are dominated by sweeping and ejection events on near both convex and concave cylinder walls, although the strengths of these events are different due to the difference in the surface curvature of the two cylinders. The ejection events are characterized by $S(u'_z) < 0$ and $S(u'_r) > 0$, while the sweeping events are characterized by $S(u'_z) > 0$ and $S(u'_r) < 0$. The ejection and sweeping events are associated with the so-called “Q2” and “Q4” events in quadrant analysis of Reynolds stresses, respectively (Adrian, 2007). The quadrant analysis of Reynolds shear stresses can be conducted with respect to the sign of u'_i or u_i^3 . This is because $\text{sign}(u'_i) = \text{sign}(u_i^3)$. Therefore, sweeping and ejection events of a wall-bounded flow can be studied based on the skewness factor. In order to facilitate a clear discussion of near-wall ejection of sweeping events, regions corresponding to these two events are

delineated using vertical dashed lines, which go through the zero-crossing points of the skewness factors in the radial direction (at which $S(u'_z) = 0$ and $S(u'_r) = 0$). The Reynolds number effects on the sweeping and ejection events are evident, which occur within $r^+ \in [5, 8]$ and $r^+ \in [28, 134]$ on the convex cylinder side; but within $r^+ \in [3, 8]$ and $r^+ \in [30, 161]$ on the concave cylinder side, respectively, at the lower nominal Reynolds number of $Re_{D_h} = 8900$. As the Reynolds number increases to $Re_{D_h} = 17700$, the strengths of the ejection and sweeping events become stronger, as the magnitudes of both $S(u'_z)$ and $S(u'_r)$ increase. At $Re_{D_h} = 17700$, the sweeping and ejection events occur within $r^+ \in [5, 12]$ and $r^+ \in [30, 253]$ on the convex cylinder side; but within $r^+ \in [4, 12]$ and $r^+ \in [31, 302]$ on the concave cylinder side, respectively. From these numbers, it is clear that the profiles of $S(u'_z)$ and $S(u'_r)$ are asymmetrical in the wall-normal direction as a result of curvature difference between the convex and concave cylinder walls, a physical feature that is different from that the classical 2-D plane-channel flows Kim et al. (1987). In fact, this asymmetrical feature can be easily seen by directly comparing Figs. 2.7a and 2.7b, which show that the amplitudes of $S(u'_z)$ and $S(u'_r)$ in these two figures are different at the same radial position r^+ .

From Fig. 2.8, it is clear that the flatness factors of all three components of velocity fluctuations peak at the wall, a pattern that is a characteristic of near-wall turbulence also observed in the classical turbulent plane-channel flows (Kim et al., 1987). The magnitude of $F(u'_i)$ is the largest near the wall, and gradually converges to $F(u'_i) = 3$ as the distance from wall increases, which is the theoretical value for the Gaussian distribution. The Reynolds number effects on the flatness factor is evident. As the nominal Reynolds number increases from $Re_{D_h} = 8900$ to 17700, the amplitude of $F(u'_\theta)$ varies little, but those of $F(u'_r)$ and $F(u'_z)$ increase significantly. Furthermore, by comparing Figs. 2.8a and 2.8b, it is clear that the magnitude of the $F(u'_i)$ is larger near the concave side than near the convex side in general, as a result of the curvature difference between the inner and outer cylinder walls.

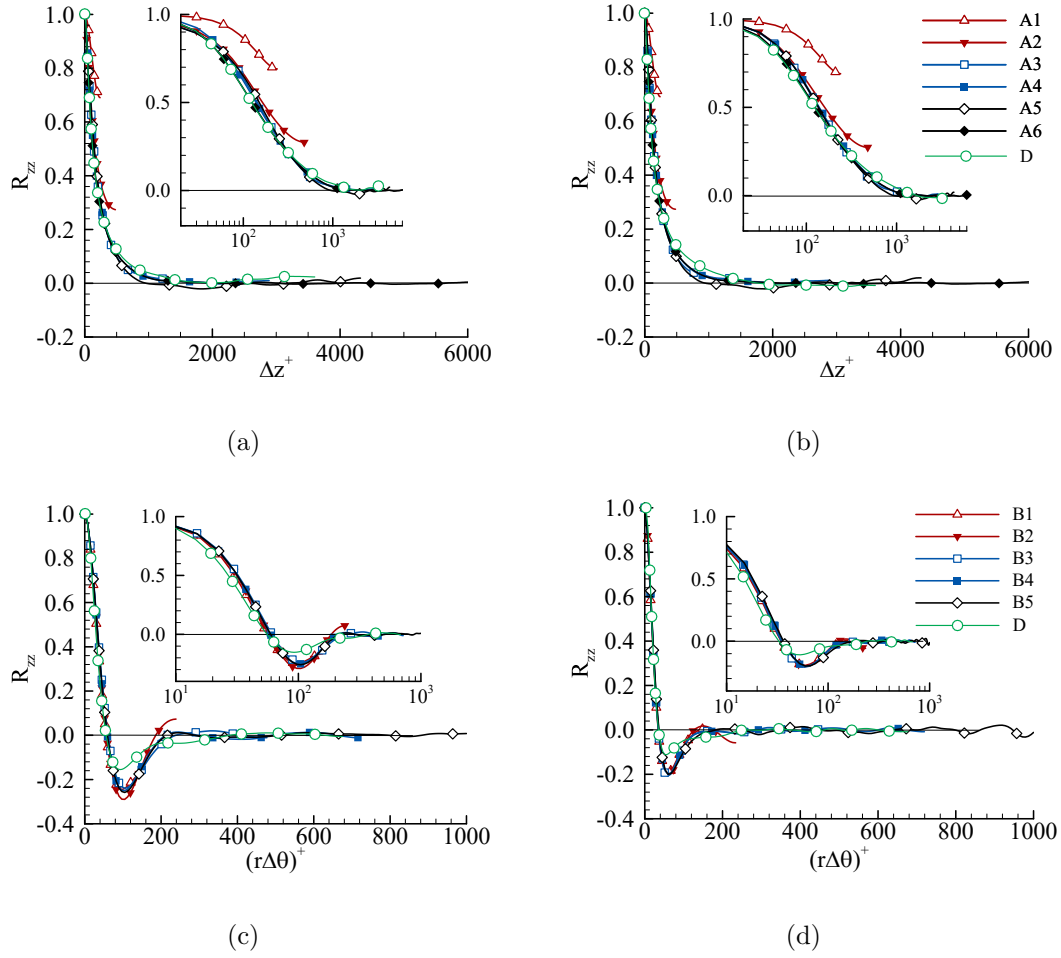


Figure 2.9: Profiles of normalized two-point correlation coefficient R_{zz} of the axial velocity fluctuations (u'_z) calculated over the cylindrical surface located at $r^+ = 15$ from the convex and concave walls, where the Reynolds normal stress $\langle u'_z u'_z \rangle$ reaches its peak value. (a) axial correlations for A- and D-series test cases (convex side), (b) axial correlations for A- and D-series test cases (concave side), (c) azimuthal correlations for B- and D-series test cases (convex side), and (d) azimuthal correlations for B- and D-series test cases (concave side).

2.2.4 Two-point correlation

Two-point correlation is a conventional tool for studying the adequacy of the computational domain size as well as the length scales of coherent structures. The axial and azimuthal 1D two-point correlation functions for the axial velocity fluctuations

are defined as

$$R_{zz}(\Delta z) = \frac{\langle u'_z(z, r\theta, r, t)u'_z(z + \Delta z, r\theta, r, t) \rangle}{\langle u'_z(z, r\theta, r, t)u'_z(z, r\theta, r, t) \rangle}, \quad (2.8)$$

and

$$R_{zz}(r\Delta\theta) = \frac{\langle u'_z(z, r\theta, r, t)u'_z(z, r\theta + r\Delta\theta, r, t) \rangle}{\langle u'_z(z, r\theta, r, t)u'_z(z, r\theta, r, t) \rangle}, \quad (2.9)$$

respectively.

Figures 2.9(a) and 2.9(b) compare the profiles of the axial 1D two-point correlation coefficient $R_{zz}(\Delta z)$ of the A-series test cases calculated over the cylindrical surface positioned at $r^+ = 15$ from the convex and concave walls, where Reynolds normal stress $\langle u'_z u'_z \rangle^+$ reaches its peak value. Given their overly short axial domain sizes, the correlation coefficient curves of cases A1 and A2 end with finite values far above $R_{zz}(\Delta z) = 0$, clearly suggesting insufficiency of the axial domain sizes to justify the use of the assumption of periodic boundary condition in these two test cases. By contrast, the two-point correlation coefficients of cases A3–A6 fall to $R_{zz}(\Delta z) = 0$ at $\Delta z^+ \approx 1000$. This indicates that a minimum domain of $L_z = 6\pi\delta$ (of case A3) is, indeed, required to capture the length scale of axial turbulent flow structures. Figures 2.9(c) and 2.9(d) compare the azimuthal 1D two-point correlation $R_{zz}(r\Delta\theta)$ at $r^+ = 15$ on the convex and concave sides, respectively. The value of $R_{zz}(r\Delta\theta)$ becomes negative and reaches its minimum at $(r\Delta\theta)^+ \approx 60$ and $(r\Delta\theta)^+ \approx 90$ on the convex and concave sides, respectively. This indicates that the mean spacing between the near-wall streaks is smaller on the concave side and larger on the convex side due to the curvature difference between these two cylinder walls. The value of $R_{zz}(r\Delta\theta)$ does not end with zero in cases B1 and B2, suggesting that the azimuthal computational domain sizes are insufficient for accurately conducting DNS in these two cases. Based on the above analysis of the 1D two-point correlation coefficients and previous analysis of the first- and second-order flow statistics, it is tempting to conclude that the minimum computational domain should be kept at $L_z = 6\pi\delta$ and $L_\theta = \pi/2$ in order to capture the length scales of energetic eddy motions at the lower nominal Reynolds number of $Re_{D_h} = 8900$. This would lead to the conclusion that

the domain of cases C and Ca is proper. However, so far, our study (conducted in section 2.2) has been limited exclusively to the physical space based on the analysis of the first- and second-order statistical moments of the velocity field and 1D two-point correlation coefficients, $R_{zz}(\Delta z)$ and $R_{zz}(r\Delta\theta)$. It should be noted that the choice of the computational domain sizes purely based on evidences in the physical space may not be conclusive. To confirm, the study needs to be further refined by examining the characteristic wavelengths of turbulent flow structures in the spectral space. In fact, we will show in the following section that this suggested minimal domain (of $L_z = 6\pi\delta$ and $\theta = \pi/2$) is actually insufficient, a proper computational domain that allows for capturing the most energetic eddy motions is that of case B4 (of $L_z = 12\pi\delta$ and $L_\theta = 3\pi/4$) based on the analysis of the axial and azimuthal 1D premultiplied spectra of velocity fluctuations.

2.3 Turbulence structures and spectral analysis

2.3.1 Scales of hairpin structures and near-wall streaks

In a concentric annular pipe flow, the scales of energetic eddy motions are dominated by two types of coherent turbulent structures, i.e. near-wall streaks and hairpin structures. The presence of near-wall streaks represents a universal feature of wall-bounded turbulent flows. Figure 2.10 shows the near-wall streaks on the convex and concave sides at $r^+ = 15$, where the maximum turbulence kinetic energy (TKE) occurs. The near-wall streaks are visualized using non-dimensionalized axial velocity fluctuations $u_z'^+$, which show a persistent and regular pattern. From Fig. 2.10, it is clear that low- and high-speed streaky structures alternate and are uniformly distributed in the axial and azimuthal directions. As one of the most energetic near-wall flow structures, these energy-containing streaks are elongated in the axial direction, which need to be captured in DNS by using a properly sized axial domain. If the axial domain is too

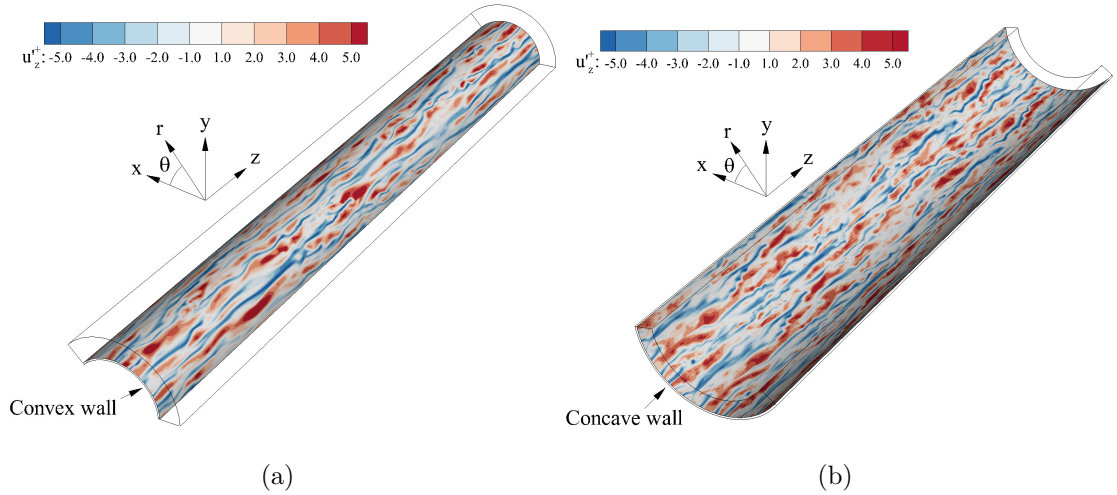


Figure 2.10: Contours of the non-dimensionalized axial velocity fluctuations u'_z+ of case B4, plotted at $r^+ = 15$ on the convex and concave sides, where the maximum TKE occurs. (a) convex side, and (b) concave side. The contours are colored using the magnitude of the instantaneous axial velocity fluctuations u'_z+ . To enhance the visual clarity of near-wall structures, only a portion of the computational domain of case B4 is plotted. The plotted domain sizes are $L_z = 6\pi\delta$ and $L_\theta = \pi/2$.

short to capture the streaky structures, the axial length scales of the streaks will be artificially chopped off or distorted, and consequently, the level of TKE contained by near-wall streaks cannot be accurately calculated by DNS.

In section 2.2, we studied the minimum domain size required for properly conducting DNS in the physical space based on analysis of a variety of flow statistics, including the two-point correlation coefficients. As is well known, energy spectra are closely related to two-point correlation coefficients, simply because they are counterparts of each other in Fourier transform. Different from two-point correlations, energy spectra can show precisely the turbulence energy level of flow structures at each specific wavelength, which in turn, facilitates identifying the characteristic length scale (wavelength) of turbulence structures at an arbitrary turbulence energy level. The axial and azimuthal length scales of coherent structures can be examined precisely through the analysis of premultiplied 2D energy spectrum, $k_z k_\theta \check{E}_{ii}$, where $\check{E}_{ii} = \check{E}_{ii}(k_z, k_\theta, r)$ is the 2D energy spectrum of velocity fluctuations in a homogeneous r - θ cylindrical

surface, defined as

$$\check{E}_{ii}(k_z, k_\theta, r) = \overline{2\widehat{u}'_i(k_z, k_\theta, r)\widehat{u}'_i{}^*(k_z, k_\theta, r)} \quad (2.10)$$

for $i = 1, 2$ or 3 (no summation convention implied). Here, an overline ($\overline{\quad}$) indicates time averaging, \widehat{u}'_i represents a Fourier coefficient of u'_i , $\widehat{u}'_i{}^*$ denotes its complex conjugate, and k_z and k_θ denote the axial and azimuthal wavenumbers, respectively. For discrete Fourier transform performed in a cylindrical coordinate system, these two wavenumbers are determined as $k_z = n_z k_{z0}$ and $k_\theta = n_\theta k_{\theta0}$ for $n_z \in [-N_z/2, N_z/2 - 1]$ and $n_\theta \in [-N_\theta/2, N_\theta/2 - 1]$, respectively. Here, $k_{z0} = 2\pi/L_z$ and $k_{\theta0} = 2\pi/(r \cdot L_\theta)$ are the lowest positive wavenumbers in the axial and azimuthal directions determined directly based on the domain sizes L_z and L_θ , respectively. The premultiplied 2D energy spectrum $k_z k_\theta \check{E}_{ii}$ is advantageous in identifying the characteristic wavenumbers (k_z and k_θ) of the most energetic eddies in a r - θ cylindrical surface. In our discussion, besides wavenumbers, we also use wavelengths to evaluate the length scales, which are defined as $\lambda_z = 2\pi/k_z$ and $\lambda_\theta = 2\pi/k_\theta$. Clearly, both k_z and λ_z are independent of r , but both k_θ and λ_θ are functions of r (because $k_{\theta0}$ is a function of r). Equation (2.10) can be alternatively expressed as a function of wavelengths as $\check{E}_{ii}(\lambda_z, \lambda_\theta, r) = \overline{2\widehat{u}'_i(\lambda_z, \lambda_\theta, r)\widehat{u}'_i{}^*(\lambda_z, \lambda_\theta, r)}$.

Figures 2.11(a)-2.11(d) display contours of premultiplied 2D energy spectra $k_z^+ k_\theta^+ \check{E}_{zz}^+$ of case B4 at two radial positions: close to the wall at $r^+ = 15$, where the axial component of TKE (i.e., $\langle u'_z u'_z \rangle$) peaks; and one quarter cylinder gap (or, $\delta/2$) away from the wall (i.e., $(R - r)/\delta = 0.5$ from the convex wall, or $(r - R)/\delta = 0.5$ from the concave wall). The flow structures at these two radial positions are qualitatively different in the sense that streaky structures are populated in the near-wall region around $r^+ = 15$, while hairpin packets are populated around the elevated position $\delta/2$ away from the convex or concave wall. In presenting results, the 2D energy spectrum, wavenumbers, and wavelengths have been non-dimensionalized using ν and local wall friction velocity (which equals to either $u_{\tau i}$ or $u_{\tau o}$ depending on the convex

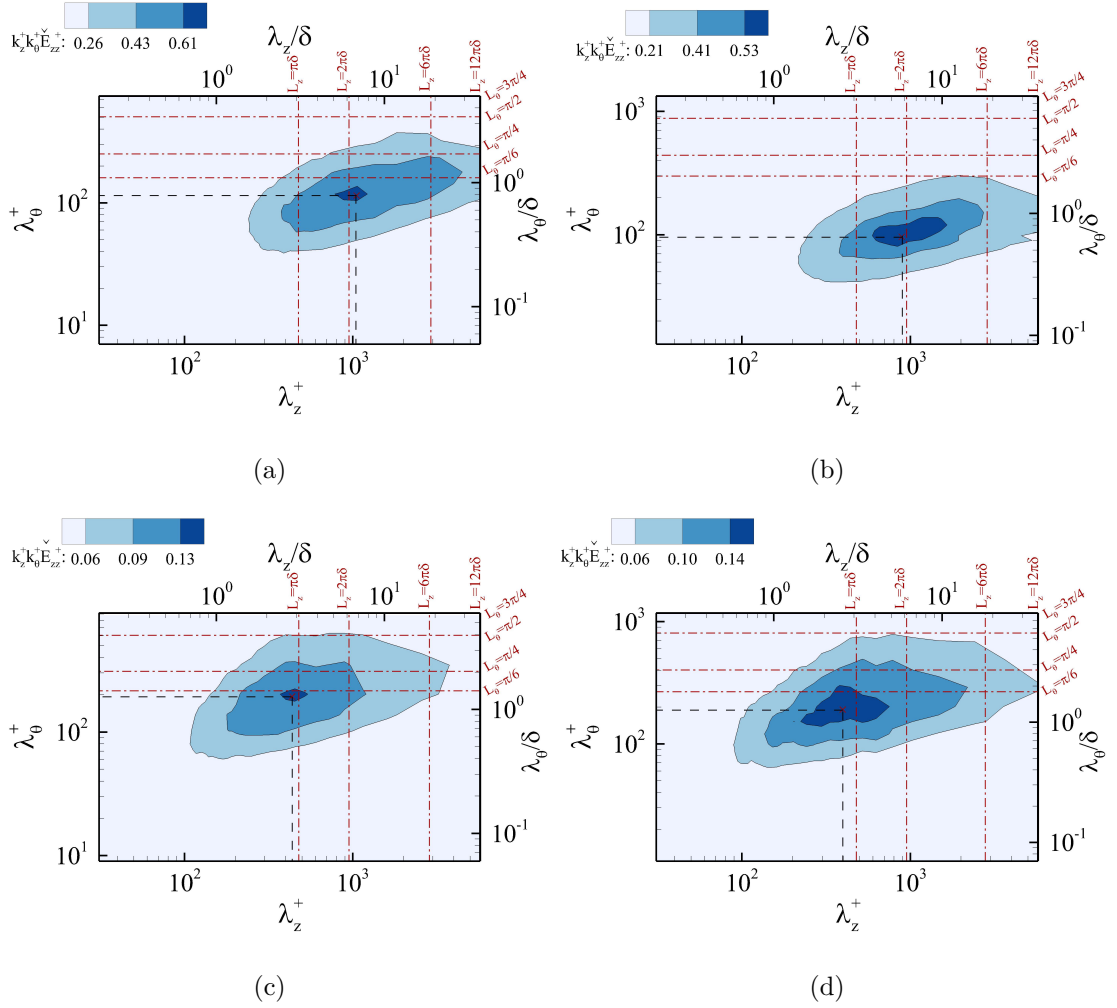


Figure 2.11: Premultiplied 2D spectra $k_z^+ k_\theta^+ \tilde{E}_{zz}^+$ of axial velocity fluctuations on the convex and concave sides of the concentric annular pipe for case B4, which vary with the axial and azimuthal wavelengths. (a) $r^+ = 15$ on the convex side, (b) $r^+ = 15$ on the concave side, (c) $(R - r)/\delta = 0.5$ on the convex side, and (d) $(R - r)/\delta = 0.5$ on the concave side. In each figure panel, the wavelength is given both as λ_z^+ (bottom) and as λ_z/δ (top). Similarly, the azimuthal coordinate is given both as λ_θ^+ (left) and as λ_θ/δ (right). The computational domain of case B4 (i.e., $L_z = 12\pi\delta$ and $L_\theta = 3\pi/4$) are shown as the boundaries in Fig. 2.11. For the purpose of comparison, smaller axial and azimuthal domain sizes used in other test cases are also labeled in the figure. The figure presentations are made at two radial positions: close to the wall at $r^+ = 15$, where $\langle u'_z u'_z \rangle^+$ peaks; and at one quarter the cylinder gap (or, $\delta/2$) away from the wall (i.e., $(R - r)/2 = 0.5$ from the convex wall or $(r - R)/2 = 0.5$ from the concave wall). Three energy levels are distinguished, and the innermost, intermediate and outermost isopleths correspond to $0.875 \max(k_z^+ k_\theta^+ \tilde{E}_{ii}^+)$, $0.625 \max(k_z^+ k_\theta^+ \tilde{E}_{ii}^+)$ and $0.375 \max(k_z^+ k_\theta^+ \tilde{E}_{ii}^+)$, respectively.

or concave side). These non-dimensionalized quantities are indicated using superscript “+” in consistency with the convention of wall coordinates. In Fig. 2.11, the spectrum maps show three regions of high-, intermediate- and low-intensity cores distinguished by colors, and their borders are shown using black solid lines corresponding to $0.875 \max(k_z^+ k_\theta^+ \check{E}_{zz}^+)$, $0.625 \max(k_z^+ k_\theta^+ \check{E}_{zz}^+)$ and $0.375 \max(k_z^+ k_\theta^+ \check{E}_{zz}^+)$ (or, 7/8-th, 5/8-th and 3/8-th the peak values of the non-dimensionalized premultiplied spectrum, respectively). The high-intensity core enclosed by the innermost isopleth of $0.875 \max(k_z^+ k_\theta^+ \check{E}_{zz}^+)$ corresponds to the most energetic eddies of the turbulent flow field. Although the low-intensity core (enclosed by the outermost isopleth of $0.375 \max(k_z^+ k_\theta^+ \check{E}_{zz}^+)$) corresponds to less dominant energetic eddies encompassing a large range length scales, it still contributes considerably to the total TKE of the flow.

Besides the three isopleths which show three magnitude levels of the premultiplied spectrum relative to its peak value, the absolute value of the non-dimensionalized premultiplied spectra is also indicated using a color legend in Fig. 2.11. The computational domain sizes of case B4 (i.e., $L_z = 12\pi\delta$ and $L_\theta = 3\pi/4$) are shown as the boundaries in Fig. 2.11. For the purpose of comparison, smaller axial and azimuthal domain sizes used in other test cases are also labeled in the figure. From Fig. 2.11, it is clear that both the innermost and intermediate isopleths (corresponding to $0.875 \max(k_z^+ \check{E}_{zz}^+)$ and $0.625 \max(k_z^+ \check{E}_{zz}^+)$, respectively) are fully captured. Furthermore, it is seen that the majority of the outermost isopleth of $0.375 \max(k_z^+ \check{E}_{zz}^+)$ is captured, with only a very small portion of the isopleth missing in Figs. 2.11(a) and 2.11(b). Based on this analysis of premultiplied 2D spectra $k_z^+ k_\theta^+ \check{E}_{zz}^+$, it is confirmed that the computational domain of case B4 (with $L_z = 12\pi\delta$ and $L_\theta = 3\pi/4$) is satisfactory in general, which can facilitate capture of large flow structures up to wavelengths that correspond to at least 37.5% of the peak value of the non-dimensionalized premultiplied 2D spectrum. By contrast, any arbitrary combination of smaller axial and azimuthal computational domain sizes would result in an inaccurate prediction of

large-scale structures with a higher percentage of TKE cutoff. For instance, as shown in Fig 2.11(c), if the “worst” combination of $L_z = \pi\delta$ and $L_z = \pi/6$ is used for conducting DNS, the domain is barely sufficient for capturing the peak of $k_z^+ k_\theta^+ \check{E}_{zz}^+$ but does not even allow for fully capturing the most energetic eddies of turbulence corresponding to the innermost isopleth of $0.875 \max(k_z^+ k_\theta^+ \check{E}_{zz}^+)$. The analysis conducted here is based on the premultiplied 2D spectra $k_z^+ k_\theta^+ \check{E}_{zz}^+$ at two special wall-normal positions of $r^+ = 15$ and $(r - R)/\delta = 0.5$. Later in sections 2.3.2 and 2.3.3, we will refine our study by further investigating the characteristic axial and azimuthal length scales of the most energetic turbulence structures over the entire wall-normal direction (i.e., the entire r -direction) through an analysis of their premultiplied 1D spectra.

Figures 2.11(a) and 2.11(b) show that the mode of $k_z^+ k_\theta^+ \check{E}_{zz}^+$ occurs at $\lambda_z^+ \approx 1100$ and $\lambda_\theta^+ \approx 120$ on the convex side, and at $\lambda_z^+ \approx 900$ and $\lambda_\theta^+ = 90$ on the concave side. These two modes represent the characteristic length scales (periods) of the streaky structures in the axial and azimuthal directions. The differences in the axial and azimuthal characteristic wavelengths on the convex and concave sides result from the surface curvature difference between the convex and concave cylinder walls. Apparently, both axial and azimuthal characteristic length scales of the streaks are larger on the convex side than on the concave side. This leads to an important conclusion that the challenge involved in accurately performing DNS of a concentric annular pipe flow mostly stems from the need of capturing large streaky structures on the convex side. Compared to the concave side, the streaky structures on the convex side are more elongated in the axial direction and more widely spread in the azimuthal direction. Although the characteristic length scales of near-wall streaky structures in a concentric annular pipe flow are sensitive to the surface curvature, their magnitudes are, in general, comparable to those of a plane-channel flow, which are approximately 1000 and 100 wall units in the streamwise and spanwise directions, respectively Kim et al. (1987); Chernyshenko and Baig (2005).

At a higher elevation of $\delta/2$ away from the convex and concave walls, the curvature effect on turbulence structures reduces, and the flow is dominated by hairpin packets. From Figs. 2.11(c) and 2.11(d), it is seen that the mode of $k_z^+ k_\theta^+ \tilde{E}_{zz}^+$ occurs approximately at $\lambda_z^+ = 405$ and $\lambda_\theta^+ = 190$ on both convex and concave sides. As is well known from the study of near-wall turbulent boundary layer over flat plates by Adrian (2007), hairpin structures constantly generate secondary hairpin vortices (SHV), develop into primary hairpin vortices (PHV) and are destroyed as downstream hairpin vortices (DHV). Figure 2.12 shows instantaneous contours of the swirling strength (for $\lambda_{ci} = 1.0$) of case B4. Similar to Fig. 2.10, only part of the computational domain is used for illustrating hairpin structures in Fig. 2.12. In addition, the domain is divided radially into two parts to clearly show the hairpin structures on the convex and concave sides. The hairpin structures identified by the swirling strength are further superimposed with colors corresponding to the value of non-dimensionalized instantaneous axial vorticity $\omega_z'^+$, with red and blue colors representing its positive and negative values, respectively. This facilitates identification of paired hairpin legs of counter-rotating directions. Figure 2.12 shows that hairpin structures are populated on both convex and concave sides of the concentric annular pipe, consisting of elongated legs (appearing as counter-rotating vortices, differentiated using the blue and red colors of $\omega_z'^+$) near the wall, and arches (or heads) at higher elevations relatively far away from the wall.

In order to demonstrate the spatial evolution of hairpin packets in the axial direction, a chain of hairpin structures on the concave side of the pipe are isolated from the surrounding flow structures in Fig. 2.12(b) using a green box and are shown separately by projecting the selected domain into a 2D z - r plane in Fig. 2.13(a). The hairpin structures displayed in Fig. 2.13(a) are magnified, showing a clear side view of the axial development of hairpin packets (consisting of PHV and SHV) on the concave side of the concentric pipe. The hairpin structures can be also studied based on a conditional averaging method described by Adrian (1994). Figure 2.13(b)

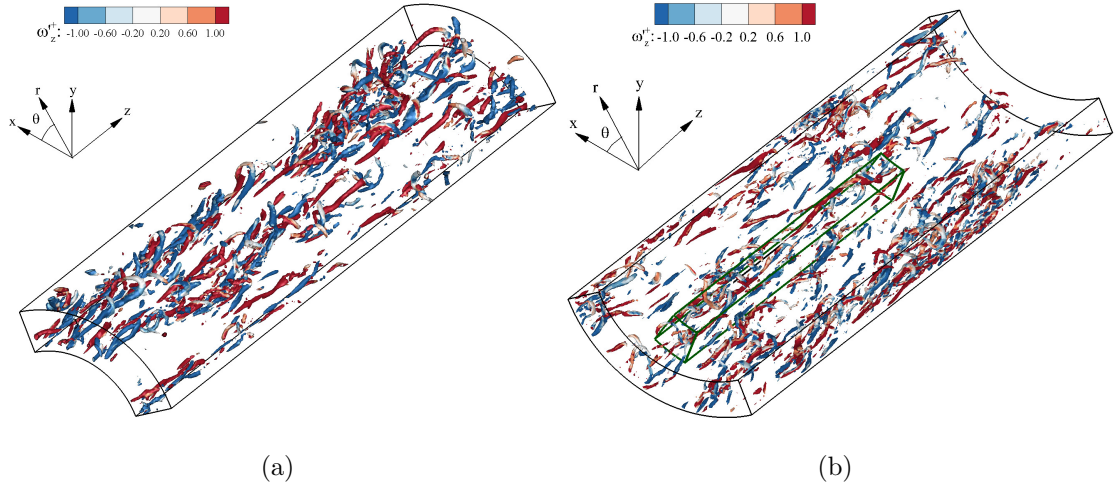


Figure 2.12: Contours of swirling strength ($\lambda_{ci} = 1.0$) for case B4. (a) convex side, and (b) concave side. The contours are colored with instantaneous axial vorticity ω_z^+ . To enhance the visual clarity of near-wall structures, only a portion of the computational domain is plotted for $L_z = 6\pi\delta$ and $L_\theta = \pi/2$.

shows the contours of $\langle u_z^+ | Q2 \rangle$, where the averaging of axial velocity fluctuations u_z' is done based on the condition of ejection events (or, the Q2 events which feature $u' < 0$ and $v' > 0$). The reason that u_z' is selected is that the length scales of large-scale streaky structures (or, the “legs” of hairpin structures) can be very effectively determined by the axial velocity fluctuations in either two-point coefficient analysis or 1D and 2D spectral analyses (see, Figs. 2.9, 2.10, 2.11, 2.14 and 2.15). From both Figs. 2.13(a) and 2.13(b), the periodicity of the hairpin packets can be readily identified (indicated using the thick dashed lines), with a period of approximately $\lambda_z^+ = 400$. This result is consistent with our previous analysis of the mode of premultiplied 2D spectrum $k_z^+ k_\theta^+ \check{E}_{zz}^+$ based on Fig. 2.11, which indicates that the axial characteristic wavelength of hairpin structures is approximately $\lambda_z^+ = 405$. The above analysis of large-scale turbulence structures (specifically, near-wall streaks and hairpin structures in core turbulent regions) was conducted based on premultiplied 2D spectra $k_z^+ k_\theta^+ \check{E}_{zz}^+(r^+, \lambda_z^+, \lambda_\theta^+)$ at two radial positions only. In order to develop a general understanding of the effect of radial position on the axial and azimuthal char-

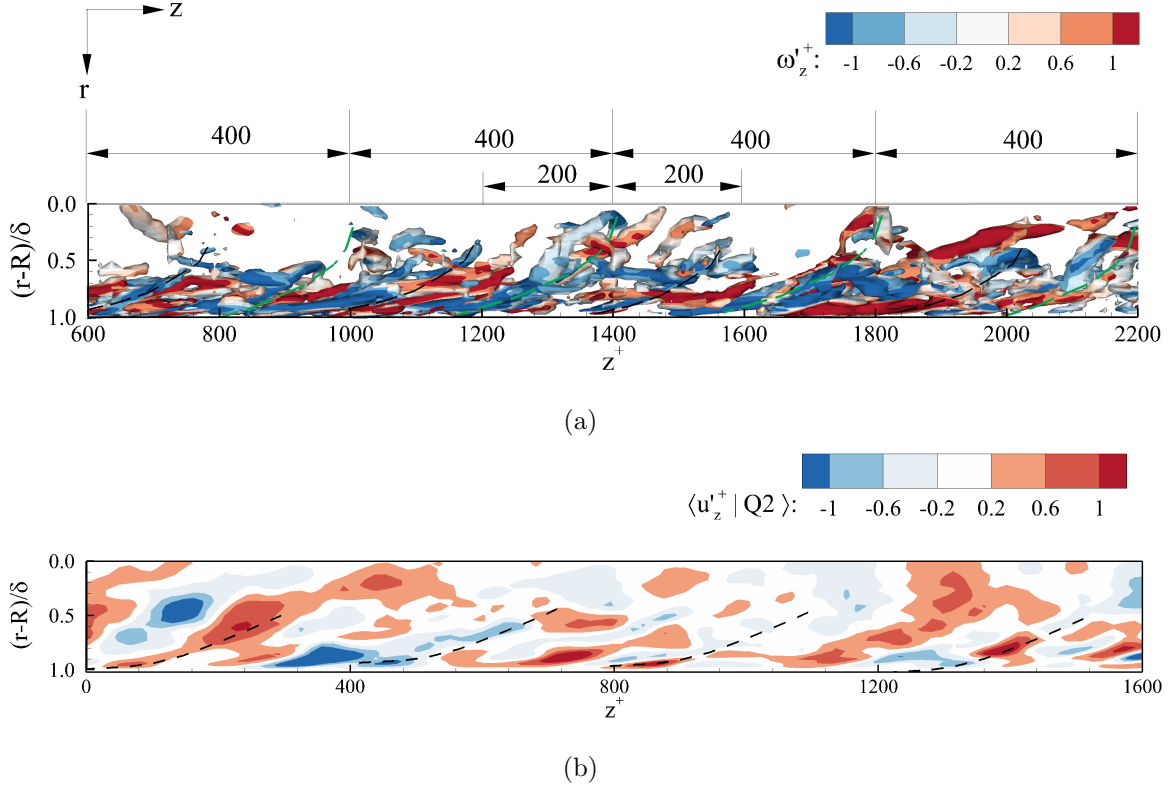


Figure 2.13: Side view of hairpin structures on the concave side of the concentric pipe for case B4. (a) contours of the swirling strength of $\lambda_{ci} = 1.0$ colored using the strength of $\omega_z'^+$, (b) contours of conditional averaging of axial velocity fluctuations $\langle u_z'^+ | Q2 \rangle$ in the $z-r$ plane located at $\theta = 0^\circ$. In panel (a), the hairpin structures are obtained by projecting the selected domain from Fig. 2.12(b) (indicated using a 3D green box) into a 2D $z-r$ plane here. The green and black dashed lines in panel (a) show the positions of the PHV and SHV, respectively. The wavelength of both PHV and SHV is approximately $\lambda_z^+ = 400$.

acteristic length scales of turbulence structures, in the following, we will refine the research by looking into the premultiplied 1D spectra as a function of r^+ and k_z^+ in section 2.3.2 and as a function of r^+ and k_θ^+ in section 2.3.3. In addition, through the study of characteristic length scales of turbulence structures using the premultiplied 1D spectra, we will further investigate the minimal axial domain size required for rigorously conducting DNS of concentric annular pipe flow and structures.

2.3.2 Axial premultiplied energy spectra

The 1D axial energy spectrum can be directly computed by integrating the 2D energy spectrum over the azimuthal wavenumbers, i.e.

$$\tilde{E}_{ii}(k_z, r) = \int \check{E}_{ii}(k_z, k_\theta, r) dk_\theta \quad , \quad (2.11)$$

or in a discrete form, as $\tilde{E}_{ii}(k_z, r) = k_{\theta 0} \sum_{k_\theta} \check{E}_{ii}(k_z, k_\theta, r)$ for $i = 1, 2$ or 3 (no summation convention implied). Due to the need of studying cases of different domain sizes (of different values of k_{z0} and $k_{\theta 0}$), the premultiplied 1D energy spectrum $k_z \tilde{E}_{ii}$ needs to be further normalized by the spectral area $k_{z0} k_{\theta 0}$ in our comparative study. Because case A6 has the largest computational domain size, its spectral results are the most accurate among all 12 test cases of the lower nominal Reynolds number of $Re_{D_h} = 8900$. Figure 2.14 compares the premultiplied 1D axial energy spectra of all three velocity fluctuation components on the convex and concave sides of case A6. For the purpose of comparison, vertical dash-dotted lines are used to demarcate the axial computational domain sizes of cases A3-A5, which vary from $L_z = 6\pi\delta$ to $18\pi\delta$. The premultiplied 1D energy spectrum has been non-dimensionalized using the local friction velocity, which equals to either $u_{\tau i}$ or $u_{\tau o}$ depending on the convex or the concave cylinder side in consideration. Similar to Fig. 2.11, three levels of the premultiplied energy spectrum are identified, which represent the high-, intermediate- and low-intensity cores of a turbulence structure. The contours for these three levels of the premultiplied spectrum are distinguished by colors and black solid borderlines corresponding to $0.875 \max(k_z^+ \tilde{E}_{ii}^+)$, $0.625 \max(k_z^+ \tilde{E}_{ii}^+)$ and $0.375 \max(k_z^+ \tilde{E}_{ii}^+)$.

Figures 2.14(a) and 2.14(b) compare the contour patterns of the non-dimensionalized premultiplied 1D spectrum of axial velocity fluctuations $k_z^+ \tilde{E}_{zz}^+$ on the convex and concave sides of the concentric annular pipe, as a function of the radius r^+ and wavelength λ_z^+ . The mode (indicated using a red cross symbol “ \times ” in the figure) of $k_z^+ \tilde{E}_{zz}^+$ occurs at $(r^+, \lambda_z^+) = (14.8, 1100)$ and $(r^+, \lambda_z^+) = (15.3, 900)$ on the convex and concave sides, respectively. Clearly, the characteristic axial length scales of the

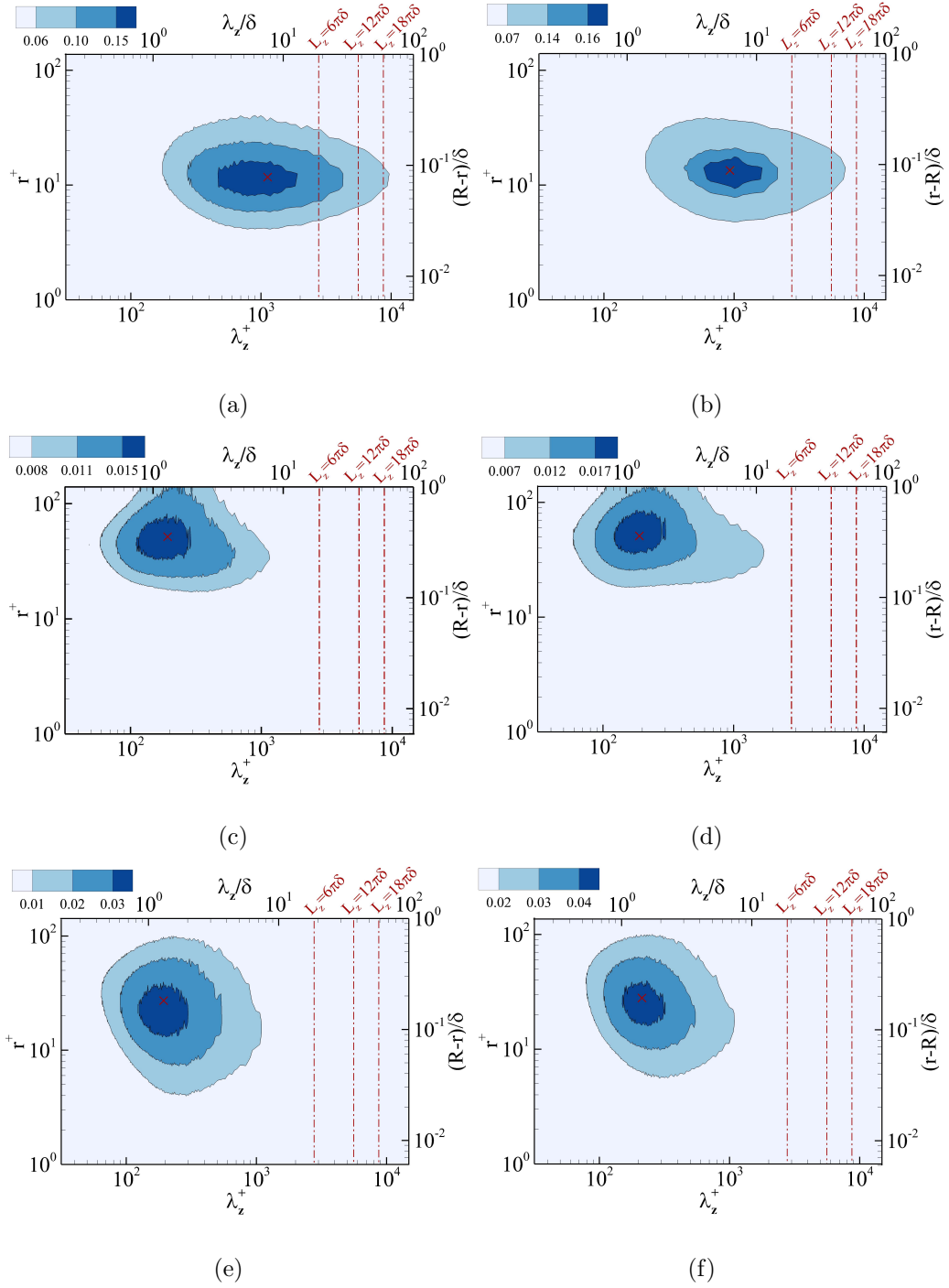


Figure 2.14: Contours of pre-multiplied 1D axial energy spectra of $k_z^+ \tilde{E}_{zz}^+(\lambda_z^+, r^+)$, $k_z^+ \tilde{E}_{rr}^+(\lambda_z^+, r^+)$, and $k_z^+ \tilde{E}_{\theta\theta}^+(\lambda_z^+, r^+)$ of case A6, non-dimensionalized by u_τ^2 . (a) $k_z^+ \tilde{E}_{zz}^+$ on the convex side, (b) $k_z^+ \tilde{E}_{zz}^+$ on the concave side, (c) $k_z^+ \tilde{E}_{rr}^+$ on the convex side, (d) $k_z^+ \tilde{E}_{rr}^+$ on the concave side, (e) $k_z^+ \tilde{E}_{\theta\theta}^+$ on the convex side, and (f) $k_z^+ \tilde{E}_{\theta\theta}^+$ on the concave side. The value of u_τ equals to either $u_{\tau i}$ or $u_{\tau o}$, depending on the convex or the concave cylinder side in consideration. In each figure panel, the wavelength is given both as λ_z^+ (bottom) and as λ_z/δ (top). Similarly, the radial coordinate is given both as r^+ (left) and as $(R-r)/\delta$ or $(r-R)/\delta$ (right, for convex or concave side, respectively). The cross symbol ‘ \times ’ pinpoints the location of the mode.

streaky structures as indicated by the axial modes of $k_z^+ \tilde{E}_{zz}^+$ and $k_\theta^+ k_z^+ \check{E}_{zz}$ (inferred from Figs. 2.11 and 2.14) are consistent, which are $\lambda_z^+ = 1100$ and 900 on the convex and concave sides of the concentric annular pipe, respectively. The radial position where the mode of $k_z^+ \tilde{E}_{zz}^+$ occurs is similar between the convex and concave sides of the concentric annular pipe, which is approximately at $r^+ = 15$. This implies that under the testing condition, the near-wall streaky structures are the most energetic at this radial position on both sides of the concentric annular pipe. The appearance of the peak value of $k_z^+ \tilde{E}_{zz}^+$ at radial position of approximately $r^+ = 15$ is consistent with that for $\langle u'_z u'_z \rangle^+$ in the physical space. However, it should be indicated here that the overlapping of these two modes of $k_z^+ \tilde{E}_{zz}^+$ and $\langle u'_z u'_z \rangle^+$ at $r^+ = 15$ is not strictly required in mathematics, because these two quantities are connected through an integral relationship, i.e. $\langle u'_z u'_z \rangle = \int \tilde{E}_{zz}(r, k_z) dk_z$. From Figs. 2.14(a) and 2.14(b), it is evident that the domain of case A6 (with $L_z = 30\pi\delta$ and $L_\theta = 2\pi$) is sufficiently large to fully capture the outermost isopleth that corresponds to $0.375 \max(k_z^+ \tilde{E}_{ii}^+)$. If the axial domain size drops to $L_z = 18\pi\delta$ (as in case A5), the outermost isopleth is still fully captured on the concave side of the pipe at all radial positions. As the axial domain size drops further to $L_z = 12\pi\delta$ (as in case A4), the outermost isopleth is well captured at all radial positions but is slightly missed around $r^+ = 15$. However, as is seen in Fig. 2.14(a), if the axial domain size continues to drop to $L_z = 6\pi\delta$ (as in case A3), even the intermediate isopleth corresponding to a higher TKE level of $0.625 \max(k_z^+ \tilde{E}_{ii}^+)$ cannot be fully captured, indicating a rather inaccurate DNS. From the previous analysis of turbulence statistics in the physical space conducted in section 2.2, we drew a conclusion that a minimum axial domain length of $L_z = 6\pi\delta$ of case A3 was satisfactory, which is apparently contradictory to the evidence shown in Fig. 2.14(a) and 2.14(b). The spectral analysis conducted here allows us to refine the study by accurately assessing the axial characteristic wavelengths of energetic near-wall streaky structures. Based on the combined physical and spectral analyses, it is now confirmed that the minimum axial computation domain must be stretched

to $L_z = 12\pi\delta$, in order to perform DNS accurately for the turbulent concentric annular pipe flow investigated here.

By comparing Figs. 2.14(c)-2.14(f), it is apparent that all three isopleths (corresponding to $0.875 \max(k_z^+ \tilde{E}_{ii}^+)$, $0.625 \max(k_z^+ \tilde{E}_{ii}^+)$ and $0.375 \max(k_z^+ \tilde{E}_{ii}^+)$) are fully captured by axial premultiplied 1D spectra of radial and azimuthal velocity fluctuations, $k_z^+ \tilde{E}_{rr}^+$ and $k_z^+ \tilde{E}_{\theta\theta}^+$, respectively. It should be indicated that in Figs. 2.14(c) and 2.14(d), the outermost isopleth is not fully captured at the maximum radial position around $r^+ = 150$. This is not an indication of insufficient radial domain size, but instead a reflection of the radial domain center, as only one-half of the radial domain is plotted in Figs. 2.14(c) and 2.14(d). From Figs. 2.14(c)-2.14(f), it is observed that the energy levels of $k_z^+ \tilde{E}_{rr}^+$ and $k_z^+ \tilde{E}_{\theta\theta}^+$ (as indicated by the color-scale legend) are one order of magnitude smaller than that of $k_z^+ \tilde{E}_{zz}^+$. The modes of $k_z^+ \tilde{E}_{rr}^+$ and $k_z^+ \tilde{E}_{\theta\theta}^+$ occur at $(r^+, \lambda_z^+) = (50, 200)$ and $(30, 200)$ on both sides of the concentric pipe, respectively. Clearly, the axial characteristic wavelengths of the turbulence structures as indicated by the modes of $k_z^+ \tilde{E}_{rr}^+$ and $k_z^+ \tilde{E}_{\theta\theta}^+$ are much smaller than that of $k_z^+ \tilde{E}_{zz}^+$ (which is about 1000 wall units, see above). Furthermore, it is interesting to observe that the modes of $k_z^+ \tilde{E}_{zz}^+$, $k_z^+ \tilde{E}_{rr}^+$ and $k_z^+ \tilde{E}_{\theta\theta}^+$ appear at three different radial positions for $r^+ = 15, 30$ and 50 , respectively. The physical mechanisms underlying these observations relate to the features of hairpin structures shown in Fig. 2.13. Similar to the hairpin structures of a turbulent boundary layer developed over a flat plate (Adrian Adrian (2007)), the radially oriented parts of a hairpin structure that connects the legs to the head (referred to as the “neck” by Adrian Adrian (2007)) contribute the most to the peak value of $k_z^+ \tilde{E}_{rr}^+$ (associated with the radial Reynolds normal stress component $\langle u'_r u'_r \rangle^+$). The necks of hairpin structures (for both PHV and SHV) are the most energetic around $r^+ = 50$, characterized by wavelength of approximately $\lambda_z^+ = 200$. Because the characteristic wavelength of either PHV or SHV (see Fig. 2.13) is approximately 400 wall units, the axial separation of the hairpin necks is typically around 200 wall units at this particular radial position judging

from the mode of $k_z^+ \tilde{E}_{rr}^+$. The reason that the peak of $k_z^+ \tilde{E}_{\theta\theta}^+$ appears at $r^+ = 30$ is that there exist azimuthally-oriented vortex filaments, which connect hairpin legs and are the most energetic around this elevation. These azimuthally-oriented vortex filaments lay further away from the wall than the near-wall streaks, perturbed and pushed away by ejections to form hairpin arches at higher elevations. Consistent with the analysis of the hairpin necks, the characteristic wavelength that represents the axial separation of azimuthally-oriented vortex filaments is also 200 wall units.

From the above analysis of the premultiplied 1D energy spectrum $k_z^+ \tilde{E}_{zz}^+$ in Figs. 2.14(a) and 2.14(b), it is understood that the axially-elongated streaks are the most energetic and the longest at $r^+ \approx 15$ on both convex and concave sides. Correspondingly, the magnitude of Reynolds normal stress $\langle u'_z u'_z \rangle^+$ also peaks at this radial position on both sides of the concentric annular pipe. The contours of $k_z^+ \tilde{E}_{zz}^+$ shown in Fig. 2.14 are based on case A6 only, which has the largest computational domain and allows for the most accurate prediction of turbulence statistics. However, in order to understand the direct influence of the axial domain size on the predictive accuracy of $k_z^+ \tilde{E}_{zz}^+$, test cases of different axial domain sizes must be compared based on independent numerical simulations. To this purpose, the profiles of all six A-series test cases are compared in Fig. 2.15. To demonstrate the Reynolds number effect, the profiles of the six A-series test cases are also compared against that of case D. The black dashed lines demarcate the axial computational domain sizes as well as the cutoff wavelengths of the A-series test cases, which vary from $L_z = 6\pi\delta$ to $30\pi\delta$ in cases A3 to A6. Similarly, the red dashed line demarcates the axial computational domain size and cutoff wavelength of case D.

From Fig. 2.15, it is clear that cases A1 and A2 fail to capture the mode of $k_z^+ \tilde{E}_{zz}^+$, implying that the most energetic eddy motions are missed in DNS. This well explains the failure of cases A1 and A2 in terms of the prediction of $\langle u'_z u'_z \rangle^+$ in Fig. 2.4a. As is clear from Fig. 2.15, although the mode of the premultiplied 1D energy spectrum has been successfully captured in cases A3-A6, the spectrum cutoffs for these four test

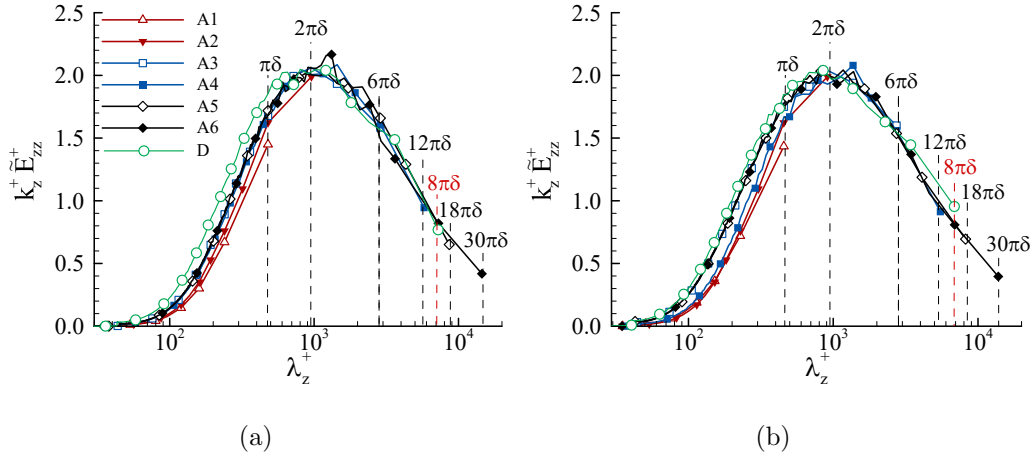


Figure 2.15: Profiles of non-dimensionalized premultiplied 1D axial energy spectra $k_z^+ \tilde{E}_{zz}^+$ of the A- and D-series test cases at the cylindrical surface located at $r^+ = 15$ from the convex and concave walls. (a) convex side, and (b) concave side. Vertical dashed lines demarcate the axial computational sizes (i.e., L_z values) for cases A1-A6 and D.

cases are different due to the differences in their axial domain sizes. At their cutoff wavelength, the magnitude of the premultiplied 1D energy spectrum is 79%, 45%, 32% and 21% of its peak value on the convex side and is 79%, 44%, 34% and 18% of its peak value on the concave side in cases A3, A4, A5 and A6, respectively. Given the fact that the cutoff wavelength occurs at a very high TKE level, the amount of TKE associated with wavelengths that are larger than the cutoff wavelength missed by DNS is significant in case A3. For this reason, even though the axial domain length of case A3 ($L_z = 6\pi\delta$) was satisfactory in previous predictions of the mean velocity, Reynolds stresses and two-point correlation coefficient, it is insufficient with respect to the current spectral analysis. Based on our previous analysis of Fig. 2.14, it is understood that an axial domain size of $L_z = 12\pi\delta$ is satisfactory in general with respect to capturing TKE at all radial positions for test cases of lower nominal Reynolds number of $Re_{D_h} = 8900$. From Fig. 2.15, it is further confirmed that even at $r^+ = 15$ where the near-wall streaks are the most energetic and the longest, the cutoff wavelength occurs when the premultiplied 1D spectrum decays to 45% of its

peak value, implying that most of the energy-containing length scales are resolved in DNS.

Also from Fig. 2.15, it is seen that as the nominal Reynolds number increases from $Re_{D_h} = 8900$ to 17700, the cutoff wavelength of case D takes place when the premultiplied 1D spectrum decays to 39% and 47% of its peak value on the convex and concave cylinder sides, respectively. By comparing case D with case A4, it is clear that although the level of the premultiplied 1D spectrum at the cutoff wavelength is comparable between cases D and A4, the axial domain length of case D is only $L_z = 8\pi\delta$, which is much shorter than that ($12\pi\delta$) of case A4. This implies that a shorter axial domain is needed for conducting DNS at a higher Reynolds number. This phenomenon is interesting but not surprising, which is similar to that of the classical turbulent plane channel flows Jiménez and Moin (1991); Kim et al. (1987); Moser and Moin (1987) and can be explained as follows. From the above analysis of Figs. 2.14 and 2.15, it is understood that the mode of either the 2D or 1D premultiplied spectrum of axial velocity fluctuations occurs approximately at a wavelength of $\lambda_z^+ = u_\tau \lambda_z / \nu \approx 1000$ at both nominal Reynolds numbers, which corresponds to the characteristic axial length scale of the most energetic streaky structures. Considering that the value of wall friction velocity u_τ increases as the Reynolds number increases (see Table 2.2), then the characteristic wavelength λ_z (corresponding to the mode) must decrease in order to maintain the value of the non-dimensional wavelength λ_z^+ at approximately 1000 wall units. As such, the physical axial length of concentric annular pipe required for capturing the most energetic streaky structures can be shortened as the Reynolds number increases.

For the lower nominal Reynolds number tested ($Re_{D_h} = 8900$), although the axial computational domain size of case A6 is the largest, eddies of axial length scales that are larger than the cutoff wavelengths (where the value of $k_z^+ \tilde{E}_{zz}^+$ decays to 21% and 18% of its peak value on the convex and concave sides, respectively) are still missed in the DNS. In fact, it is unrealistic to fully capture the premultiplied energy spectrum

(with 0% of spectrum leaking) in a DNS or in a physical experiment, as it demands using a pipe of infinite length. Thus far, the longest axial domain size used for DNS of concentric annular pipe flow in the literature is $L_z = 6\pi\delta$ by Chung *et al.* Chung *et al.* (2002) for a similar nominal Reynolds number of $Re_{D_h} = 8900$. As such, the minimum axial domain size of $L_z = 12\pi\delta$ recommended here is twice that of Chung *et al.* Chung *et al.* (2002), which makes it the longest in the current literature.

2.3.3 Azimuthal premultiplied energy spectra

Similar to the 1D axial energy spectrum, the 1D azimuthal energy spectrum can be computed by integrating the 2D energy spectrum over the axial wavenumbers as

$$\tilde{E}_{ii}(k_\theta, r) = \int \check{E}_{ii}(k_z, k_\theta, r) dk_z \quad , \quad (2.12)$$

or in a discrete form, as $\tilde{E}_{ii}(k_\theta, r) = k_{z0} \sum_{k_z} \check{E}_{ii}(k_z, k_\theta, r)$ for $i = 1, 2$ or 3 (no summation convention implied). Different from the 1D axial energy spectrum, the 1D azimuthal energy spectrum is useful for analyzing the characteristic azimuthal length scales associated with the energetic eddy motions. Based on the conclusion of the previous subsection, it is understood that a minimum axial domain of $L_z = 12\pi\delta$ is needed in order to capture axially-elongated energetic eddy motions. In this subsection, we aim at investigating the minimum azimuthal domain size for DNS by analyzing the premultiplied 1D azimuthal energy spectrum $k_\theta^+ \tilde{E}_{ii}^+$ (as a function of r^+ and k_θ^+). To this purpose, case B5 (with $L_z = 12\pi\delta$ and $L_\theta = 2\pi$) is selected, which has a sufficient axial domain size and the largest azimuthal domain size to facilitate generation of the most reliable azimuthal spectral results. Figure 2.16 compares the premultiplied 1D azimuthal energy spectra of all three velocity fluctuation components on the convex and concave sides of cases B5. Dash-dotted lines demarcate the azimuthal computational domain sizes of cases B1-B5, which vary from $L_\theta = \pi/6$ to $L_\theta = 2\pi$. Similar to the previous subsection, the local friction velocity ($u_{\tau i}$ or $u_{\tau o}$) is used for non-dimensionalization on the convex or concave side. The cross symbol ‘ \times ’

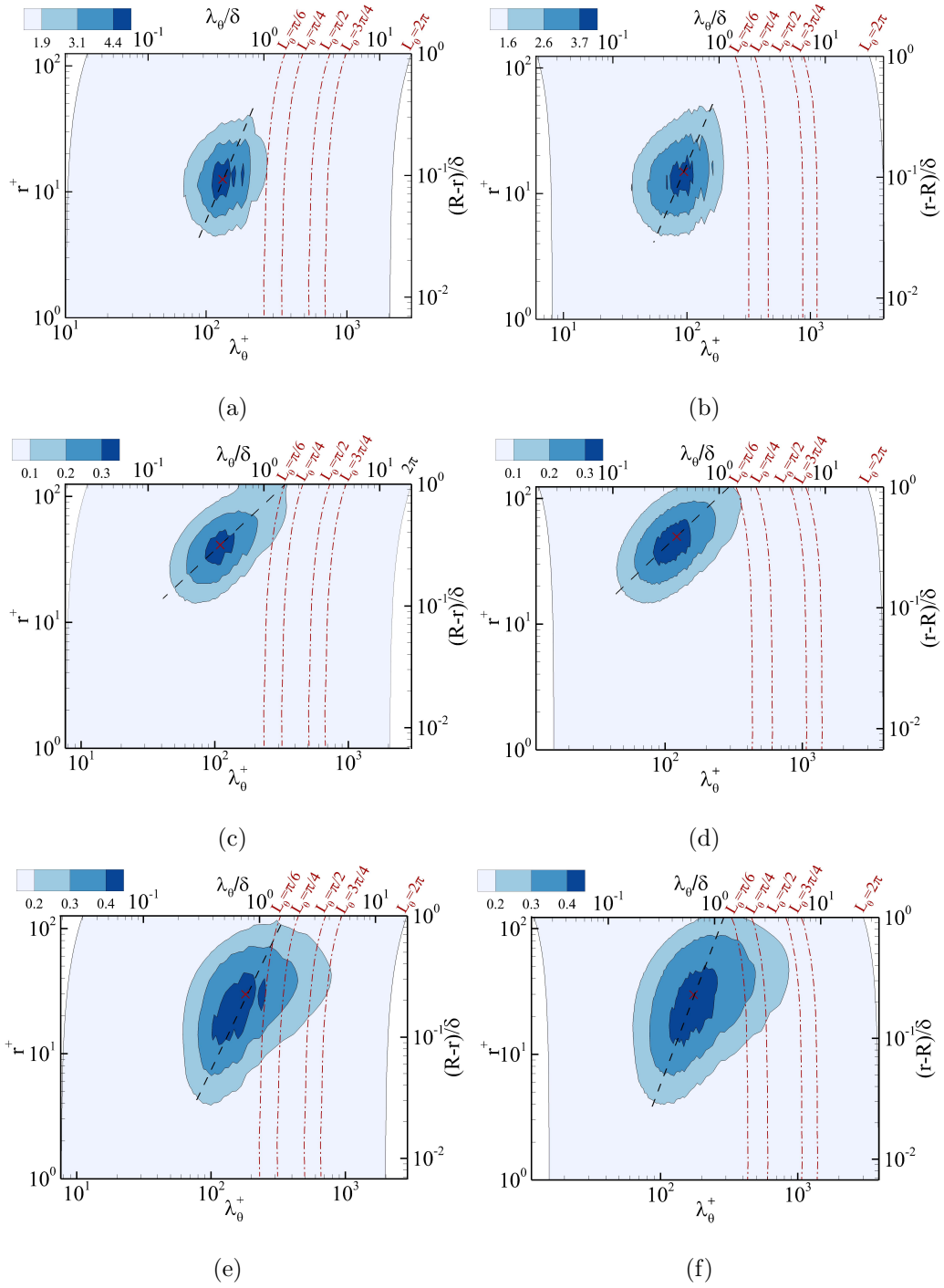


Figure 2.16: Contours of pre-multiplied 1D axial energy spectra of $k_\theta^+ \tilde{E}_{zz}^+(\lambda_\theta^+, r^+)$, $k_\theta^+ \tilde{E}_{rr}^+(\lambda_\theta^+, r^+)$, and $k_\theta^+ \tilde{E}_{\theta\theta}^+(\lambda_\theta^+, r^+)$ of case B5, non-dimensionalized by u_τ^2 . (a) $k_\theta^+ \tilde{E}_{zz}^+$ on the convex side, (b) $k_\theta^+ \tilde{E}_{zz}^+$ on the concave side, (c) $k_\theta^+ \tilde{E}_{rr}^+$ on the convex side, (d) $k_\theta^+ \tilde{E}_{rr}^+$ on the concave side, (e) $k_\theta^+ \tilde{E}_{\theta\theta}^+$ on the convex side, and (f) $k_\theta^+ \tilde{E}_{\theta\theta}^+$ on the concave side. The value of u_τ equals to either $u_{\tau i}$ or $u_{\tau o}$, depending on the convex or the concave cylinder side in consideration. In each figure panel, the wavelength is given both as λ_θ^+ (bottom) and as λ_θ/δ (top). Similarly, the radial coordinate is given both as r^+ (left) and as $(R-r)/\delta$ or $(r-R)/\delta$ (right, for convex or concave side, respectively). The cross symbol ‘x’ pinpoints the location of the mode.

pinpoints the mode corresponding to the maximum premultiplied energy spectrum, i.e. $\max(k_\theta^+ \tilde{E}_{ii}^+)$. Similar to the previous analysis, contours corresponding to the of high-, intermediate- and low-intensity cores are distinguished by three isopleth values of the premultiplied 1D azimuthal spectra of $0.875 \max(k_\theta^+ \tilde{E}_{ii}^+)$, $0.625 \max(k_\theta^+ \tilde{E}_{ii}^+)$ and $0.375 \max(k_\theta^+ \tilde{E}_{ii}^+)$, respectively. By comparing Figs. 2.16(a)-2.16(f), it is clear that Fig. 2.16(e) represents the most critical scenario in terms of the choice of the azimuthal domain size, which shows that a minimal domain of $L_\theta = 3\pi/4$ (corresponding to case B4) is needed in order to fully capture the outermost isopleth corresponding to $0.375 \max(k_\theta^+ \tilde{E}_{\theta\theta}^+)$.

Figures 2.16(a) and 2.16(b) compare the contour patterns of premultiplied 1D azimuthal spectrum of axial velocity fluctuations ($k_\theta^+ \tilde{E}_{zz}^+$) on the convex and concave sides. The mode of $k_\theta^+ \tilde{E}_{zz}^+$ occurs at $(r^+, \lambda_\theta^+) = (14.8, 120)$ and $(r^+, \lambda_\theta^+) = (15.3, 90)$ on the convex and concave sides, respectively. The small difference in the modal values of r^+ between the convex and concave sides is due to the surface curvature effect. Nonetheless, the appearance of the peak value of $k_\theta^+ \tilde{E}_{zz}^+$ at the radial position of approximately $r^+ = 15$ is consistent with the previous conclusion based on the analysis of the premultiplied 1D axial spectrum $k_z^+ \tilde{E}_{zz}^+$.

Figures 2.16(c) and 2.16(d) show contours of the premultiplied 1D azimuthal spectrum of radial velocity fluctuations $k_\theta^+ \tilde{E}_{rr}^+$ on the convex and concave cylinder sides, respectively. Clearly, the mode occurs at $(r^+, \lambda_\theta^+) \approx (50, 100)$ on both cylinder sides of the concentric annular pipe. This mode of $k_\theta^+ \tilde{E}_{rr}^+$ indicates that the radially oriented parts of hairpin structures (i.e., hairpin necks) are the most energetic at the radial position of $r^+ \approx 15$ and the azimuthal spacing is approximately 100 wall units. Figures 2.16(e) and 2.16(f) show the contours of the premultiplied 1D azimuthal spectrum of azimuthal velocity fluctuations $k_\theta^+ \tilde{E}_{\theta\theta}^+$. From Figs. 2.16(e) and 2.16(f), it is seen that the mode of $k_\theta^+ \tilde{E}_{\theta\theta}^+$ occurs at $(r^+, \lambda_\theta^+) \approx (30, 150)$ on both convex and concave sides of the concentric annular pipe. The physical mechanism underlying this mode is that the characteristic azimuthal length of the vortex filaments that con-

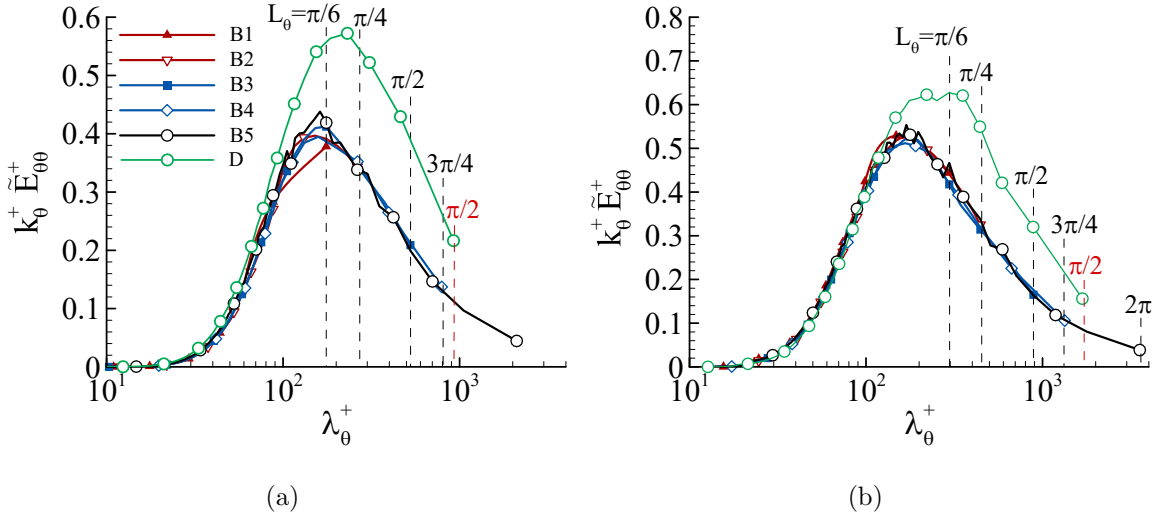


Figure 2.17: Profiles of non-dimensionalized premultiplied 1D azimuthal energy spectra $k_{\theta}^+ \tilde{E}_{\theta\theta}^+$ of the B- and D-series test cases at the cylindrical surface located at $r^+ = 30$ from the convex and concave walls. (a) convex side, and (b) concave side. Vertical dashed lines demarcate the azimuthal computational sizes (i.e., L_{θ} values) for cases B1-B5 and D.

nect the legs of the hairpin structures (i.e., hairpin arches) are the most energetic at $r^+ \approx 30$, with an characteristic azimuthal wavelength of $\lambda_{\theta}^+ = 150$. It should be further indicated here that although the hairpin necks are the most energetic at $r^+ \approx 50$, this does not imply that the hairpin arches are necessarily the most energetic at higher elevations for $r^+ > 50$. This is because the structures and dynamics of hairpin packets are always more complicated in reality than the ideal situation that all hairpin structures are uniformly sized and each hairpin structure has a perfect symmetrical shape of two legs, two necks and one arch.

In Fig. 2.16(a)-2.16(e), the contours of all three components of $k_{\theta}^+ \tilde{E}_{ii}^+$ show quasi-elliptical shapes, with an inclined major axis. This inclined major axis shows a linear scale growth rate with the wall-normal distance, which indicates that the azimuthal scales of near-wall streaks (Figs. 2.16(a) and 2.16(b)) and hairpin structures (Figs. 2.16(c)-2.16(f)) increase as the wall-normal distance increases. This observation is consistent with the DNS results of turbulent pipe flows of Wu *et al.* Wu et al.

(2012) and hot-wire measurements of turbulent channel and pipe flows of Monty *et al.* Monty et al. (2007).

From the above analysis of Fig. 2.16, it is understood that the value of $k_\theta^+ \tilde{E}_{\theta\theta}^+$ is more sensitive to the choice of the azimuthal domain size than the other two components of the premultiplied 1D azimuthal spectra. Furthermore, it is understood that the analysis of Fig. 2.16 is conducted based on the DNS result of case B5 only, which has the largest azimuthal domain size of $L_\theta = 2\pi$ and offers the most accurate DNS results among the B-series test cases. However, in order to examine the actual influence of the azimuthal domain size on the predictive accuracy of DNS, numerical simulations based on all five B-series test cases need to be carried independently. To this purpose, Fig. 2.17 compares the non-dimensionalized premultiplied 1D azimuthal spectra $k_\theta^+ \tilde{E}_{\theta\theta}^+$ of all five B-series test cases at a fixed radial position $r^+ = 30$. The reason that Fig. 2.17 is plotted for $r^+ = 30$ is that $k_\theta^+ \tilde{E}_{\theta\theta}^+$ peaks approximately at this radial position based on the DNS result of case B5 shown in Figs. 2.16(e) and 2.16(f). In Fig. 2.17, the black dashed lines demarcate the azimuthal computational domain sizes as well as the cutoff wavelengths of the B-series test cases, which vary from $L_\theta = \pi/6$ to 2π in cases B1 to B5. The results shown in Fig. 2.17 provide a direct measure on the accuracy of the assumed periodical azimuthal boundary condition used in DNS at the lower nominal Reynolds number of $Re_{D_h} = 8900$. To investigate the Reynolds number effects, the profiles of these five B-series test cases are also compared against that of case D. Clearly, the turbulence energy level as indicated by the premultiplied spectrum of the azimuthal velocity fluctuations ($k_\theta^+ \tilde{E}_{\theta\theta}^+$) increases as the Reynolds number increases. This pattern of $k_\theta^+ \tilde{E}_{\theta\theta}^+$ as a result of an increasing Reynolds number in the spectral space is consistent with that of $\langle u'_\theta u'_\theta \rangle^+$ in the physical space shown in Fig. 2.5b. Furthermore, the characteristic azimuthal length scale (or, the spanwise separation) of the energetic streaky structures corresponding to the modal value of $k_\theta^+ \tilde{E}_{\theta\theta}^+$ also increases as the Reynolds number increases on both convex and concave cylinder sides of the concentric annular pipe.

From Fig. 2.17(a), case B1 barely captures the mode of $k_\theta^+ \tilde{E}_{\theta\theta}^+$ on the convex side. This well explains that the underprediction of $\langle u'_\theta u'_\theta \rangle^+$ on the convex side in Fig. 2.5b. By contrast, the mode of the premultiplied 1D azimuthal spectrum $k_\theta^+ \tilde{E}_{\theta\theta}^+$ is captured in cases B2-B5. However, the cutoff wavelengths of $k_\theta^+ \tilde{E}_{\theta\theta}^+$ differ. Specifically, at the cutoff wavelength, the magnitude of $k_\theta^+ \tilde{E}_{\theta\theta}^+$ is 87.6%, 52.7%, 33.6% and 11.2% of its peak value on the convex side, and 84.6%, 62.7%, 20.1% and 7.0% of its peak value on the concave side, in cases B2, B3, B4 and B5, respectively. In other words, based on the comparative study of $k_\theta^+ \tilde{E}_{\theta\theta}^+$ at $r^+ = 30$ for the B-series test cases, the computational domain size of $L_\theta = 3\pi/4$ of case B4 resolves most of the energy-containing scales. Only a small portion of large scales remain unresolved which contain energy that is lower than 33.6% and 20.1% of the peak value of $k_\theta^+ \tilde{E}_{\theta\theta}^+$ at the cutoff wavelength on the convex and concave sides of the concentric annular pipe, respectively. Furthermore, from Fig. 2.17, it is seen that as the nominal Reynolds number increases from $Re_{D_h} = 8900$ to 17700, the cutoff wavelength of case D takes place when the value of $k_\theta^+ \tilde{E}_{\theta\theta}^+$ decays to 39% and 24% of its peak value on the convex and concave cylinder sides, respectively. This further indicates the domain size of case D is suitable for capturing the characteristic azimuthal length scale of the energetic large-scale streaky structures at the higher nominal Reynolds number of $Re_{D_h} = 17700$. Finally, it is very interesting to observe that in case B5, the value of $k_\theta^+ \tilde{E}_{\theta\theta}^+$ decays to 11.2% and 7.0% of its peak value on the convex and concave sides of the concentric annular pipe, respectively. Considering that the azimuthal domain size of case B5 is a full circle with $L_\theta = 2\pi$, there is only one explanation that there are some low-energy flow structures in the flow, which have azimuthal periods larger than 2π . An example of this type of continuously developing azimuthal structure is the familiar helical structure.

Chapter 3

The Effects of Radius Ratio on Turbulent Concentric Annular Pipe Flow and Structures

In a concentric annular pipe flow, the radius ratio not only alters the transverse curvature of the inner and outer cylinder walls, but also drastically affects the characteristics of turbulent boundary layers developed along the inner and outer cylinder surfaces. Closely related to this subject, in the current literature, there are studies of flows over a single concave or convex curved surface. For instance, So and Mellor (1973) conducted an experiment in a wind tunnel of curved surfaces to study curvature effects on the turbulent flow field. They reported that turbulence intensities are higher on the concave wall than on the convex wall. Neves et al. (1994) conducted DNS to study the effects of transverse curvature on the turbulent boundary layer developed over a convex surface. They showed that as the transverse curvature increases, the slope of the mean axial velocity in the logarithmic region and the turbulent intensities reduce. They also showed that turbulence structures remain unaffected unless the ratio of the boundary layer thickness to the radius of transversely curved surface is large.

As reviewed in chapter 1, although there are a couple of experimental and numerical studies of the concentric annular pipe flow of different radius ratios (Nouri et al., 1993; Chung et al., 2002), the number of detailed DNS studies of the effects of radius ratio on the turbulent flow in a concentric annular pipe is still rather limited in the current literature. In view of this, we aim at conducting a systematic DNS study of turbulent concentric annular pipe flow based on various radius ratios ($R_i/R_o = 0.1-0.7$). Specifically, we will examine the effects of radius ratio on the first- and second-order statistical moments of the velocity field, interaction of the boundary layers developed over the inner and outer cylinder walls, spectra of the velocity and vorticity fields, budget balance of Reynolds shear stress, and the length scales of the streamwise vortical structures near the inner and outer cylinder walls. The content and results of following chapter is published in Bagheri et al. (2020).

The organization of the present study is as follows: in section 3.1, the test cases are described and the sufficiency of the selected computational domains is discussed. In section 3.2, DNS results of various radius ratio cases are compared and analyzed. Finally, in section 3.3, the effects of radius ratio on the scales and strengths of streamwise vortical structures and hairpin structures are investigated.

3.1 Test cases and numerical algorithm

Figure 3.1 shows the schematic diagram of concentric annular pipe flow with respect to the cylindrical coordinate system. In this figure, z , θ and r , denote the axial (streamwise), azimuthal and radial coordinates, respectively, and u_z , u_θ and u_r represent velocity components in the corresponding directions. The radius of the cylindrical channel center is $R = (R_i + R_o)/2$. The equations that govern an incompressible flow with respect to a cylindrical coordinate system read

$$\nabla \cdot \vec{u} = 0 \quad , \quad (3.1)$$

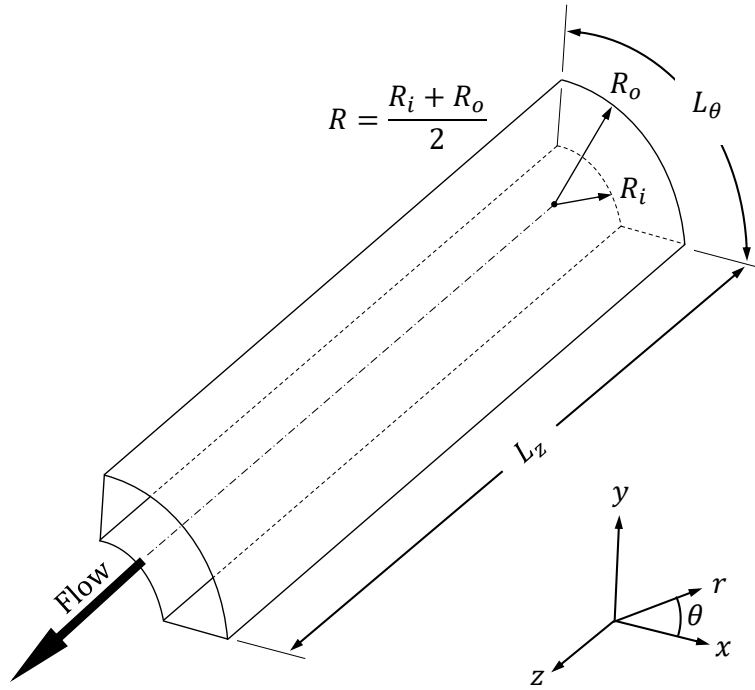


Figure 3.1: Computational domain and coordinates.

$$\frac{\partial \vec{u}}{\partial t} + \vec{u} \cdot \nabla \vec{u} = -\frac{1}{\rho} \nabla p + \nu \nabla^2 \vec{u} - \frac{\Pi}{\rho} \hat{\mathbf{e}}_z \quad , \quad (3.2)$$

where p , ρ and ν denote the pressure, density and kinematic viscosity, respectively. Π is the constant mean axial pressure gradient that drives the flow, and $\hat{\mathbf{e}}_z$ is the base unit vector of the z -direction, with $|\hat{\mathbf{e}}_z| \equiv 1$. The details of numerical algorithm to solve the governing equations of the problem are presented in appendix A.

A summary of test cases and grid resolutions are given in table 3.1. Four radius ratios (for $R_i/R_o = 0.1, 0.3, 0.5$ and 0.7) are compared at a nominal Reynolds number of $Re_{D_h} = 8900$. The axial domain size is fixed at $L_z = 12\pi\delta$ for all cases, where $\delta = (R_o - R_i)/2$ denotes one half the cylinder gap. However, the azimuthal domain size varies from $L_\theta = 2\pi$ (in the case of $R_i/R_o = 0.1$) to $L_\theta = \pi/2$ (in the case of $R_i/R_o = 0.7$). Later in Section 3.2.1, a brief analysis will be conducted in the physical and spectral spaces to justify the choice of these computational domain sizes

for conducting the current DNS and research. The spatial grid resolution is uniform in both axial and azimuthal directions. In the wall-normal direction, Chebyshev-Gauss-Lobatto points were used to improve the spatial resolution near the wall. In Table 3.1, the wall units of the inner and outer sides are calculated based on the local wall friction velocities defined as $u_{\tau_i} = \sqrt{\tau_{wi}/\rho}$ and $u_{\tau_o} = \sqrt{\tau_{wo}/\rho}$, respectively. Here, the mean wall shear stresses on the inner and outer cylinder sides are defined as $\tau_{wi} = \rho\nu(d\langle u_z \rangle/dr)_{r=R_i}$ and $\tau_{wo} = -\rho\nu(d\langle u_z \rangle/dr)_{r=R_o}$, respectively. The mean wall friction velocity u_τ can be defined based on the weighted averaging over the inner and outer cylinder walls, i.e. $u_\tau = (R_o u_{\tau_o} + R_i u_{\tau_i})/(R_i + R_o)$. The origin for the radial coordinate r is located at the pipe center. In order to conduct near-wall analysis (as in a turbulent plane channel), a wall coordinate r^+ is also introduced, which is defined as $r^+ = (r - R_i)u_{\tau_i}/\nu$ and $r^+ = (R_o - r)u_{\tau_o}/\nu$ on the inner and outer cylinder sides, respectively. In order to maintain the accuracy required by DNS, the grid resolution is kept at $\Delta z_i^+ \leq 14.95$ and $(R_i \Delta \theta)^+ \leq 6.39$ on the inner cylinder side, and $\Delta z_o^+ \leq 14.49$ and $(R_o \Delta \theta)^+ \leq 8.46$ on the outer cylinder side. The radial resolution for the first node off the wall is kept for $\Delta r_{min,i}^+ \leq 0.22$ and $\Delta r_{min,o}^+ \leq 0.18$ on the inner and outer cylinder sides, respectively. More importantly, the maximum radial grid resolution is kept for $\Delta r_{max,i}^+ \leq 9.07$ and $\Delta r_{max,o}^+ \leq 7.41$ on the inner and outer sides, respectively. Here, superscript “+” denotes a quantity expressed in the wall coordinate (through non-dimensionalization based on ν and u_τ).

In this chapter, an arbitrary instantaneous flow variable ϕ is decomposed as $\phi = \langle \phi \rangle + \phi'$, where a pair of angular brackets $\langle \cdot \rangle$ represent temporal-averaging and spatial-averaging over a homogeneous (z - θ) cylindrical surface. For each simulation, statistics were collected at each time step for a reasonably long time duration of 35 large-eddy turnover times (LETOTs), where an LETOT is determined as δ/u_τ . The spectral accuracy was also enforced during post-processing of DNS data in order to maintain a high precision of the statistical results. The time step was kept at $0.001\delta/U_b$ such that the Courant-Friedrichs-Lewy (CFL) number is less than 0.8. All computations

Table 3.1: Summary of four test cases of different radius ratios and grid resolutions associated with each case. Here, $\delta = (R_o - R_i)/2$ is one half the cylinder gap.

R_i/R_o	0.1	0.3	0.5	0.7
$L_z \times L_\theta \times L_r$	$12\pi\delta \times 2\pi \times 2\delta$	$12\pi\delta \times 3\pi/2 \times 2\delta$	$12\pi\delta \times 3\pi/4 \times 2\delta$	$12\pi\delta \times \pi/2 \times 2\delta$
$N_z \times N_\theta \times N_r$	$480 \times 256 \times 64$	$420 \times 260 \times 64$	$384 \times 196 \times 64$	$384 \times 210 \times 64$
Δz_i^+	14.20	14.26	14.95	14.82
Δz_o^+	11.39	13.10	14.18	14.49
$\Delta r_{min,i}^+$	0.22	0.19	0.19	0.18
$\Delta r_{min,o}^+$	0.18	0.18	0.18	0.18
$\Delta r_{max,i}^+$	9.07	7.97	7.64	7.57
$\Delta r_{max,o}^+$	7.28	7.32	7.25	7.41
$(R_i\Delta\theta)^+$	0.98	2.45	3.74	6.39
$(R_o\Delta\theta)^+$	7.90	7.54	7.09	8.46

were performed on the WestGrid (Western Canada Research Grid) supercomputers. Required CPU hours to conduct a DNS varies depending on the number of grid points. Test cases $R_i/R_o = 0.1$ and 0.7 are the most and the least expensive test cases, which were performed using 6,580 and 5,266 CPU hours, respectively.

3.2 Results and discussions

3.2.1 Computational domain sizes

The accuracy of the predicted flow field depends on not only numerical algorithm, and temporal and spatial grid resolutions, but also the computational domain size. Although the pseudo-spectral method employed here is highly accurate, it by itself is insufficient to warrant a correct prediction of the principal flow physics associated with the most energetic eddy motions. If the computational domain is overly small, energetic eddies cannot be captured by DNS, which necessarily leads to an artificial distortion or chopping off of the energy spectra at low wavenumbers. The sufficiency of a computational domain size can be investigated in both physical and spectral spaces based on the criteria of two-point correlation and premultiplied energy spectra.

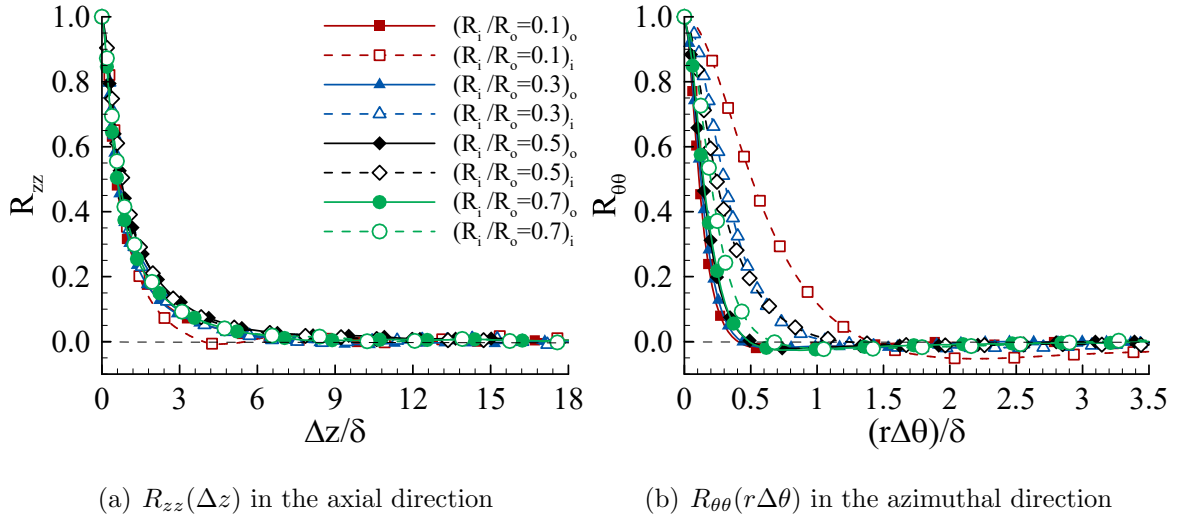


Figure 3.2: Profiles of 1D two-point correlation coefficients (R_{zz} and $R_{\theta\theta}$) for all test cases on the inner and outer cylinder sides. (a) The value of R_{zz} is calculated at $r^+ = 15$, where the Reynolds normal stress component $\langle u'_z u'_z \rangle$ peaks. (b) The value of $R_{\theta\theta}$ is calculated at $r^+ = 30$, where the Reynolds normal stress component $\langle u'_\theta u'_\theta \rangle$ peaks.

The effects of domain size on turbulent concentric annular pipe flow has been thoroughly investigated by Bagheri et al. (2020), who compared 12 test cases of different axial and azimuthal domain sizes for a fixed radius ratio of $R_i/R_o = 0.5$. They observed that the predictive accuracy of the first- and second-order statistical moments of the velocity field is dependent on the axial and azimuthal domain sizes. Through a systematic analysis of the velocity field in both physical and spectral spaces, they indicated that in order to correctly predict turbulence statistics of a concentric annular pipe flow, the axial and azimuthal computational domain sizes should be kept sufficiently large such that the most energetic eddy motions can be properly captured. In this subsection, we extend our study to include a wider range of radius ratios, and briefly justify the sufficiency of the selected domains required for accurately performing DNS for the four test cases of different radius ratios. A conventional tool for examining the adequacy of a computational size domain is the two-point correlation function. The axial and azimuthal one-dimensional (1D) two-

point correlation functions for the axial and azimuthal velocity fluctuations are defined as

$$R_{zz}(\Delta z) = \frac{\langle u'_z(z, r\theta, r, t)u'_z(z + \Delta z, r\theta, r, t) \rangle}{\langle u'_z(z, r\theta, r, t)u'_z(z, r\theta, r, t) \rangle} \quad (3.3)$$

and

$$R_{\theta\theta}(r\Delta\theta) = \frac{\langle u'_\theta(z, r\theta, r, t)u'_\theta(z, r\theta + r\Delta\theta, r, t) \rangle}{\langle u'_\theta(z, r\theta, r, t)u'_\theta(z, r\theta, r, t) \rangle} \quad (3.4)$$

respectively. Figure 3.2 compares the profiles R_{zz} and $R_{\theta\theta}$ of different test cases in the axial and azimuthal directions, respectively. The value of R_{zz} is calculated at $r^+ = 15$, where the Reynolds normal stress component $\langle u'_z u'_z \rangle$ reaches its peak value, while the value of $R_{\theta\theta}$ is calculated at $r^+ = 30$, where the Reynolds normal stress component $\langle u'_\theta u'_\theta \rangle$ peaks (to be shown later in section 3.2.2). Figures 3.2(a) and 3.2(b) show that the values of R_{zz} and $R_{\theta\theta}$ marginally go to zero for $\Delta z/\delta \geq 6$ and $(r\Delta\theta)/\delta \geq 1.5$, respectively, for all test cases. This indicates a sufficiency of the axial and azimuthal computational domain sizes (i.e., $L_z = 12\pi\delta$ and $L_\theta = \pi/2-2\pi$, see Table 3.1). It is worth mentioning that the choice of domain sizes based on two-point correlation coefficients in the physical space may not be conclusive, and it is necessary to further study the energy spectra of the flow field in the spectral space to ensure that all energetic eddies of low wavenumbers are fully captured. The two-dimensional (2D) energy spectrum of velocity fluctuations is defined as

$$\check{E}_{ij} = \overline{\widehat{u}'_i \widehat{u}'_j^* + \widehat{u}'_i^* \widehat{u}'_j} \quad (3.5)$$

Here, $\check{E}_{ij}(k_z, k_\theta, r)$ is a real function of the axial and azimuthal wavenumbers and radius, the overline denotes averaging over time, and subscripts i and j correspond to the fluctuating velocity components. In Eq. (3.5), the 1D axial energy spectrum can be directly computed by integration over azimuthal wavenumbers, as $\check{E}_{ij}(k_z, r) = k_{\theta 0} \sum_{k_\theta} \check{E}_{ij}(k_z, k_\theta, r)$. The 1D azimuthal energy spectrum can be defined in a similar way by integrating $\check{E}_{ij}(k_z, k_\theta, r)$ over k_z , as $\check{E}_{ij}(k_\theta, r) = k_{z 0} \sum_{k_z} \check{E}_{ij}(k_z, k_\theta, r)$. Here, k_z and k_θ denote the axial and azimuthal wavenumbers, respectively. These two wavenumbers are determined as $k_z = n_z k_{z 0}$ and $k_\theta = n_\theta k_{\theta 0}$ for $n_z \in [-N_z/2, N_z/2 - 1]$

and $n_\theta \in [-N_\theta/2, N_\theta/2 - 1]$, respectively. Here, $k_{z0} = 2\pi/L_z$ and $k_{\theta0} = 2\pi/(r \cdot L_\theta)$ are the lowest positive wavenumbers in the axial and azimuthal directions, determined directly by the domain sizes L_z and L_θ , respectively.

Figure 3.3 compares the contour patterns of the premultiplied 1D axial spectrum of axial velocity fluctuations ($k_z^+ \tilde{E}_{zz}^+(\lambda_z^+, r^+)$) and the azimuthal spectrum of azimuthal velocity fluctuations ($k_\theta^+ \tilde{E}_{\theta\theta}^+(\lambda_\theta^+, r^+)$) of the case of $R_i/R_o = 0.1$ on the inner and outer sides of the concentric annular pipe. The reason this test case is selected is that the curvature difference between the inner and outer cylinder walls is the most distinct among all the test cases, which facilitates our investigation of the curvature effect on the minimum computational domain size. Three levels of the premultiplied energy spectrum are identified, which represent the high-, intermediate- and low-intensity cores of a turbulence structure. Following the approach of Hoyas and Jiménez (2006) and Yang and Wang (2018), the contours for these three levels of the premultiplied spectrum are distinguished by colors and by black solid borderlines corresponding to $0.875 \max(\tilde{E}_{ii}^+)$, $0.625 \max(\tilde{E}_{ii}^+)$ and $0.375 \max(\tilde{E}_{ii}^+)$ (or, corresponding to 7/8-th, 5/8-th and 3/8-th of the modal value, respectively). The modes (indicated using a red cross symbol “ \times ” in the figures) of $k_z^+ \tilde{E}_{zz}^+$ and $k_\theta^+ \tilde{E}_{\theta\theta}^+$ occur at $r^+ \approx 15$ and $r^+ \approx 30$, respectively, on the both inner and outer sides. For DNS, it is critically important to capture the peaks (modes) of these premultiplied energy spectra, which correspond to characteristic length scales of the most energetic eddy motions. The mode typically occurs at a large wavelength (but not necessarily at the largest possible wavelength) of the premultiplied spectrum. The premultiplied spectra can be useful for identifying the characteristic length scales of the most energetic eddy motions in a logarithmic coordinate system because of the following identity: $\langle u_i' u_j' \rangle = \int_0^\infty \tilde{E}_{ij}(k_m, r) dk_m = \int_0^\infty k_m \tilde{E}_{ij}(k_m, r) d(\ln(k_m))$ (for $i, j, m = 1, 2, \text{ or } 3$). This method of spectral analysis turbulent structure length scales is precise, which has been well established and documented in the literature (Jiménez, 2012; Kim et al., 1987; Moser et al., 1999; Yang and Wang, 2018).

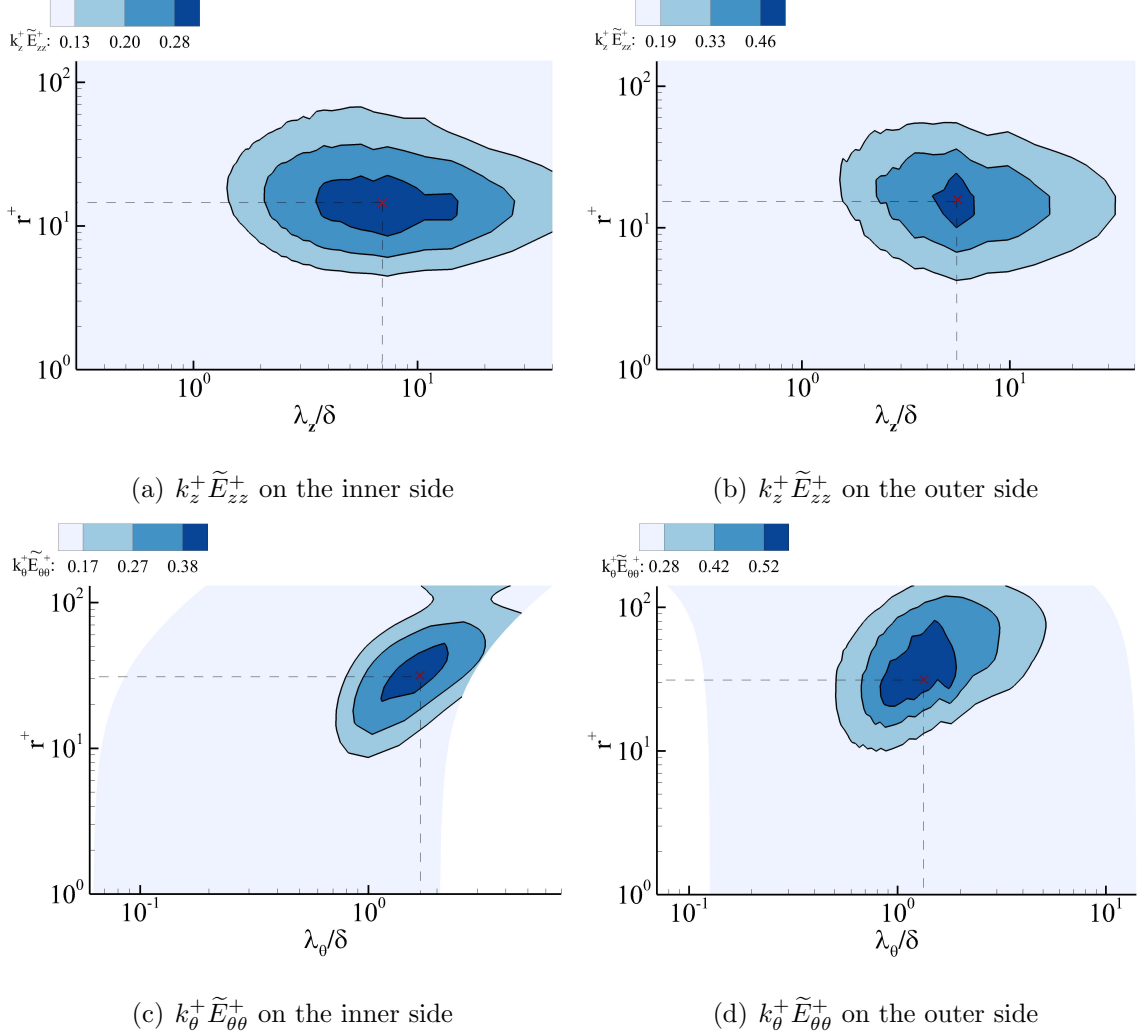


Figure 3.3: Contours of pre-multiplied 1D axial energy spectra of $k_z^+ \tilde{E}_{zz}^+(\lambda_z^+, r^+)$ and $k_\theta^+ \tilde{E}_{\theta\theta}^+(\lambda_z^+, r^+)$ of the case of $R_i/R_o = 0.1$. In the non-dimensionalization, the value of u_τ equals to either $u_{\tau i}$ or $u_{\tau o}$, depending on the convex (inner) or the concave (outer) cylinder side in consideration. The cross symbol ‘ \times ’ pinpoints the location of the mode. Three energy levels are distinguished, and the innermost, middle and outermost isopleths correspond to $0.875 \max(k_z^+ \tilde{E}_{ii}^+)$, $0.625 \max(k_z^+ \tilde{E}_{ii}^+)$ and $0.375 \max(k_z^+ \tilde{E}_{ii}^+)$, respectively. Besides these three isopleths which show three magnitude levels of the pre-multiplied spectrum relative to its peak value, the absolute magnitude of the non-dimensionalized pre-multiplied spectrum is also shown using a color legend.

From Figs. 3.3(a) and 3.3(b), it is evident that the axial domain of $L_z = 12\pi\delta$ is large enough to capture the outermost isopleth at all radial position except for a slight miss around $r^+ = 15$ on the inner side of the concentric annular pipe. Figures 3.3(c) and 3.3(d) show that all three levels of the azimuthal premultiplied energy spectrum $k_\theta^+ \tilde{E}_{\theta\theta}^+$ are also well captured in general on both inner and outer sides of the concentric annular pipe, except for the isopleth of the low-intensity core (for $0.375 \max(\tilde{E}_{ii}^+)$) on the inner side at large azimuthal wavelengths. This is due to the use of the periodic boundary condition in the azimuthal direction, which forces chopping off the premultiplied energy spectrum at a small finite level after a full azimuthal cycle of $L_\theta = 2\pi$, even though the azimuthal flow structures may develop spatially beyond a full cycle (exhibiting, e.g. a quasi-helical pattern) in physical reality. At the largest r^+ value (or, at top edge of the figure panel), the isopleth of $0.375 \max(\tilde{E}_{ii}^+)$ is seemingly incomplete in Figs. 3.3(c) and 3.3(d). But this is simply because the isopleths of $0.375 \max(\tilde{E}_{ii}^+)$ in these two figure panels are connected radially in the central domain of the concentric annular pipe. Owing to the difference in the local friction velocities ($u_{\tau i}$ and $u_{\tau o}$), the wall units measured from inner and outer sides of the concentric annular pipe are slightly different.

Figures 3.4(a) and 3.4(b) compare the profiles of 1D premultiplied spectra of axial velocity fluctuations (i.e., $k_z^+ \tilde{E}_{zz}^+(\lambda_z, r)$) and azimuthal velocity fluctuations (i.e., $k_\theta^+ \tilde{E}_{\theta\theta}^+(\lambda_\theta, r)$) of different test cases, respectively. Similar to the profiles of $R_{zz}(\Delta z)$ and $R_{\theta\theta}(r\Delta\theta)$ shown in Fig. 3.2, the values of $k_z^+ \tilde{E}_{zz}^+(\lambda_z, r)$ and $k_\theta^+ \tilde{E}_{\theta\theta}^+(\lambda_\theta, r)$ are also calculated at $r^+ = 15$ and $r^+ = 30$, respectively. Clearly, by comparing Figs. 3.2 and 3.4, it is understood that although the two-point correlation coefficient and the energy spectrum are counterparts of each other in Fourier transform, the criterion of two-point correlation coefficient is more intuitive but less informative compared to that of the energy spectrum. As is evident in Fig. 3.4, the premultiplied spectrum shows precisely the characteristic length scale (or the mode) corresponding to the most energetic eddy motions in the axial and azimuthal directions, the turbulence kinetic

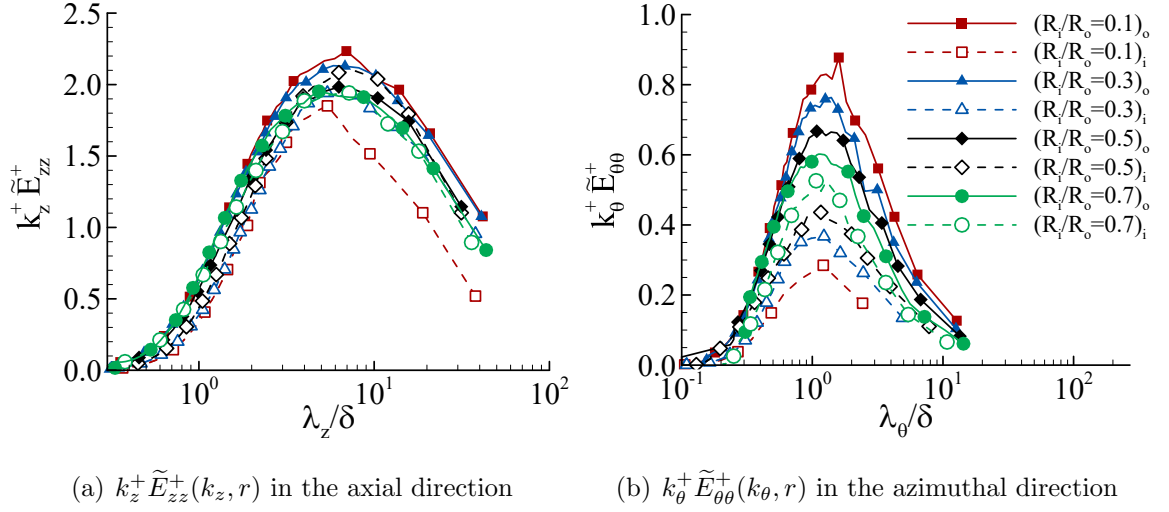


Figure 3.4: Profiles of premultiplied 1D spectra of axial velocity fluctuations (u'_z) $k_z^+ \tilde{E}_{zz}^+(k_z, r)$ and azimuthal velocity fluctuations (u'_θ) $k_\theta^+ \tilde{E}_{\theta\theta}^+(k_\theta, r)$ for all test cases on the inner and outer cylinder sides. (a) The value of $k_z^+ \tilde{E}_{zz}^+(k_z, r)$ is calculated at $r^+ = 15$, where the Reynolds normal stress component $\langle u'_z u'_z \rangle$ peaks. (b) The value of $k_\theta^+ \tilde{E}_{\theta\theta}^+(k_\theta, r)$ is calculated at $r^+ = 30$, where the Reynolds normal stress component $\langle u'_\theta u'_\theta \rangle$ peaks.

energy (TKE) level of large-scale structures captured at the cut-off wavelength, and the maximum axial and azimuthal wavelengths of large-scale flow structures that can be exactly contained and simulated using the selected domain.

From Fig. 3.4, it is evident that the TKE level as indicated by the premultiplied spectrum is higher on the outer cylinder side than on the inner cylinder side in general. The peak values of the premultiplied spectra $k_z^+ \tilde{E}_{zz}^+(\lambda_z, r)$ and $k_\theta^+ \tilde{E}_{\theta\theta}^+(\lambda_\theta, r)$ occur on the outer cylinder side at the lowest radius ratio tested (i.e, at $R_i/R_o = 0.1$). Clearly, the peak values of the premultiplied spectra have been well captured, indicating that the axial and azimuthal domain sizes (i.e, $L_z = 12\pi\delta$ and $L_\theta = 2\pi$) are sufficient for capturing the most energetic eddy motions in the case of $R_i/R_o = 0.1$. A perusal of Fig. 3.4 further indicates that in the case of $R_i/R_o = 0.1$, the value of $k_z^+ \tilde{E}_{zz}^+$ at the cut-off wavelength (corresponding to the lowest wavenumber) is 48% and 28% of its peak value on the inner and outer cylinder sides of the concentric annular pipe,

respectively; while the value of $k_\theta^+ \tilde{E}_{\theta\theta}^+$ at the cut-off wavelength is 56% and 18% of its peak value on the inner and outer cylinder sides of the concentric annular pipe, respectively.

Consistent with our previous analysis of Fig. 3.3, it is very interesting to observe in Fig. 3.4 that even though a full circle of $L_\theta = 2\pi$ (which is the largest possible azimuthal domain size) has been used for the case of $R_i/R_o = 0.1$, the value of pre-multiplied azimuthal spectrum $k_\theta^+ \tilde{E}_{\theta\theta}^+$ is non-trivial at the cut-off wavelength on both inner and cylinder sides, which decays to 56% and 18% of its peak value, respectively. Given the fact that the DNS is conducted here using a highly-accurate pseudo-spectral method code, the truncation error involved in the computation is the minimum. Therefore, there is only one possible physical explanation to this observed interesting phenomenon: there are some low-energy-level turbulent flow structures with azimuthal periods larger than 2π , possess a quasi-helical pattern, and can continue developing peripherally even after a full circle. As explained above, the flow field is homogeneous in the both of axial and azimuthal directions. In the axial direction, the energy spectrum is chopped off (at a relatively very low TKE level) due to the use of a finite-sized axial domain. Analogous to the axial direction, flow structures can be larger than 2π in the azimuthal direction in physical reality. But, owing to the use of the periodic boundary condition, the energy spectrum is artificially chopped off in the azimuthal direction after a full circle, such that the value of the energy spectrum is small (but non-zero) at the largest wavelength corresponding to $L_\theta = 2\pi$. The conventional periodic boundary condition is a good assumption for the statistical moments of the velocity field (because turbulence is statistically homogeneous in the azimuthal direction), but it is not necessarily a good assumption for large coherent flow structures, especially when they develop azimuthally with periods that are large than $L_\theta = 2\pi$.

Finally, it should be indicated that it is neither possible nor necessary to fully capture the pre-multiplied axial energy spectrum $k_z^+ \tilde{E}_{zz}^+$ (with 0% of spectrum leaking

Table 3.2: Mean flow parameters of all four test cases of different radius ratios.

R_i/R_o	δ_{ti}/δ	δ_{to}/δ	Re_{τ_i}	Re_{τ_o}	Re_{D_h}
0.1	0.62	1.38	111.39	200.72	8945
0.3	0.78	1.22	123.90	178.04	8953
0.5	0.88	1.12	133.82	161.98	8927
0.7	0.95	1.05	142.83	155.49	8936

at the cut-off wavelength) in the axial direction either in a DNS or in a physical experiment. There are two good reasons: firstly, this would demand the usage of a pipe of infinite length, which is impractical; and secondly, even if this is possible, the TKE level of the large-scale flow structures would be extremely low at the very high wavelengths, making it meaningless to desire so. To compare, the concentric annular pipe length considered here ($L_z = 12\pi\delta$) is actually twice that used in the DNS study of Chung et al. (2002) for a similar nominal Reynolds number of $Re_{D_h} = 8900$. The initial choice of the computational domains used in this research (see, Table 3.1) is based on the recent study of Bagheri et al. (2020), who systematically compared the axial and azimuthal domain sizes for accurately conducting DNS of turbulent flow confined within a concentric annular pipe at a fixed radius ratio of $R_i/R_o = 0.5$. Now, after rigorously justifying the computational domain sizes selected for conducting the current research, we can focus our attention on analyzing the effects of radius ratio on the flow statistics and structures in subsections to be followed.

3.2.2 Flow statistics

Fundamental to the understanding of flow physics, the characteristics and interaction of the boundary layers developed above the inner and outer cylinder surfaces need to be studied, which are sensitive to the radius ratio. Table 3.2 compares the mean flow parameters of four test cases of different radius ratios. In the table, $Re_{\tau_i} = \delta_{ti}u_{\tau_i}/\nu$ and $Re_{\tau_o} = \delta_{to}u_{\tau_o}/\nu$ are defined based on local wall friction velocity (u_{τ_i} or u_{τ_o}) and boundary layer thickness over the inner (δ_{ti}) or outer (δ_{to}) cylindrical

cal wall, respectively. In an axially fully-developed concentric annular pipe flow, the boundary layer thickness, δ_t , is defined as the distance from the wall to the point where the axial mean velocity reaches its maximum (or alternatively, where the Reynolds shear stress is zero). The interaction between the two boundary layers developed over the inner and outer cylinder walls will be discussed later in section 3.2.3. In order to maintain the nominal Reynolds number of $Re_{D_h} = 8900$, a constant mean streamwise pressure gradient is applied to the momentum equation that governs the streamwise flow, which is determined as $\Pi = -C_f \rho U_b^2 / (R_o - R_i)$. Here, C_f denotes the average friction coefficient, defined as $C_f = (C_{fi} R_i + C_{fo} R_o) / (R_i + R_o)$, where the skin friction coefficients of the inner and outer cylinder walls are defined as $C_{fi} = \tau_{wi} / (\rho U_b^2 / 2)$ and $C_{fo} = \tau_{wo} / (\rho U_b^2 / 2)$, respectively. The value of C_f can be determined from an empirical equation given by Nouri et al. (1993), i.e. $C_f = 0.36 Re_{D_h}^{-0.39}$. In order to ensure the value of Re_{D_h} calculated from DNS converges to its nominal value within a reasonable range of error tolerance, minor adjustments were made for the value of Π after initial test runs. The actual value of Re_{D_h} from the calculation is given in Table 3.2, which deviates slightly (up to 0.6%) from the nominal value of 8900. From Table 3.2, it is apparent that the boundary layer thicknesses and Reynolds numbers are smaller on the inner cylinder side than on the outer cylinder side (i.e., $\delta_{ti} < \delta_{to}$ and $Re_{\tau_i} < Re_{\tau_o}$) in all four test cases. This is a clear reflection of the curvature difference between the two cylinder walls. Furthermore, as the radius ratio R_i/R_o increases in value, the curvature difference between the two cylinder surfaces reduces, and as a result, the difference between the values of δ_{ti} and δ_{to} and that between Re_{τ_i} and Re_{τ_o} decrease monotonically.

Figure 3.5 compares the boundary layer thicknesses (δ_{ti} and δ_{to}) and the skin friction coefficients (C_{fi} and C_{fo}) of the inner and outer cylinder sides as a function of the radius ratio. From Fig. 3.5(a), it is clear that the value of C_{fi} decreases significantly while that of C_{fo} increases slightly as the radius ratio increases. Figure 3.5(b) shows the effect of radius ratio on the boundary layer thicknesses over the inner and outer

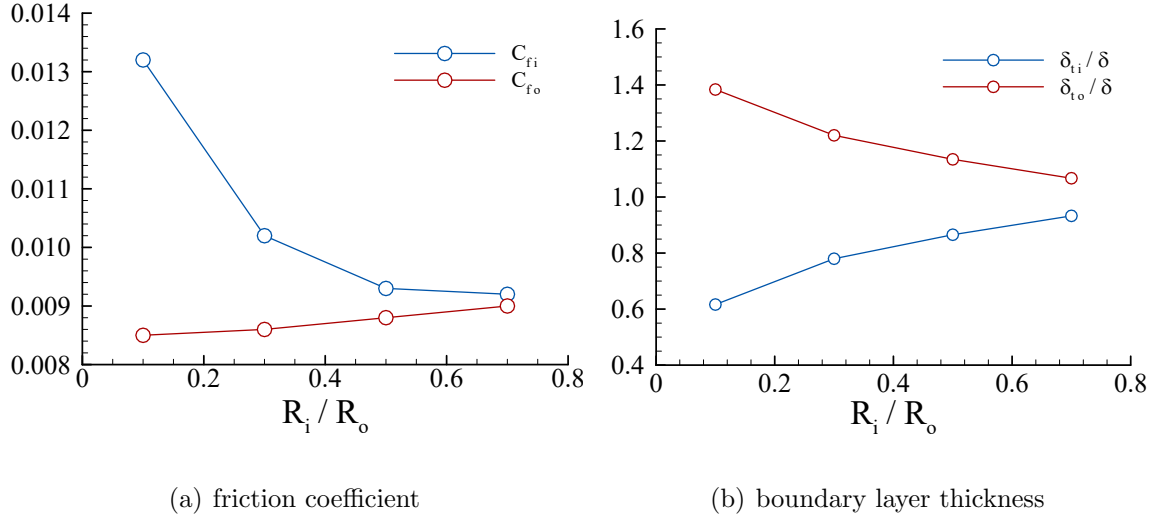


Figure 3.5: Profiles of skin friction coefficient and boundary layer thickness of the inner and outer cylindrical walls in concentric annular pipe for all four test cases.

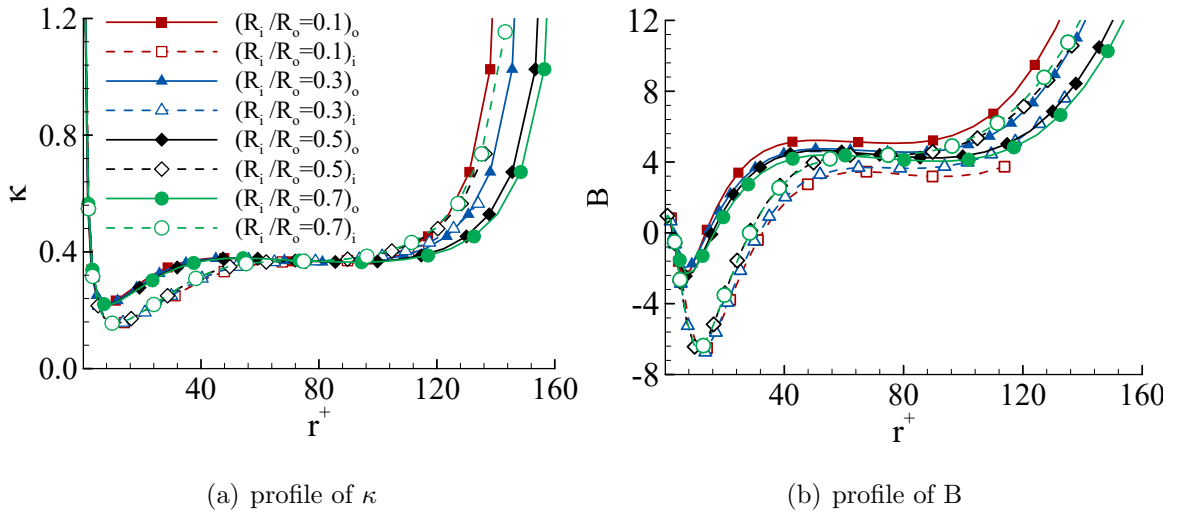


Figure 3.6: Values of constants κ and B of the logarithmic law of the wall associated with the mean axial flow in a concentric annular pipe for all cases.

sides of the concentric annular pipe. As the radius ratio increases, the boundary layer thicknesses (δ_{ti} and δ_{to}) of the inner and outer sides of the concentric annular pipe decreases and increases, respectively.

The law-of-the-wall can be derived by postulating a length scale $\ell = \kappa r$. Here, κ is the von Kármán constant, which reflects the ratio of the outer length scale to

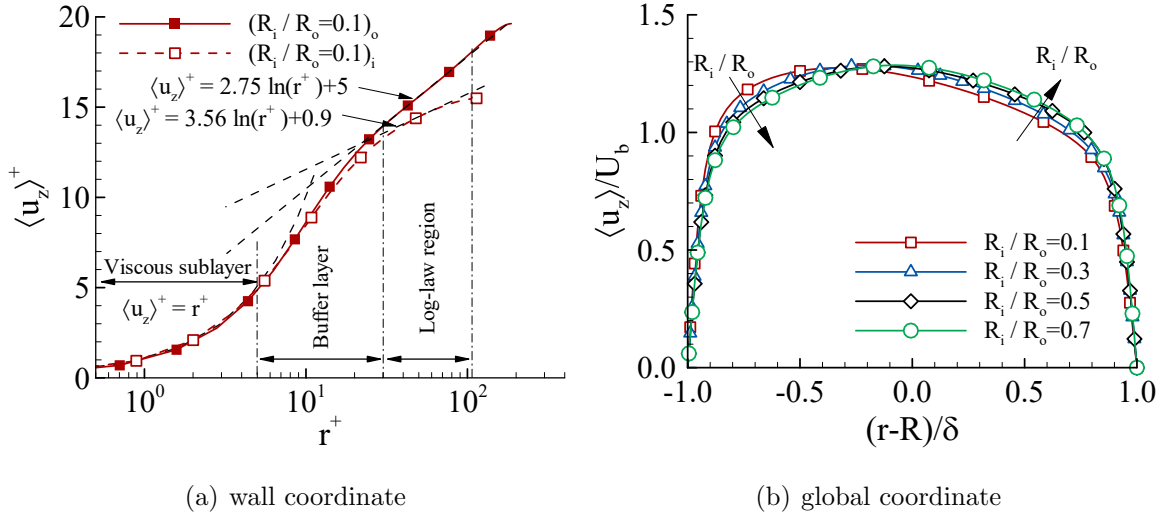


Figure 3.7: Profile of the mean axial velocity $\langle u_z \rangle^+$. (a) in wall coordinate for case $R_i/R_o = 0.1$, and (b) in non-dimensionalized global coordinate $(r - R)/\delta$ for all test cases.

the viscous length scale (Adrian, 2007). The law of the wall in the log-law region is expressed as:

$$\langle u_z \rangle^+ = \frac{1}{\kappa} \ln(r^+) + B \quad . \quad (3.6)$$

Direct numerical simulation enables us to accurately evaluate the constants κ and B in the context of a concentric annular pipe flow. The Kármán constant is determined as

$$\frac{1}{\kappa} = r^+ \frac{\partial \langle u_z \rangle^+}{\partial r^+} \quad . \quad (3.7)$$

Plugging Eq. (3.7) into Eq. (3.6), we obtain

$$B = \langle u_z \rangle^+ - r^+ \frac{\partial \langle u_z \rangle^+}{\partial r^+} \ln(r^+) \quad . \quad (3.8)$$

Figures 3.6(a) and 3.6(b) compare the values of κ and B on the inner and outer cylinder sides of the concentric annular pipe of the four test cases. In both figures, a plateau region presents, where the values of these two constants are relatively stable and close to their classical values in the context of zero-pressure-gradient (ZPG) boundary layer developed over a flat plate, i.e. $\kappa = 0.41$ and $B = 5.0$. Clearly, as

the radius ratio decreases, the plateau region is reduced, especially near the inner wall. Figure 3.7(a) contrasts the axial mean velocity profiles on the inner and outer cylinder sides in the wall coordinate for the test case of $R_i/R_o = 0.1$.

The reason this test case is selected is that the curvature difference between the inner and outer cylinder walls is the most distinct among all the test cases, which facilitates our investigation of the curvature effect on the scaling laws of the mean axial velocity profile of a concentric annular pipe flow. The velocity profiles of both the inner and outer walls strictly follow the linear law-of-the-wall in the viscous sublayer (i.e., $\langle u_z \rangle^+ = r^+$). The log-law region is wider on the outer wall side than on the inner wall side, which is consistent with a greater plateau region of the outer wall shown in Fig. 3.6(a). Figure 3.7(b) compares the mean velocity profiles of all cases along with the DNS data of Chung et al. (2002) with respect to the global coordinate ($r - R$). An excellent agreement is observed between the current results and the reference data of Chung et al. (2002) for the cases $R_i/R_o = 0.1$ and 0.5, which confirm the predictive accuracy of the computer DNS in terms of the mean velocity of the concentric turbulent annular pipe flow. Clearly, the boundary layer evolving over the outer cylinder surface is thicker than that over the inner cylinder surface (i.e., $\delta_{to} > \delta_{ti}$). The characteristics of the turbulent boundary layer near the inner cylinder surface with higher velocities are similar to those of an accelerating boundary layer. From Fig. 3.7(b), it is clear that the effect of radius ratio on the profile shape of the mean axial velocity is limited. In the following, we will show that by contrast, the second-order statistical moments of the velocity field are much more sensitive to the radius ratio.

Figure 3.8 compares the profiles of the Reynolds normal stresses of four test cases on both the inner and outer cylinder sides. The Reynolds normal stresses are scaled based on the local friction velocities of the inner and outer cylinder walls accordingly. From Fig. 3.8, the radius ratio effects can be readily identified by comparing the results on the inner and outer cylinder sides of each case. The position of the peak

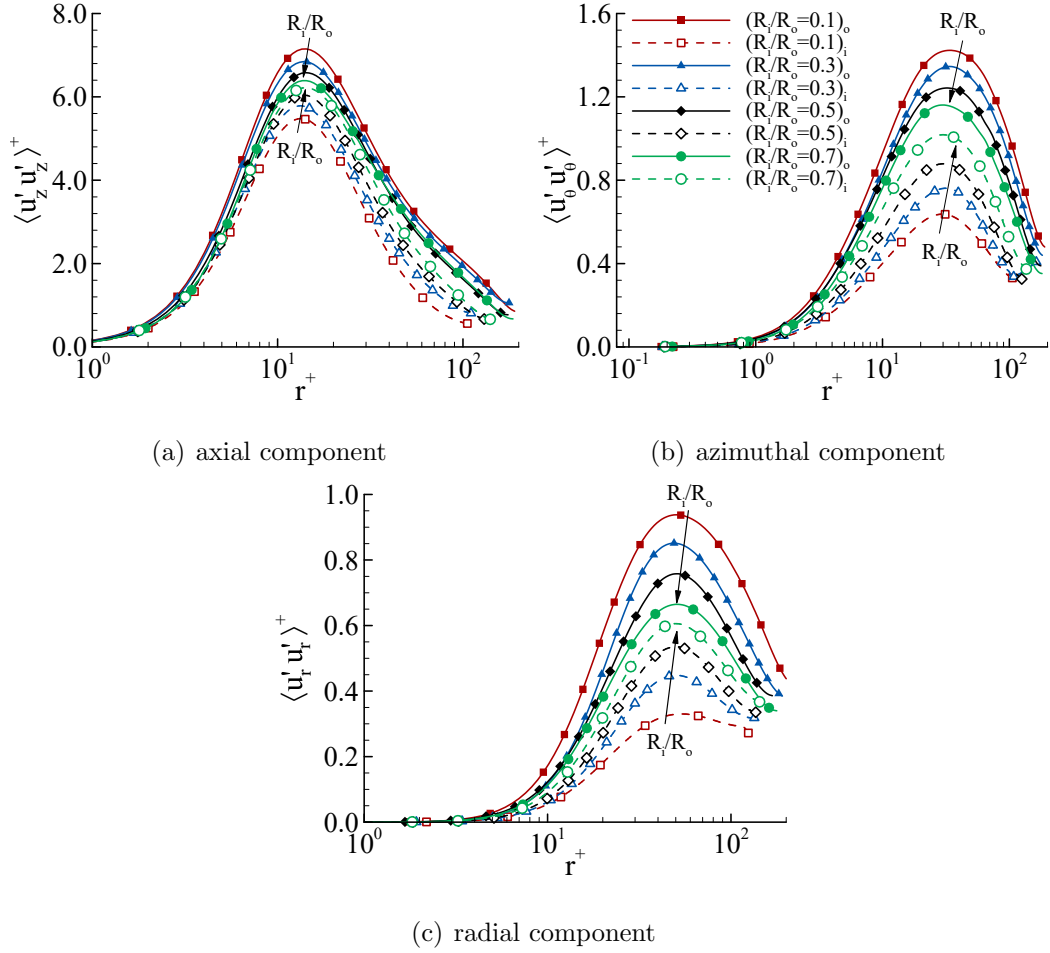


Figure 3.8: Profiles of Reynolds normal stresses at various radius ratios. Arrow points to the direction of an increasing radius ratio R_i/R_o .

is consistent near the inner and outer cylinder walls in all cases, which occurs at $r^+ \approx 15, 30$ and 50 for the axial, azimuthal and radial components of Reynolds normal stresses, respectively. The magnitude of turbulence intensity associated with the axial velocity fluctuations is the highest, followed by the components of the azimuthal and radial velocity fluctuations. The difference between the inner and outer cylinder walls becomes less apparent as the radius ratio increases. It is worth noting that the radial and azimuthal components of turbulence intensity are more sensitive to the radius ratio than is the axial component.

3.2.3 Interaction of the inner and outer boundary layers

The study of the Reynolds shear stress is the key to a better understanding the interaction between the inner and outer boundary layers. The radial position where the Reynolds shear stress equals zero divides the inner and outer boundary layers. At this special radial position, the mean axial velocity $\langle u_z \rangle / U_b$ reaches its maximum in Fig. 3.7(b). Figures 3.9(a) and 3.9(b) compare the Reynolds shear stresses of four test cases with respect to the wall-normal distance h (measured from the inner cylinder wall) and wall coordinate r^+ , respectively. The DNS data of Chung et al. (2002) are also plotted in Fig. 3.9(a) for the cases $R_i/R_o = 0.1$ and 0.5 for the purpose of comparison, which show a good agreement with the current DNS results.

From Fig. 3.9(a), it is clear that zero-crossing point (where $-\langle u'_z u'_r \rangle^+ = 0$ and $d\langle u_z \rangle / dr = 0$) deviates significantly from the cylindrical channel center ($h/\delta = 1$). However, as the radius ratio increases, this zero-crossing point shifts monotonically towards the cylindrical channel center, as a result of reduced curvature difference. In Fig. 3.9(b), the magnitude of $-\langle u'_z u'_r \rangle^+$ is apparently smaller on the inner side than on the outer side, implying that the boundary-layer developed on the inner cylinder side contains a smaller range of turbulence scales than the boundary-layer developed on outer cylinder side. Furthermore, as is evident in Fig. 3.9(a), the magnitude of the Reynolds shear stress $-\langle u'_z u'_r \rangle^+$ is higher on the outer cylinder side than on the inner cylinder side. The difference between these two sides of the concentric annular pipe becomes more pronounced as the radius ratio decreases. Clearly, as the radius ratio value increases from $R_i/R_o = 0.1$ to 0.7 , the profile of the Reynolds shear stress $-\langle u'_z u'_r \rangle^+$ becomes increasingly symmetrical in Fig. 3.9(a), indicating that the degree of curvature difference between the two cylinder walls reduces. In fact, as the radius ratio further approaches the ideal value of unity (i.e., $R_i/R_o \rightarrow 0.1$), the curvature effect vanishes, as the flow configuration becomes that of a plane-channel flow, which has a symmetrical Reynolds shear stress profile across the channel, with the zero-crossing point located exactly at the plane-channel center. From Fig. 3.9(a),

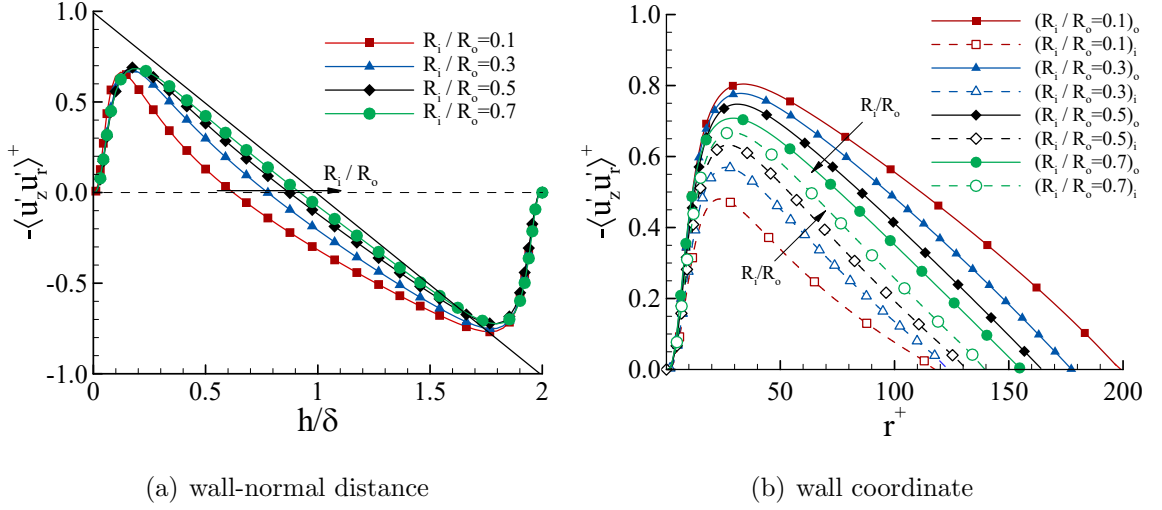


Figure 3.9: Profiles of Reynolds shear stress $\langle u'_z u'_r \rangle^+$ at various radius ratios with respect to (a) wall-normal distance h/δ (measured from the inner wall, the Reynolds shear stress is non-dimensionalized by the average wall friction velocity u_τ), (b) wall coordinate (both the Reynolds shear stress and wall coordinate are non-dimensionalized based on the local wall friction velocity, i.e. $u_{\tau i}$ or $u_{\tau o}$ for the inner or outer cylinder side, respectively). Arrow points to the direction of an increasing radius ratio R_i/R_o

the boundary layer thickness δ_{ti} or δ_{to} can be determined by finding the point where $-\langle u'_z u'_r \rangle^+ = 0$. Values of the boundary layer thicknesses have been presented in Table 3.2 and Fig. 3.5(b).

The boundary layer thickness (δ_t) of a fully-developed concentric annular pipe flow can be also determined analytically. A further study of the momentum equation of the mean axial velocity can provide a deeper understanding of the balance of the Reynolds shear stress $-\langle u'_z u'_r \rangle$. Considering that the flow is statistically stationary and homogeneous in the z - θ plane, the following can be derived from momentum equation:

$$\frac{\tau_{\text{tot}}}{\rho} = \nu \frac{d\langle u_z \rangle}{dr} - \langle u'_z u'_r \rangle = \frac{\Pi}{2\rho} r + \frac{D}{r} \quad , \quad (3.9)$$

and D is a constant of integration given as

$$D = \frac{R_o^2 R_i u_{\tau i}^2 + R_i^2 R_o u_{\tau o}^2}{R_o^2 - R_i^2} \quad . \quad (3.10)$$

The mean axial pressure gradient is balanced by the wall friction shear stresses τ_{wi} and τ_{wo} at the inner and outer cylinder surfaces, expressed as

$$\Pi = -\frac{2\rho}{R_o^2 - R_i^2}(R_o u_{\tau o}^2 + R_i u_{\tau i}^2) \quad . \quad (3.11)$$

Substituting Eqs. (3.10) and (3.11) into Eq. (2.5), the following total shear stress is obtain:

$$\frac{\tau_{\text{tot}}}{\rho} = -\frac{1}{r(R_o^2 - R_i^2)} [R_o(r^2 - R_i^2)u_{\tau o}^2 + R_i(r^2 - R_o^2)u_{\tau i}^2] \quad . \quad (3.12)$$

The radial position r_m where $\tau_{\text{tot}} = 0$ (and where the Reynolds shear stress vanishes and the mean axial velocity $\langle u_z \rangle$ reaches its maximum) can be further expressed based on the friction velocities at the two cylinder walls as

$$r_m = \sqrt{-\frac{2\rho D}{\Pi}} = \sqrt{\frac{R_o^2 R_i u_{\tau i}^2 + R_i^2 R_o u_{\tau o}^2}{R_i u_{\tau i}^2 + R_o u_{\tau o}^2}} \quad , \quad (3.13)$$

or, in a non-dimensional form

$$\frac{r_m}{R_o} = \sqrt{\frac{(u_{\tau i}/u_{\tau o})^2 + R_i/R_o}{(u_{\tau i}/u_{\tau o})^2 + R_o/R_i}} \quad , \quad (3.14)$$

which shows clearly that the value of r_m is purely determined by the radius ratio R_i/R_o and the friction velocity ratio $u_{\tau i}/u_{\tau o}$. The value of R_i/R_o is a direct indication of the curvature difference between the two cylindrical surfaces of a concentric annular pipe while the value of $u_{\tau i}/u_{\tau o}$ is a direct consequence of the surface curvature difference. Now, the boundary layer thickness for the inner and outer sides can be alternatively calculated as $\delta_{ti} = r_m - R_i$ and $\delta_{to} = R_o - r_m$ for the inner and outer sides, respectively. The values of δ_{ti} and δ_{to} are given in Table 3.2.

To further study the interaction of the inner and outer boundary layers, the transport equation of Reynolds shear stress for a steady-state flow can be studied, which reads

$$\frac{D\langle u'_z u'_r \rangle}{Dt} = 0 = \Pi_{zr} + P_{zr} + D_{zr} + T_{zr} + \varepsilon_{zr} \quad , \quad (3.15)$$

where the left hand side is the material derivative of the Reynolds stress, and the terms on the right hand side of the above equation are the velocity-pressure-gradient term

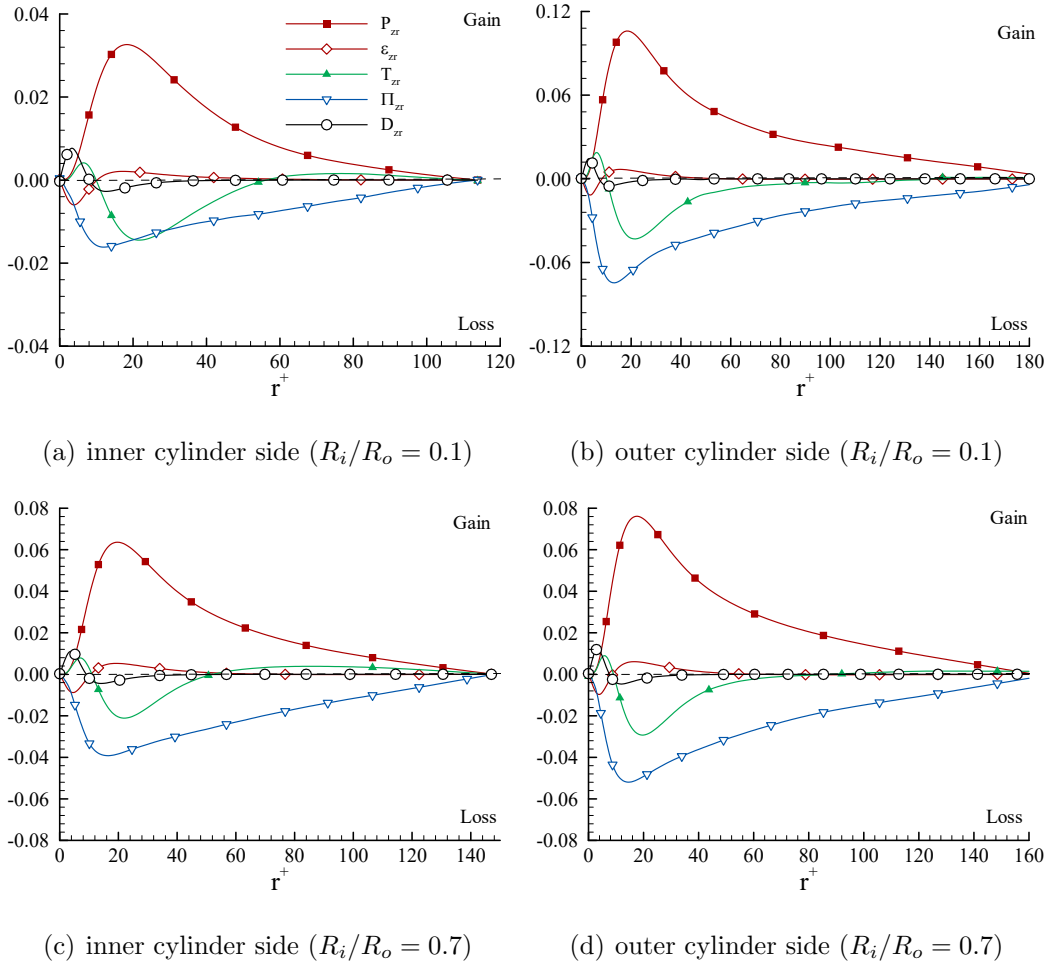


Figure 3.10: Profiles of the budget term of Reynolds shear stress $\langle u'_z u'_r \rangle$ of cases $R_i/R_o = 0.1$ and $R_i/R_o = 0.7$. All budget terms have been non-dimensionalized using local friction velocity ($u_{\tau i}$ or $u_{\tau o}$) and ν .

(Π_{zr}), production term (P_{zr}), viscous dissipation term (D_{zr}), turbulent diffusion term (T_{zr}) and dissipation term (ε_{zr}), respectively. Given that the flow is homogeneous in

the axial and azimuthal directions, these budget terms are expressed as

$$\Pi_{zr} = \frac{-1}{\rho} \left(\left\langle u'_z \frac{\partial p'}{\partial r} \right\rangle + \left\langle u'_r \frac{\partial p'}{\partial z} \right\rangle \right) , \quad (3.16a)$$

$$P_{zr} = - \langle u'_r u'_r \rangle \frac{\partial \langle u_z \rangle}{\partial r} , \quad (3.16b)$$

$$D_{zr} = \nu \left(\frac{\partial^2 \langle u'_z u'_r \rangle}{\partial r^2} + \frac{1}{r} \frac{\partial \langle u'_z u'_r \rangle}{\partial r} - \frac{\langle u'_z u'_r \rangle}{r^2} \right) , \quad (3.16c)$$

$$T_{zr} = - \frac{\partial \langle u'_z u'_r u'_r \rangle}{\partial r} - \frac{\langle u'_z u'_r u'_r \rangle}{r} + \frac{\langle u'_z u'_\theta u'_\theta \rangle}{r} , \quad (3.16d)$$

$$\varepsilon_{zr} = -2\nu \left(\left\langle \frac{\partial u'_z}{\partial r} \frac{\partial u'_r}{\partial r} \right\rangle + \frac{1}{r^2} \left\langle \frac{\partial u'_z}{\partial \theta} \frac{\partial u'_r}{\partial \theta} \right\rangle + \left\langle \frac{\partial u'_z}{\partial z} \frac{\partial u'_r}{\partial z} \right\rangle + \left\langle \frac{u'_z}{r^2} \frac{\partial u'_\theta}{\partial \theta} \right\rangle \right) . \quad (3.16e)$$

To effectively investigate the curvature effects on the interaction between the inner and outer boundary layers, here we only consider the cases of $R_i/R_o = 0.1$ and 0.7 , which represent the lowest and highest radius ratios under current testing condition. Figure 3.10 compares the profiles of the budget terms in the transport equation of the Reynolds shear stress on the inner and outer cylinder sides for cases $R_i/R_o = 0.1$ and 0.7 . Clearly, the production, velocity-pressure-gradient, and turbulence diffusion terms dominate the budget balance. The production term (P_{zr}) is the source of TKE, which is counterbalanced by the velocity-pressure-gradient and turbulence diffusion terms (Π_{zr} and T_{zr} , respectively). The influence of the dissipation term ε_{zr} and molecular diffusion term D_{zr} on the budget balance is relatively small, which consume the Reynolds shear stress mostly in the buffer layer and the viscous sub-layer (for $r^+ < 30$). By comparing the Fig. 3.10(a) with 3.10(b) and Fig. 3.10(c) with 3.10(d), it is clear that the magnitudes of the dominant source and sink terms (i.e., the production term P_{zr} and velocity-pressure-gradient term Π_{zr} , respectively) are higher on the outer side than on the inner cylinder side for both radius ratios of $R_i/R_o = 0.1$ and 0.7 . However, as the radius ratio increases from $R_i/R_o = 0.1$ to 0.7 , the differences in the magnitudes of these two budget terms between the outer and inner cylinder side decrease, which is a reflection of the fact that the curvature difference between the

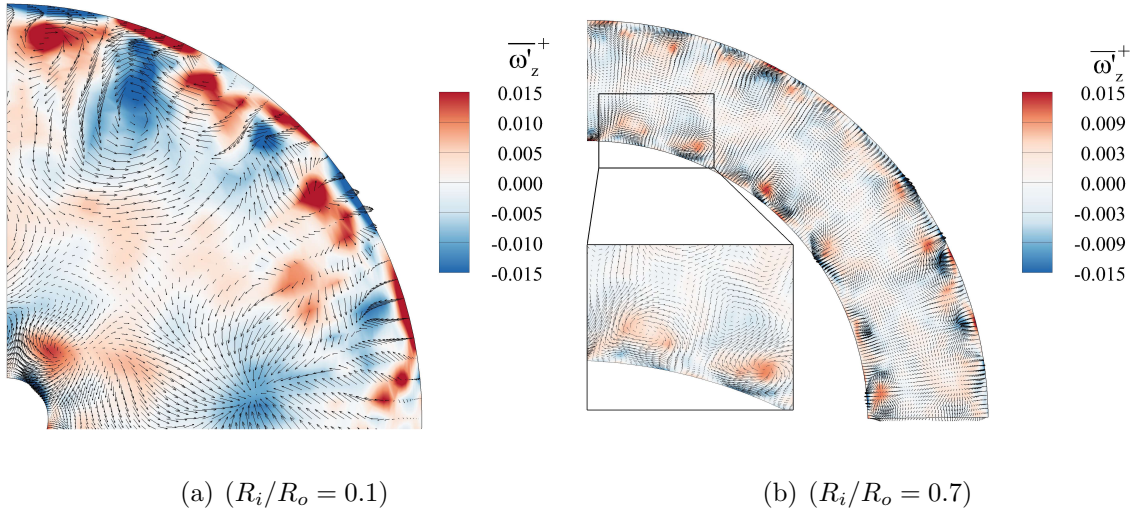


Figure 3.11: Contours of $\overline{\omega'_z}^+$ superimposed with velocity vectors composed of $\overline{u'_\theta}$ and $\overline{u'_r}$, averaged in time and axial domain for cases $R_i/R_o = 0.1$ and 0.7 . For clarity, only one-quarter of the cross-section is shown.

two cylinder walls reduces as the radius ratio increases. The turbulent diffusion term T_{zr} plays an important role in the budget balance of Reynolds shear stress, which is typically negatively valued around the peak location of the production term P_{zr} to diffuse the TKE towards the wall and the domain center as Reynolds shear stress fluxes (associated with the triple velocity terms in Eq. (3.16d)).

3.3 Turbulence structures

Thus far, the interaction of the boundary layers developed above the inner and outer cylinder surfaces has been investigated through the statistics of the velocity field and the budget balance of Reynolds shear stress. In this section, the radius ratio effects on coherent flow structures developing within these two turbulent boundary layers are examined.

As is well known, the dynamics of the turbulent boundary layer are significantly affected by the streamwise-elongated vortices (Robinson, 1991). To visualize and make

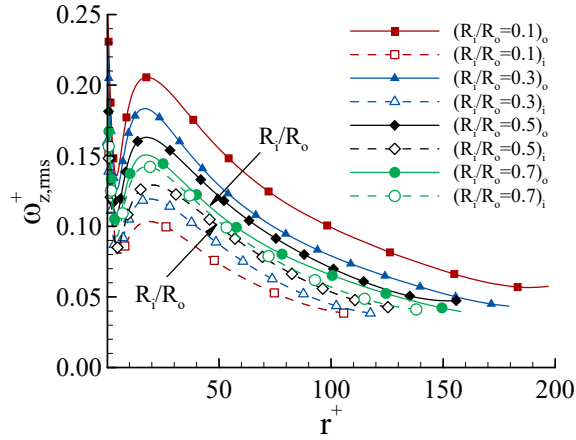


Figure 3.12: Profiles of $\omega_{z,rms}^+$ for various radius ratios.

a qualitative analysis on these vortices, we consider the time-averaged axial vorticity fluctuations ($\overline{\omega_z'^+}$). The time averaging was performed over a duration of 35 LETOTs, which ensures filtering out vortical structures that have short life spans and do not contribute to large-scale structures. Figure 3.11 compares the contours of $\overline{\omega_z'^+}$ and velocity vectors in a $r-\theta$ plane for cases of $R_i/R_o = 0.1$ and 0.7 . Only one-quarter of the cross-section is shown to ensure a clear view of the velocity field. The averaged wall friction velocity is used for non-dimensionalizing the axial vorticity fluctuations. The red and blue regions reflect positively- and negatively-valued axial vorticity fluctuations, respectively. In the azimuthal direction, contours of positively- and negatively-valued $\overline{\omega_z'^+}$ alternate, indicating that the streamwise-elongated flow structures appear in pairs, forming large-scale counter-rotating vortices. From Fig. 3.11(a), it is clear that for the case of $R_i/R_o = 0.1$, the intensity of these vertical structures is stronger on the outer side than on the inner side. However, for the case of $R_i/R_o = 0.7$ as shown in Fig. 3.11(b), the intensity of these vortical structures is similar on the inner and outer sides, as a result of a much reduced curvature difference between the two cylinder walls.

Beside the qualitative results discussed above, the characteristics of the streamwise-elongated vortices can be further precisely examined through the analysis of the axial

vorticity fluctuations in both physical and spectral spaces. Figure 3.12 compares the root mean square (RMS) profiles of the axial vorticity fluctuations $\omega_{z,rms}^+$ (non-dimensionalized based on the local mean friction velocity $u_{\tau i}$ or $u_{\tau o}$ and kinematic viscosity ν) of the four test cases with respect to the wall coordinate. From Fig. 3.12, it is clear that the local minimum and maximum of $\omega_{z,rms}^+$ occur approximately at $r^+ = 5$ and $r^+ = 20$, respectively, for all cases. This is consistent with the observation of Neves et al. (1994), who simulated a turbulent boundary layer over a cylindrical surface and showed that the locations of these local extrema remain unaffected by the transverse curvature. It is clear that the radius ratio, and correspondingly, the transverse curvature significantly affect the strength of the axial vorticity fluctuations. The axial vorticity fluctuations are stronger on the outer cylinder side than on the inner cylinder side.

To develop a deeper understanding of the effect of radius ratio on the scales of the streamwise vortical structures, the spectrum of the axial vorticity fluctuations can be further examined. The 2D spectrum of the axial vorticity fluctuations can be calculated through the Fourier transform of the axial vorticity fluctuation and multiplying the result with its conjugate, i.e.

$$\check{\phi}(k_z, k_\theta, r) = \overline{2\widehat{\omega}_z'(k_z, k_\theta, r)\widehat{\omega}_z'^*(k_z, k_\theta, r)} \quad , \quad (3.17)$$

In Eq. (3.17), the one-dimensional (1D) axial vorticity spectrum can be directly computed by integration over azimuthal wavenumbers, as $\check{\phi}_z(k_z, r) = k_{\theta 0} \sum_{k_\theta} \check{\phi}(k_z, k_\theta, r)$. The 1D azimuthal vorticity spectrum can be defined in a similar way by integrating $\check{\phi}_z(k_z, k_\theta, r)$ over k_z , as $\check{\phi}_\theta(k_\theta, r) = k_{z 0} \sum_{k_z} \check{\phi}(k_z, k_\theta, r)$. Figure 3.13 shows the pre-multiplied 1D spectra of vorticity fluctuations of all four cases in the axial and azimuthal directions at $r^+ = 20$, where the local maximum RMS value of axial vorticity fluctuation $\omega_{z,rms}^+$ occurs according to our previous analysis of Fig. 3.12. From both Figs. 3.13(a) and 3.13(b), it is clear that in both the axial and azimuthal directions, as the radius ratio R_i/R_o increases, the modes of both $k_z^+ \check{\phi}_z^+$ and $k_\theta^+ \check{\phi}_\theta^+$ shift to longer

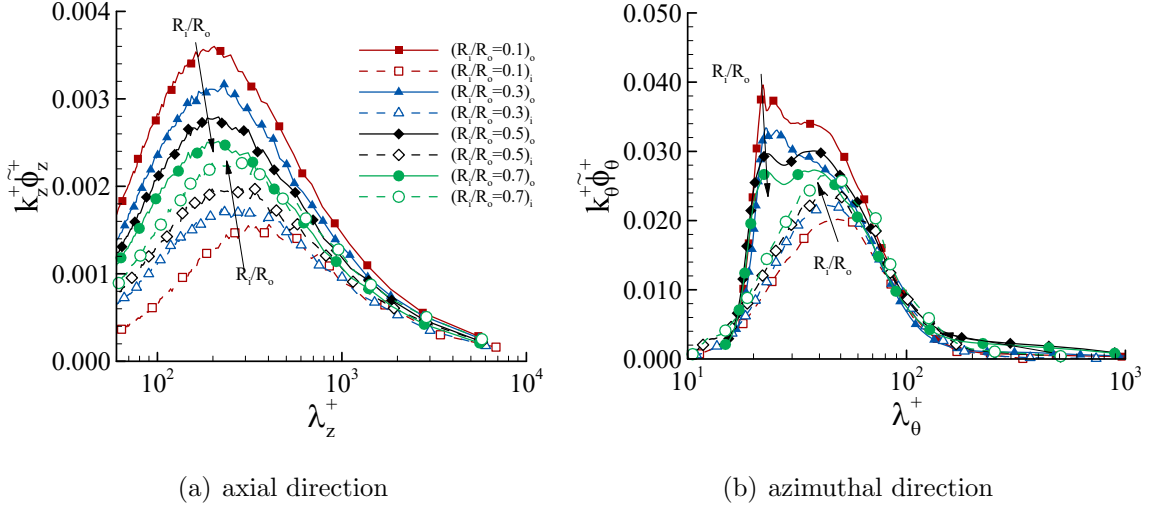


Figure 3.13: Profiles of the premultiplied 1D spectra of axial vorticity fluctuations $k_z^+ \tilde{\phi}_z^+(k_z, r)$ and $k_\theta^+ \tilde{\phi}_\theta^+(k_\theta, r)$ in the axial and azimuthal directions for the four test cases at surface located at wall-normal position $r^+ = 20$.

wavelengths while their peak values reduce monotonically on the outer cylinder side. By contrast, the premultiplied 1D spectra $k_z^+ \tilde{\phi}_z^+$ and $k_\theta^+ \tilde{\phi}_\theta^+$ exhibit opposite trends on the inner cylinder side. At this near-wall position of $r^+ = 20$, the flow is dominated by streamwise vortical structure. The axial mode of $k_z^+ \tilde{\phi}_z^+$ indicates the characteristic axial length scale of the streamwise vortical structures, which varies from $\lambda_z^+ = 200$ on the outer cylinder side to $\lambda_z^+ = 400$ on the inner cylinder side in the case of $R_i/R_o = 0.1$. While, the azimuthal mode of $k_\theta^+ \tilde{\phi}_\theta^+$ varies from $\lambda_\theta^+ = 20$ on the cylinder outer side to $\lambda_\theta^+ = 50$ on the inner cylinder side in the case of $R_i/R_o = 0.1$. These modes represent the characteristic length scales of the energetic streamwise vortices in the axial and azimuthal directions. Clearly, the axial and azimuthal characteristic length scales of the streamwise vortices are larger on the inner side than on the outer side.

As the distance from the wall increases, the flow field becomes dominated by energy-containing structures known as hairpin structures. The physical background that streaky and hairpin structures dominate the near-wall and core turbulence regions in a concentric annular pipe flow is similar to that in a boundary-layer flow over a

flat plate (Adrian, 2007). Figure 3.14 compares instantaneous contours of the swirling strength (for $\lambda_{ci} = 1.25$) of two cases of $R_i/R_o = 0.1$ and 0.7 , which have the lowest and highest radius ratios, respectively. In order to improve the visual effects here, only a portion of the computational domain is plotted for each test case. In addition, the domain is divided radially into two parts to clearly show the hairpin structures on the inner and outer cylinder sides. To facilitate identification of counter-rotating hairpin legs, the iso-surfaces of the swirling strength are further superimposed with colors based on the value of non-dimensionalized instantaneous axial vorticity $\omega_z'^+$. By comparing Figs. 3.14(a) and 3.14(b), it is clear that the hairpin structures are less populated on the inner cylinder side than on the outer cylinder side for the radius ratio of $R_i/R_o = 0.1$. However, by comparing Figs. 3.14(c) and 3.14(d), it is seen that as the radius ratio increases from $R_i/R_o = 0.1$ to 0.7 , the difference in the density of hairpin structures between the inner and outer cylinder sides reduces, as a direct result of reduced curvature difference between these two cylinder surfaces.

The premultiplied 1D energy spectra of the axial velocity fluctuation in axial ($k_z^+ \tilde{E}_{zz}^+$) and azimuthal ($k_\theta^+ \tilde{E}_{zz}^+$) directions is advantageous in precisely identifying the characteristic wavelengths (λ_z^+ and λ_θ^+) of these structures. Figure 3.15 compares premultiplied 1D axial and azimuthal spectra of axial velocity fluctuations $k_z^+ \tilde{E}_{zz}^+$ and $k_\theta^+ \tilde{E}_{zz}^+$, in core turbulent regions at $\delta_{ti}/2$ and $\delta_{to}/2$ well above the inner and the outer cylinder walls, respectively. The reason these two wall-normal positions are selected is that hairpin structures are the most populated at these elevations. By comparing Fig. 3.15 with Fig. 3.13, it is seen that the premultiplied 1D axial and azimuthal spectra of axial velocity fluctuations (u_z') exhibit some similar feature to those of axial vorticity fluctuations (ω_z'). However, it should be indicated that Fig. 3.13 is plotted at a near-wall elevation of $r^+ = 20$, which is meant to show the energy level and characteristic length scales of streamwise-elongated energetic vortical structures (or, streaky structures) near the wall. By contrast, Fig. 3.15 is plotted to show the hairpin structures that are populated in the core turbulence regions relatively far

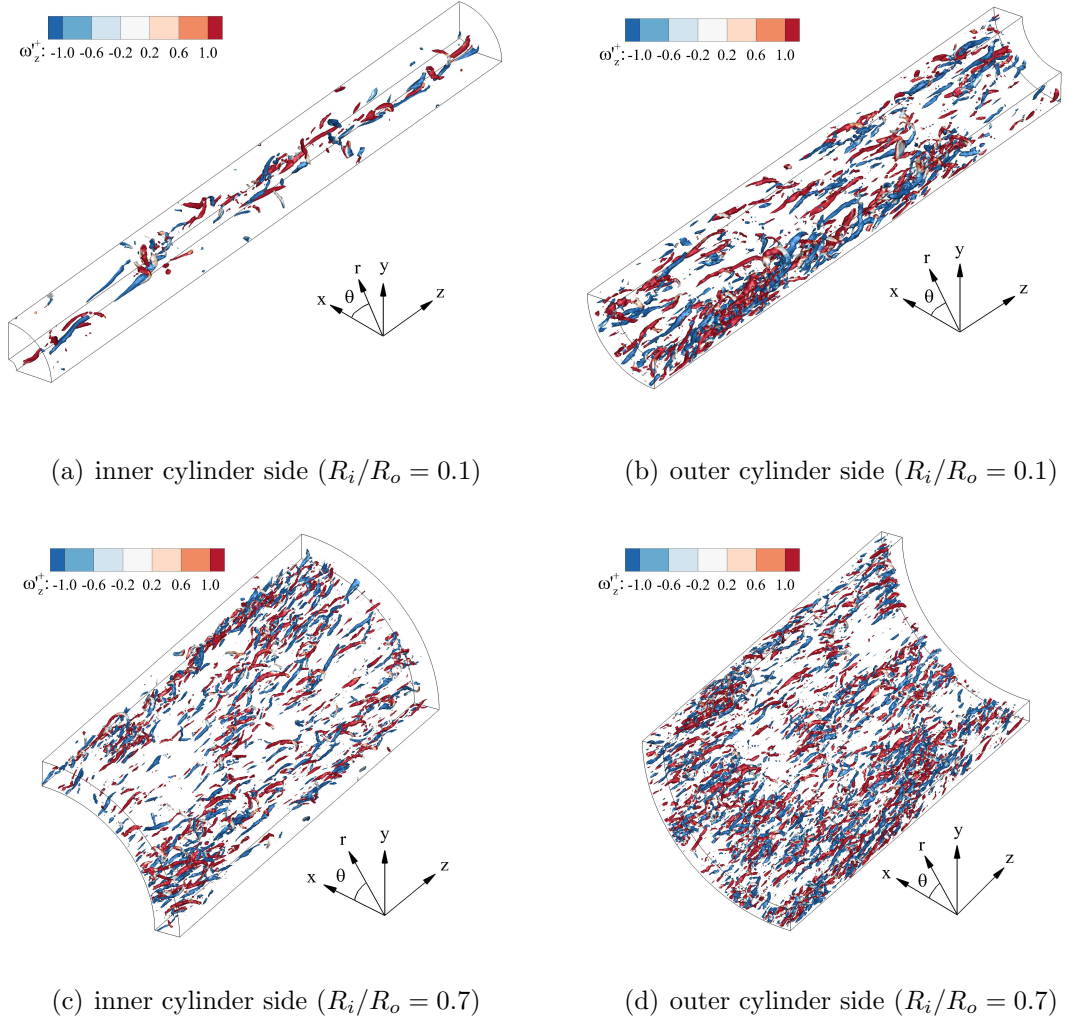


Figure 3.14: Contours of swirling strength ($\lambda_{ci} = 1.25$) of cases $R_i/R_o = 0.1$ and 0.7 . The contours are colored with instantaneous axial vorticity $\omega_z'^+$. For clarity, only a portion of the computational domain is displayed with $L_z = 6\pi\delta$ and $L_\theta = \pi/2$ for all four panels.

from the inner and outer cylinder walls at $\delta_{ti}/2$ and $\delta_{to}/2$, respectively. The modes shown in Figs. 3.15(a) and 3.15(b) represent the characteristic length scales of hairpin structures in the axial and azimuthal directions, respectively. From Fig. 3.15(a), it is clear that the axial mode of $k_z^+ \tilde{E}_{zz}^+$ varies from $\lambda_z^+ = 400$ on the cylinder outer side to $\lambda_z^+ = 700$ on the inner cylinder side in the case of $R_i/R_o = 0.1$. Figure 3.15(b) shows the effect of radius ratio on the azimuthal scale of hairpin structures. Although

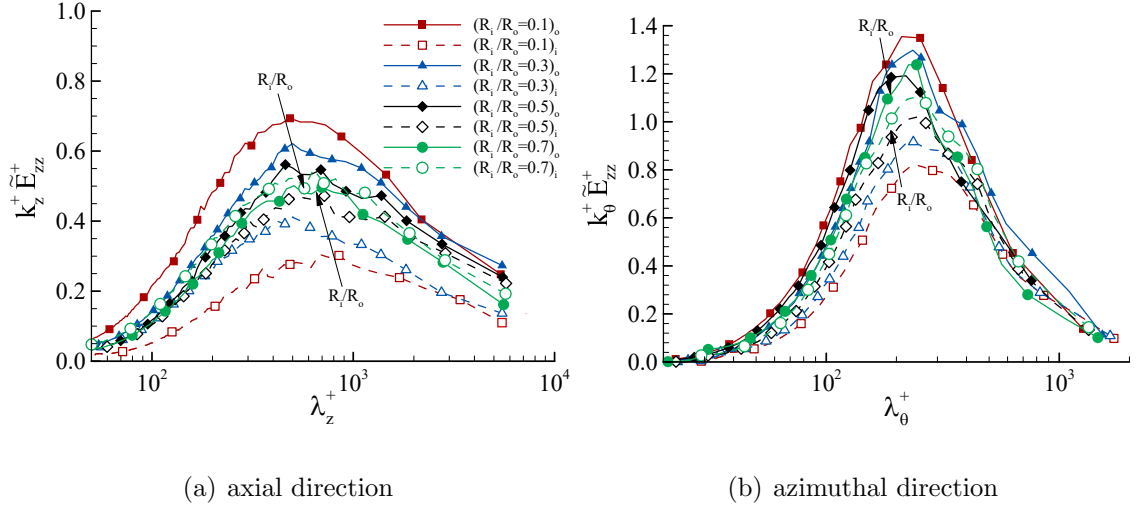


Figure 3.15: Profiles of the premultiplied 1D spectra of axial velocity fluctuations (u'_z) $k_z^+ \tilde{E}_{zz}^+(k_z, r)$ and $k_\theta^+ \tilde{E}_{zz}^+(k_z, r)$ in the axial and azimuthal directions for the four cases at $\delta_{ti}/2$ and $\delta_{to}/2$ in core turbulence region relatively far above the inner and outer cylinder walls, respectively.

some weak monotonic trend can be still observed, the azimuthal mode of $k_\theta^+ \tilde{E}_{zz}^+$ does not vary significantly, which occurs at $\lambda_\theta^+ = 200-300$. The variation of these modes reflects the curvature difference between the inner and outer cylinder walls due to the change of the radius ratio. These quantitative results from the spectral analysis well explain the qualitative results observed previously in Fig. 3.14. From Fig. 3.15(a), it is seen that as the radius ratio increases, the axial characteristic length scale of hairpin structures decreases and increases monotonically on the inner and outer cylinder sides, respectively. The hairpin structures are longer on the inner cylinder side than on the outer cylinder side at all radius ratios. Furthermore, the energy level of the hairpin structures is lower on the inner cylinder side than on the outer cylinder side. As the radius ratio increases, the difference in the energy level between the inner and outer cylinder sides reduces monotonically, which is a reflection of decreased curvature difference between the two cylinder walls.

Chapter 4

Direct Numerical Simulation of Turbulent Heat Transfer in Concentric Annular Pipe Flows

As reviewed in chapter 1, although there has been multiple experimental and RANS studies of turbulent heat transfer in concentric annular pipe flow for different radius ratios, the number of detailed DNS studies is still rather limited. In view of this, we aim at conducting a systematic comparative DNS study of the turbulent heat transfer in concentric annular pipe flow based on four radius ratios (for $R_i/R_o = 0.1, 0.3, 0.5$ and 0.7) at a nominal Reynolds number of $Re_{D_h} = 17700$. Specifically, we will examine the effects of radius ratio on the first- and second-order statistical moments of the temperature field, interaction of the thermal boundary layers developed over the inner and outer cylinder walls, spectra of the temperature fields, budget balance of temperature variance and turbulent heat fluxes, and the length scales of the thermal structures near the inner and outer cylinder walls.

The organization of the remainder of this chapter is as follows: in section 4.1, the test case and the numerical algorithm for solving the governing equations are described, and sufficiency of the selected computational domain for accurately pre-

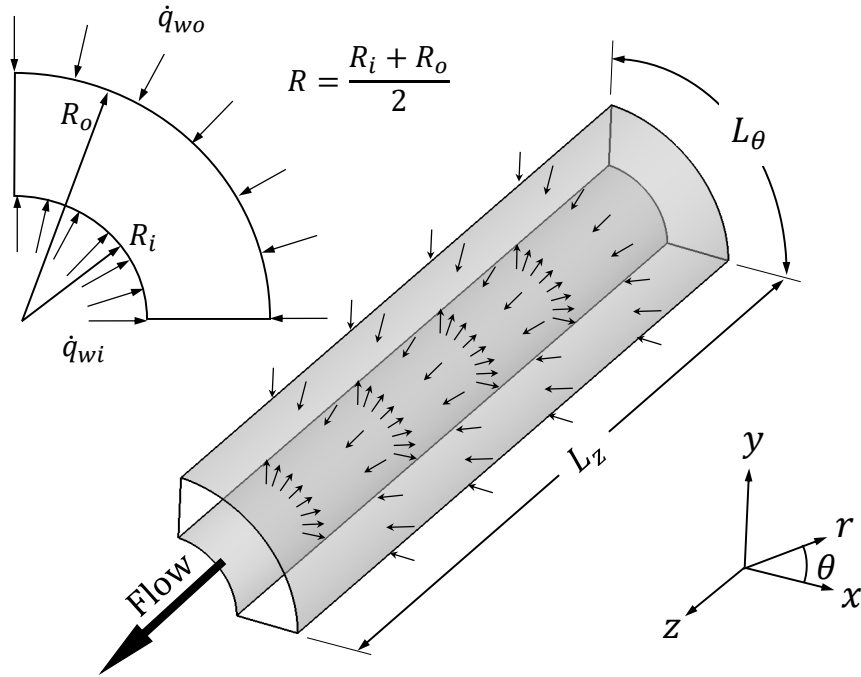


Figure 4.1: Computational domain and coordinate system. The flow is heated under a uniform wall heat flux condition ($\dot{q}_w = \dot{q}_{wi} = \dot{q}_{wo}$) through the inner and outer cylinder walls.

dicting the temperature field is studied. In section 4.2, the DNS results of various radius ratio cases are compared and analyzed. Finally, in section 4.3, the effects of radius ratio on the scales of thermal coherent structures are investigated.

4.1 Test cases and numerical algorithm

Fig. 4.1 shows the schematic diagram and coordinate system of the concentric annular flow under testing. Here z , θ , and r represent the axial, azimuthal and radial coordinates, respectively. Correspondingly, u_z , u_θ and u_r represent velocity components in these three directions. The fluid properties, including density and viscosity, are assumed to be constant. Hence, the temperature is considered to be a passive scalar, with a constant Prandtl number of 0.71. The continuity, momentum and thermal energy equations that govern the process of turbulent heat transfer in

the context of an incompressible flow are expressed as

$$\nabla \cdot \vec{u} = 0 \quad , \quad (4.1)$$

$$\frac{\partial \vec{u}}{\partial t} + \vec{u} \cdot \nabla \vec{u} = -\frac{1}{\rho} \nabla p + \nu \nabla^2 \vec{u} - \frac{\Pi}{\rho} \hat{\mathbf{e}}_z \quad , \quad (4.2)$$

$$\frac{\partial \Theta}{\partial t} + \vec{u} \cdot \nabla \Theta = u_z \frac{dT_w}{dz} + \alpha \nabla^2 \Theta \quad . \quad (4.3)$$

Here, \vec{u} , p , ρ , and α represent the velocity vector, pressure, density, and thermal diffusivity of the fluid, respectively. In Eq. (4.2), $\hat{\mathbf{e}}_z$ is the base unit vector of the z -direction, with $|\hat{\mathbf{e}}_z| \equiv 1$. In Eqs. (4.2) and (4.3), Π and dT_w/dz denote the constant mean axial pressure gradient that drives the flow, and the mean axial wall-temperature gradient characteristic of surface heating under a constant surface heat flux condition. Here, $T_w = T_w(z)$ represents the local mean wall temperature of the inner and outer cylinder surfaces at a given axial position, and $\Theta = T_w - T$ is the deficit temperature relative to T_w . By definition, $\Theta \equiv 0$ holds at both cylinder walls.

As shown in Fig. 4.1, the flow is fully developed both hydraulically and thermally. No-slip boundary conditions are enforced at the cylinder walls for the velocity field. Periodic boundary conditions are applied in the axial and azimuthal directions for both the velocity field and the deficit temperature (Θ) field. This treatment method for the temperature field is similar to that used in the numerical studies of turbulent heat transfer in rotating square duct flows by Pallares and Davidson (2002) and Fang and Wang (2018). Given the uniform surface heat flux boundary condition ($\dot{q}_w = \dot{q}_{wi} = \dot{q}_{wo}$), both the bulk mean temperature (T_b) and the local mean peripheral temperature of the walls ($\langle T_w \rangle$) increase linearly in the axial direction at the same constant rate (i.e., $dT_w/dz = dT_b/dz$). Furthermore, for a thermally fully developed flow, the deficit temperature Θ is invariant along the axial direction such that $dT_w/dz = d\langle T \rangle/dz$. The mean axial wall-temperature gradient can be evaluated by applying the principle of energy conservation to a differential control volume to

obtain

$$\frac{d\langle T \rangle}{dz} = \frac{dT_b}{dz} = \frac{dT_w}{dz} = \frac{2(\dot{q}_{wi}R_i + \dot{q}_{wo}R_o)}{\rho C_p U_b (R_o^2 - R_i^2)} \quad (4.4)$$

where, C_p is the specific heat of the fluid under constant pressure.

In this chapter, an instantaneous turbulence variable (for example, Θ) is decomposed into an averaged and a fluctuating components, i.e. $\Theta = \langle \Theta \rangle + \Theta'$. Here, a pair of angular brackets $\langle \cdot \rangle$ denotes temporal and spatial averaging. More specifically, the spatial averaging is performed over a homogeneous z - θ cylindrical surface at an arbitrary radial position r , and temporal averaging was performed over 35 large-eddy turnover times (LETOTs). Here, a LETOT is defined as δ/u_τ . The non-dimensionalized temperature with respect to the wall coordinate is defined as $\Theta^- = \Theta/T_{\tau i}$ and $\Theta^+ = \Theta/T_{\tau o}$, depending on the inner or outer cylinder side of the flow. The wall friction temperatures on the inner and outer cylinder sides of the concentric annular pipe are defined as $T_{\tau i} = \dot{q}_{wi}/\rho C_p u_{\tau i}$ and $T_{\tau o} = \dot{q}_{wo}/\rho C_p u_{\tau o}$, respectively. The mean wall friction temperature is defined as $T_\tau = (\dot{q}_{wi}R_i + \dot{q}_{wo}R_o)/(\rho C_p u_\tau (R_i + R_o))$. The computational time step used is kept at $0.001\delta/U_b$ to keep the Courant-Friedrichs-Lewy (CFL) number less than 0.8. All computations were performed on the WestGrid (Western Canada Research Grid) supercomputers. Required CPU hours to conduct a DNS varies depending on the number of grid points. Test cases $R_i/R_o = 0.1$ and 0.5 are the most and the least expensive test cases, which were performed using 19,271 and 16,617 CPU hours, respectively. In order to save storage memory, all averaging has been done during simulation and no instantaneous velocity field was saved for the purpose of post-processing. Furthermore, spectral accuracy was ensured during computation of temperature statistics.

Table 4.1 summarizes the computational domain size and grid resolution of the four test cases of different radius ratios. Equally-spaced grid points were used in both axial and azimuthal directions and Chebyshev-Gause-Lobatto points were applied to the radial direction. In Table 4.1, wall coordinates are indicated using superscript '+', which are non-dimensionalized based on ν and wall friction velocity $u_{\tau i} = \sqrt{\tau_{wi}/\rho}$

Table 4.1: Summary of test cases, grid resolutions, wall friction velocity [m/s] and friction temperature [°C].

R_i/R_o	0.1	0.3	0.5	0.7
$N_z \times N_\theta \times N_r$	$580 \times 540 \times 144$	$580 \times 540 \times 144$	$500 \times 280 \times 144$	$500 \times 360 \times 144$
$L_z \times L_\theta \times L_r$	$8\pi\delta \times 2\pi \times 2\delta$	$8\pi\delta \times 3\pi/2 \times 2\delta$	$8\pi\delta \times \pi/2 \times 2\delta$	$8\pi\delta \times \pi/2 \times 2\delta$
Δz_i^+	14.940	13.237	14.443	14.270
Δz_o^+	11.917	11.840	13.647	13.556
$\Delta r_{min,i}^+$	0.104	0.096	0.088	0.092
$\Delta r_{min,o}^+$	0.084	0.088	0.083	0.090
Δr_{max}^+	7.551	7.318	7.015	7.412
$(R_i\Delta\theta)^+$	0.781	2.265	3.227	5.774
$(R_o\Delta\theta)^+$	7.102	6.793	6.099	7.834
u_{τ_i}	0.078	0.071	0.065	0.064
u_{τ_o}	0.060	0.061	0.062	0.063
T_{τ_i}	12.82	14.08	15.38	15.62
T_{τ_o}	16.66	16.39	16.13	15.87

or $u_{\tau_o} = \sqrt{\tau_{wo}/\rho}$ for the inner and outer cylinder sides, respectively. The values of u_{τ_i} and u_{τ_o} are given in the table. In order to ensure the high spatial accuracy demanded by DNS, the grid resolution is kept for $\Delta z_i^+ \leq 14.940$ and $r\Delta\theta^+ \leq 7.834$ in the axial and azimuthal directions, respectively. The radial resolution is kept for $\Delta r^+ \leq 0.104$ near the walls and for $\Delta r^+ \leq 7.551$ in the central domain. In our study of the near-wall grid resolutions and wall-scaling behaviors, the wall units are typically calculated ‘locally’ based on either u_{τ_i} or u_{τ_o} , depending on the inner or the outer cylinder side under consideration. In this research, we also use the average wall friction velocity, defined as $u_\tau = \sqrt{\tau_w/\rho}$, where τ_w is the mean wall shear stress based on weighted averaging over the inner and outer cylinder walls, i.e. $\tau_w = (R_i\tau_{wi} + R_o\tau_{wo})/(R_i + R_o)$. The mean wall friction velocity u_τ is typically used in a ‘global’ non-dimensionalization process when the entire flow field (between the inner and outer cylinder walls) is considered. The same principle is applied to the use of three wall friction temperatures T_{τ_i} , T_{τ_o} and T_τ defined above.

4.1.1 Justification of domain size for DNS of turbulent heat transfer

Although the pseudo-spectral method code used in this research is of a high numerical accuracy for conducting DNS, the numerical accuracy by itself is insufficient for correctly predicting the physical phenomena of turbulent heat and fluid flows. This is because turbulence consists of eddies of different wavelengths. If the computational domain is too small to allow DNS to capture the characteristic wavelengths of the most energetic eddies of turbulence, the DNS is deemed as inaccurate. This has become a well-known issue since the pioneering work of Jiménez and Moin (1991), who investigated the minimum domain size required for accurate DNS prediction of turbulence statistics of a low Reynolds number turbulent plane-channel flow. The current choice of the axial domain size of $L_z = 8\pi\delta$ is based on the conclusion of our previous systematic study of the domain size effects on the predictive accuracy of DNS of a concentric annular pipe fluid flow (Bagheri et al., 2020), which compared 14 test cases of different axial and azimuthal domain sizes at a fixed radius ratio of $R_i/R_o = 0.5$. The current research covers a wider range of radius ratios for $R_i/R_o = 0.1\text{--}0.7$, and furthermore, expands the scope of our research from fluid flow to heat transfer. Due to these two major differences, it is necessary to briefly examine whether the selected computational domain sizes of the four test cases (see Table 4.1) are sufficient for accurately conducting current DNS of turbulent heat transfer.

Similar to the velocity field, the computational domain size is expected to be large enough to resolve the essential turbulence scales of the temperature field. The scales of the turbulent temperature field can be investigated through the study of the spectra of temperature fluctuations. The two-dimensional (2D) temperature spectrum is defined as

$$\check{E}_{\Theta\Theta}(k_z, k_\theta, r) = \overline{2\hat{\Theta}'(k_z, k_\theta, r)\hat{\Theta}'^*(k_z, k_\theta, r)} \quad . \quad (4.5)$$

where $\check{E}_{\Theta\Theta}(k_z, k_\theta, r)$ is a real function of axial and azimuthal wavenumbers and radius,

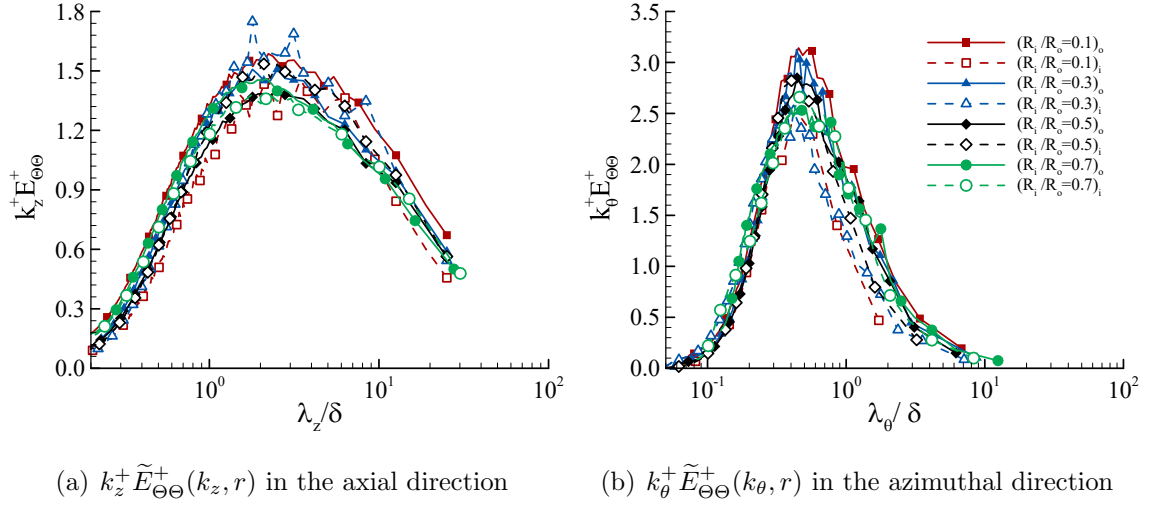


Figure 4.2: Profiles of the premultiplied 1D spectra of temperature fluctuations, (a) in the axial direction, and (b) azimuthal direction for the four cases at $r^+ = 15$, where the temperature variance peaks.

$\hat{\Theta}'$ represents a Fourier coefficient of Θ' , $\hat{\Theta}'^*$ denotes the complex conjugate of $\hat{\Theta}'$, and the overline denotes averaging over time. Also in the above equations, k_z and k_θ denote the axial and azimuthal wavenumbers, respectively. These two wavenumbers are determined as $k_z = n_z k_{z0}$ and $k_\theta = n_\theta k_{\theta0}$ for $n_z \in [-N_z/2, N_z/2 - 1]$ and $n_\theta \in [-N_\theta/2, N_\theta/2 - 1]$, respectively. Here, $k_{z0} = 2\pi/L_z$ and $k_{\theta0} = 2\pi/(r \cdot L_\theta)$ are the lowest positive wavenumbers in the axial and azimuthal directions, determined directly based on the domain sizes L_z and L_θ , respectively. In Eq. (4.5), one-dimensional (1D) axial temperature spectra can be directly computed by integration over azimuthal wavenumbers, as $\tilde{E}_{\Theta\Theta}(k_z, r) = k_{\theta0} \sum_{k_\theta} \check{E}_{\Theta\Theta}(k_z, k_\theta, r)$. The 1D azimuthal temperature spectra can be defined in a similar way by integrating $\check{E}_{\Theta\Theta}(k_z, k_\theta, r)$ over k_z , as $\tilde{E}_{\Theta\Theta}(k_\theta, r) = k_{z0} \sum_{k_z} \check{E}_{\Theta\Theta}(k_z, k_\theta, r)$.

Figs. 4.2(a) and 4.2(b) compare the profiles of 1D premultiplied spectra of temperature fluctuations in the axial and azimuthal directions (i.e., $k_z^+ \tilde{E}_{\Theta\Theta}^+(\lambda_z, r)$ and $k_\theta^+ \tilde{E}_{\Theta\Theta}^+(\lambda_\theta, r)$) of all test cases, respectively. The values of $k_z^+ \tilde{E}_{\Theta\Theta}^+(\lambda_z, r)$ and $k_\theta^+ \tilde{E}_{\Theta\Theta}^+(\lambda_\theta, r)$ are calculated at $r^+ = 15$, where the temperature variance peaks. As is evident in Fig. 4.2, the premultiplied temperature spectra precisely shows the characteristic

Table 4.2: Mean temperature field parameters of all four test cases of different radius ratios.

R_i/R_o	δ_{ti}^*/δ	δ_{to}^*/δ	Pe_{τ_i}	Pe_{τ_o}	Re_{D_h}
0.1	0.620	1.380	151.56	268.98	17788
0.3	0.803	1.197	173.85	231.84	17806
0.5	0.882	1.118	179.65	215.04	17770
0.7	0.962	1.038	193.46	198.46	17823

length scale (or the mode) corresponding to the most energetic thermal structures in the axial and azimuthal directions, the turbulent scalar energy (TSE, or temperature variance, $\langle \Theta^2 \rangle$) level of large-scale structures captured at the cut-off wavelength, and the maximum axial and azimuthal wavelengths of large-scale thermal structures that can be exactly contained and simulated using the selected domain.

From Fig. 4.2, it is evident that the TSE level as indicated by the premultiplied spectrum is higher on the outer cylinder side than on the inner cylinder side in general. Furthermore, the peak value of the premultiplied spectrum $k_z^+ \tilde{E}_{\Theta\Theta}^+$ occurs on the outer cylinder side at the lowest radius ratio tested (i.e, at $R_i/R_o = 0.1$). A perusal of Fig. 4.2 further indicates that in the case of $R_i/R_o = 0.1$, the value of $k_z^+ \tilde{E}_{\Theta\Theta}^+$ at the cut-off wavelength (corresponding to the lowest wavenumber) is 31% and 42% of its peak value on the inner and outer cylinder sides of the concentric annular pipe, respectively; while the value of $k_\theta^+ \tilde{E}_{\Theta\Theta}^+$ at the cut-off wavelength is 20% and 6% of its peak value on the inner and outer cylinder sides of the concentric annular pipe, respectively. Thus, it is clear that the premultiplied spectra have been well captured, indicating that the axial and azimuthal domain sizes of all test cases are sufficient for capturing the most energetic eddy motions associated with the turbulent heat transfer process.

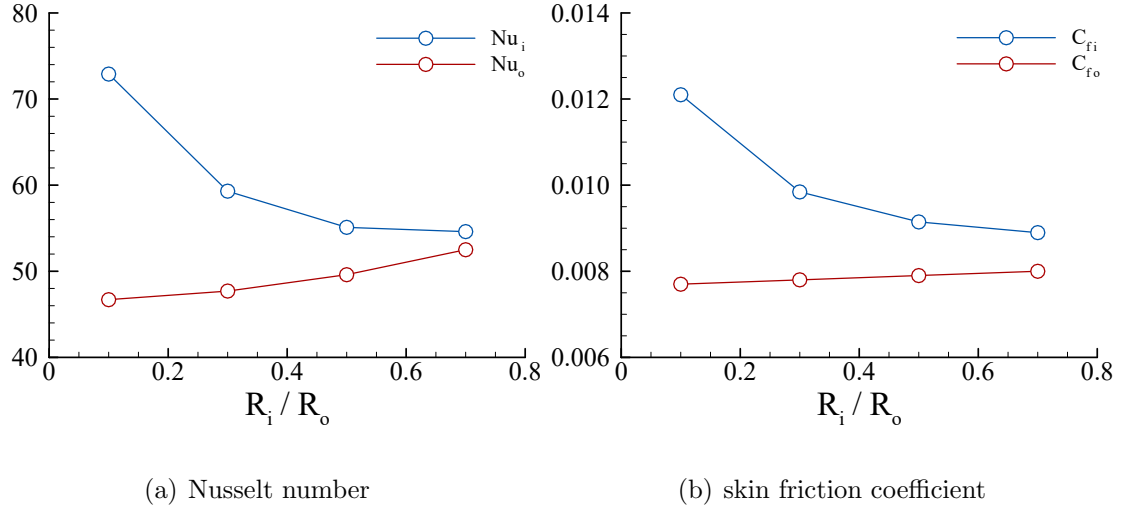


Figure 4.3: Effects of radius ratio on Nusselt number Nu and the skin friction coefficient C_f on the inner and outer cylinder sides.

4.2 Results and discussions

4.2.1 Temperature statistics

Table 4.2 shows the mean flow and thermal parameters of all four test cases. In this table, the Péclet number ($Pe_\tau = \delta_t^* u_\tau / \alpha$) is defined based on the wall friction velocity, thermal boundary layer thickness (δ_t^*) and thermal diffusivity. The Péclet number describes the ratio of convective to diffusive heat transfer rates. Given that $Pe_\tau = Re_\tau \cdot Pr$, the role of Pe_τ for the thermal energy equation is analogous to that of Re_τ for the momentum equation (Francisco et al., 2018). From table 4.2, it is clear that the value of Pe_τ is larger on the outer cylinder side than on the inner cylinder side. Moreover, this tendency enhances as the radius ratio decreases.

To evaluate the heat transfer performance, the Nusselt number can be calculated, which is defined as

$$Nu_i = \frac{D_h}{\Theta_m} \left. \frac{\partial \langle \Theta \rangle}{\partial r} \right|_{r=R_i}, \quad (4.6)$$

or

$$Nu_o = \frac{D_h}{\Theta_m} \left. \frac{\partial \langle \Theta \rangle}{\partial r} \right|_{r=R_o}, \quad (4.7)$$

depending on the inner or outer cylinder wall, respectively. Here, D_h is the hydraulic diameter and Θ_m is the bulk mean temperature, defined as:

$$\Theta_m = \frac{1}{U_b} \int_{R_i}^{R_o} \langle u_z \rangle \langle \Theta \rangle dr \quad , \quad (4.8)$$

Fig. 4.3 shows the effect of radius ratio on the skin friction coefficient and Nusselt number of the inner and outer cylinder walls. Clearly, the value of the Nusselt number on the inner cylinder wall is higher than that on the outer cylinder wall (i.e., $Nu_i > Nu_o$). The difference between the values of Nu_i and Nu_o increases significantly as the radius ratio decreases. The curvature difference between the inner (convex) and outer (concave) cylinder walls increases as the radius ratio decreases, and becomes the largest at $R_i/R_o = 0.1$ among the four test cases. From Fig. 4.3(a), it is clear that owing to the curvature difference between the inner and outer cylinder walls, the mean temperature field is asymmetrical in radial direction, and consequently, there is a discrepancy between the values of Nu_i and Nu_o . By comparing Figs. 4.3(a) and 4.3(b), it is clear that the profile shape of skin friction coefficient C_f is similar to that of Nu , which is an indication of the analogy between the momentum and thermal energy transport processes in the near-wall region. In fact, an analogy strictly holds between the velocity and temperature wall laws in the viscous sublayer, i.e., $u^+ = r^+$ versus $\Theta^+ = Pr \cdot r^+$. Further considering that $C_f \propto \partial \langle u \rangle / \partial r$ and $Nu \propto \partial \langle \Theta \rangle / \partial r$ hold in the vicinity of the wall, $C_f \propto Nu$. In other words, the magnitude of Nu is linearly proportional to that of C_f , a feature that is evident from Figs. 4.3(a) and 4.3(b).

The logarithmic law of the wall can be derived by postulating a length scale $\ell = \kappa_\Theta r$. Here, κ_Θ is the thermal Kármán constant. The law of the wall for the mean temperature in the logarithmic region can be expressed as:

$$\langle \Theta \rangle^+ = \frac{1}{\kappa_\Theta} \ln(r^+) + B_\Theta \quad . \quad (4.9)$$

DNS enables us to accurately evaluate the “constants” κ_Θ and B_Θ in the context of turbulent heat transfer in a concentric annular pipe. The value of κ_Θ is determined

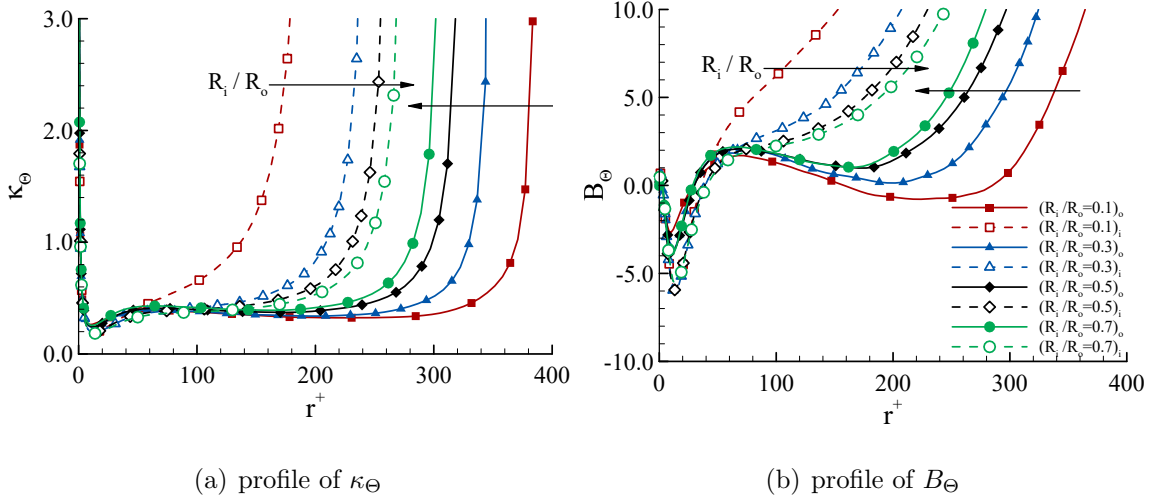


Figure 4.4: Values of constants κ_Θ and B_Θ of the logarithmic law of the wall associated with the mean axial flow in a concentric annular pipe for all cases. Arrow points to the direction of an increasing value of the radius ratio R_i/R_o .

as

$$\frac{1}{\kappa_\Theta} = r^+ \frac{\partial \langle \Theta \rangle^+}{\partial r^+} \quad (4.10)$$

Once the value of κ_Θ is calculated based on the mean temperature field, the value of B_Θ can be subsequently determined using Eq. 4.9. Figs. 4.4(a) and 4.4(b) compare the values of κ_Θ and B_Θ on the inner and outer cylinder sides of the concentric annular pipe of the four test cases. In both figures, a quasi plateau region presents, where the values of these two “constants” are relatively stable, for $\kappa_\Theta \approx 0.35$ and $B_\Theta \approx 1.34$. In the quasi-plateau region, the turbulent thermal boundary layer developing over the inner or outer cylindrical wall briefly exhibits a behavior that is similar to that over a flat plate. From Figs. 4.4(a) and 4.4(b), it is clear that the values of κ_Θ and B_Θ vary with not only the wall-normal distance r^+ but also the radius ratio R_i/R_o . Clearly, the influence from the surface curvature (as indicated by the radius ratio) on their values is significant. As the radius ratio decreases, the plateau region shortens rapidly, especially on the inner cylinder wall side. In fact, at the lowest radius ratio of $R_i/R_o = 0.1$, the quasi-plateau region vanishes completely on the inner cylinder side.

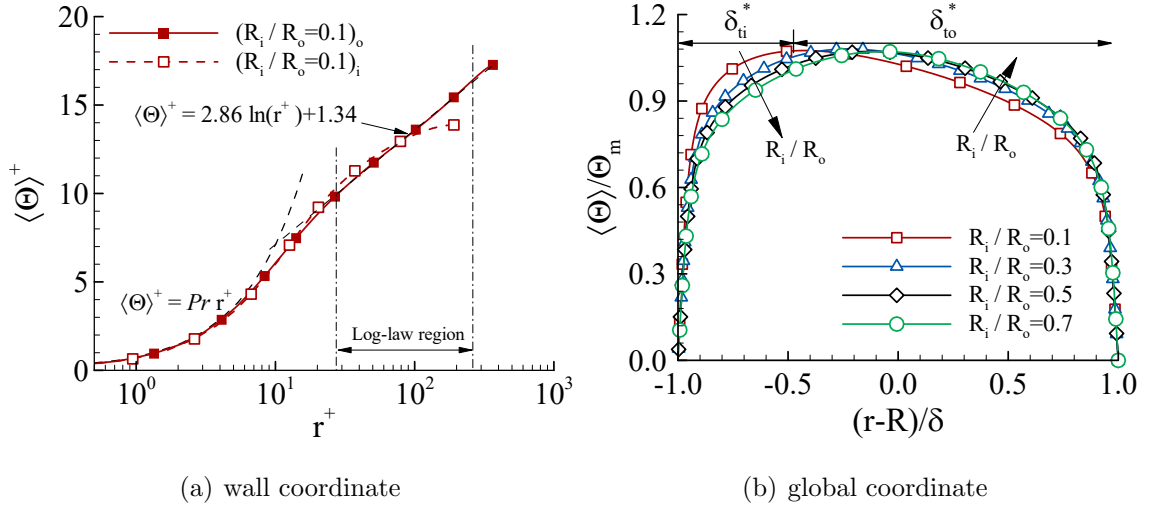


Figure 4.5: Profile of the mean temperature $\langle \Theta \rangle^+$. (a) Displayed with respect to the wall coordinate for the case of $R_i/R_o = 0.1$, and (b) displayed with respect to the non-dimensionalized global coordinate $(r - R)/\delta$ for all test cases of $R_i/R_o = 0.1-0.7$. Arrow points to the direction of an increasing value of the radius ratio R_i/R_o . In panel (b), the thermal boundary layer thicknesses, δ_{ti}^* and δ_{to}^* are labeled for the case of $R_i/R_o = 0.1$.

The curvature difference between the inner and outer cylinder walls is the largest in the case of $R_i/R_o = 0.1$, and consequently, the curvature effect on the wall scaling law of the mean temperature is also the most apparent among all four test cases. Fig. 4.5(a) compares the mean temperature profiles on the inner and outer cylinder sides in the wall coordinate for the test case of $R_i/R_o = 0.1$. From Fig. 4.5(a), it is evident that the temperature profiles of both the inner and outer cylinder walls strictly follow the linear law-of-the-wall in the conductive sublayer (i.e., $\langle \Theta \rangle^+ = Pr \cdot r^+$), where heat transfer is dominated by the molecular diffusion mechanism. Above the molecular conductive sublayer, the log-law region is much wider on the outer wall side than on the inner wall side. This is consistent with the previous analysis of Fig. 4.4(a) which shows that the quasi-plateau region is the widest on the outer cylinder side, and is the narrowest (almost non-existing) on the inner cylinder side (in the case of $R_i/R_o = 0.1$). In consequence, due to the large curvature of the convex inner cylinder wall of the case of $R_i/R_o = 0.1$, the mean temperature profile on the inner

cylinder side deviates significantly from the familiar logarithmic law, a feature that is apparent in Fig. 4.5(a). By contrast, the logarithmic law holds well on the concave outer cylinder side. This is because the surface curvature is much smaller on the outer cylinder side, and as a result, the wall scaling behavior of the mean temperature on the outer cylinder side is similar to that over a flat plate. Fig. 4.5(b) compares the mean temperature profiles of all four cases with respect to the global coordinate $(r - R)/\delta$. The thickness of the thermal boundary layer (δ_{ti}^* or δ_{to}^*) is defined as the distance from the inner or outer cylinder wall to the radial position where the mean temperature is the maximum and the radial mean temperature gradient is zero (i.e., $d\langle\Theta\rangle/dr = 0$). Clearly, owing to the curvature difference between the two cylinder walls, the thermal boundary layer is thicker over the out cylinder surface than over the inner cylinder surface (i.e., $\delta_{to}^* > \delta_{ti}^*$). The values of δ_{ti}^* and δ_{to}^* are given in Table 4.2, which clearly indicates the trends that the value of δ_{ti}^* and δ_{to}^* increases and decreases monotonically as the radius ratio R_i/R_o increases, respectively.

Fig. 4.6(a) shows the root mean square (RMS) profile of temperature fluctuations in the wall coordinate. The RMS values are scaled based on the local friction temperature of the inner and outer cylinder walls accordingly. From Fig. 4.6(a), the radius ratio effects can be readily identified by directly contrasting the results of the inner and outer cylinder sides for each test case. The mode of the profile (corresponding to peak value) is consistent in all test cases, which occurs at $r^+ \approx 15$. The peak values are higher on the outer cylinder side than on the inner cylinder side, but the difference between the inner and outer cylinder walls becomes less apparent as the radius ratio increases. Fig. 4.6(b) compares profiles of the axial turbulent heat flux $\langle\Theta'u_z'\rangle^+$ of the four test cases in wall coordinates. By comparing Figs. 4.6(b) and 4.6(a), it is clear that profiles of the axial turbulent heat flux $\langle\Theta'u_z'\rangle^+$ and RMS temperature Θ_{rms}^+ show a similar pattern. Later in section 4.8, it will be explained that these two quantities are related because $\langle\Theta'u_z'\rangle^+$ appears in the turbulence production term for the temperature variance $\langle\Theta'\Theta'\rangle^+$. Similar to the profiles of Θ_{rms}^+ , the mode of

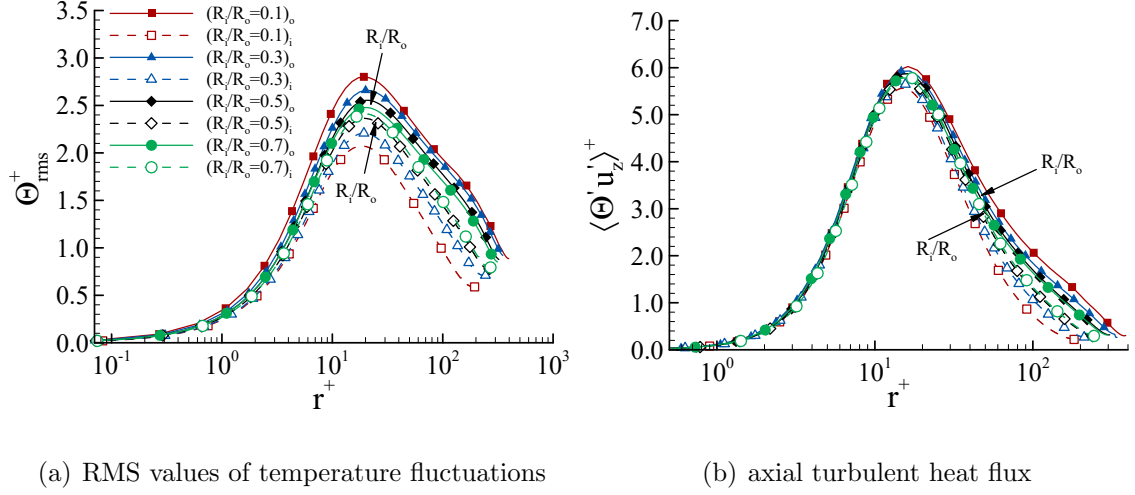


Figure 4.6: Profiles of RMS values of temperature fluctuation and axial turbulent heat flux at various radius ratios. Arrow points to the direction of an increasing value of the radius ratio R_i/R_o .

$\langle \Theta' u_z' \rangle^+$ is consistent near the inner and outer cylinder walls in all test cases, which occurs at $r^+ \approx 15$.

4.2.2 Interaction of the inner and outer thermal boundary layers

The radial position where the radial turbulent heat flux equals zero (i.e., $-\langle \Theta' u_r' \rangle = 0$) divides the inner and outer thermal boundary layers. At this special radial position, the mean temperature $\langle \Theta \rangle$ also reaches its maximum as shown in Fig. 4.5(b). Figs. 4.7(a) and 4.7(b) compare the radial turbulent heat flux ($-\langle \Theta' u_r' \rangle^+$) of the four test cases with respect to the wall-normal distance h (measured from the inner cylinder wall) and wall coordinate r^+ , respectively. From Fig. 4.7(a), it is clear that the zero-crossing point (where $-\langle \Theta' u_r' \rangle^+ = 0$ and $d\langle \Theta \rangle/dr = 0$) deviates significantly from the cylindrical channel center ($h/\delta = 1$). Owing to the curvature difference between the two cylinder walls, the profile of $-\langle \Theta' u_r' \rangle^+$ is asymmetrical about the

cylindrical channel center in the radial direction, a feature that is evident in both Figs. 4.7(a) and 4.7(b). To understand this phenomenon better, we may recall the classical heated circular pipe flow case, in which, both the Reynolds stress $-\langle u'_z u'_r \rangle^+$ and turbulent heat flux $-\langle \Theta' u'_r \rangle^+$ are symmetrical about the axial center of the circular pipe. However, for the profiles of $-\langle \Theta' u'_r \rangle^+$ of heated concentric annular pipe flows shown in Fig. 4.7(b), it is seen that the radial location of the profile peak varies from $r^+ = 20$ on the inner cylinder side to $r^+ = 50$ on the outer cylinder side in the case of $R_i/R_o = 0.1$. As the radius ratio decreases from 0.7 to 0.1, the zero-crossing point monotonically deviates from the cylindrical channel center towards the inner cylinder wall. In Fig. 4.7(b), the radial wall coordinate of the zero-crossing point of $-\langle \Theta' u'_r \rangle^+$ is smaller on the inner side than on the outer side, implying that the thermal boundary-layer developed over the inner cylinder wall contains a smaller range of turbulence scales than does the thermal boundary-layer developed over the outer cylinder wall.

4.2.3 Budget balance of transport equations

In order to develop a deeper insight into turbulent heat transfer, the transport processes of the temperature variance ($k_\Theta = \langle \Theta' \Theta' \rangle / 2$), and axial and radial turbulent heat fluxes ($\langle u'_z \Theta' \rangle$ and $\langle u'_r \Theta' \rangle$, respectively) can be further studied. The transport equations of these three turbulence quantities can be expressed, in a general form, as

$$\Pi_i + P_i + T_i + D_i + \varepsilon_i = 0 \quad . \quad (4.25)$$

The terms in order of appearance are referred to as: pressure-temperature gradient (Π_i), production (P_i), molecular diffusion (D_i), turbulent diffusion (T_i), and molecular dissipation (ε_i). The exact definitions of these terms are given in Table 4.3. In this table, subscript “ i ” appearing in the general transport Eq. (4.25) is replaced by subscripts “ Θ ”, “ z ” and “ r ” to denote the budget terms of the temperature variance,

Table 4.3: Budget terms of transport Eq. (4.25) for temperature variance k_Θ , axial turbulent heat flux $\langle u'_z \Theta' \rangle$, and radial turbulent heat flux $\langle u'_r \Theta' \rangle$.

Budget terms for k_Θ

$$P_\Theta = - \langle u'_r \Theta' \rangle \frac{\partial \langle \Theta \rangle}{\partial r} + \langle u'_z \Theta' \rangle \frac{\partial \langle T_w \rangle}{\partial z} \quad , \quad (4.11)$$

$$D_\Theta = + \frac{\nu}{2Pr} \left(\frac{\partial^2 \langle \Theta' \Theta' \rangle}{\partial r^2} + \frac{1}{r} \frac{\partial \langle \Theta' \Theta' \rangle}{\partial r} \right) \quad , \quad (4.12)$$

$$T_\Theta = - \frac{1}{2} \left(\frac{\partial \langle u'_r \Theta' \Theta' \rangle}{\partial r} + \frac{\langle u'_r \Theta' \Theta' \rangle}{r} \right) \quad , \quad (4.13)$$

$$\varepsilon_\Theta = - \frac{\nu}{Pr} \left(\left\langle \frac{\partial \Theta'}{\partial r} \frac{\partial \Theta'}{\partial r} \right\rangle + \frac{1}{r^2} \left\langle \frac{\partial \Theta'}{\partial \theta} \frac{\partial \Theta'}{\partial \theta} \right\rangle + \left\langle \frac{\partial \Theta'}{\partial z} \frac{\partial \Theta'}{\partial z} \right\rangle \right) \quad . \quad (4.14)$$

Budget terms for $\langle u'_z \Theta' \rangle$

$$\Pi_z = \frac{\partial \langle p' \Theta' \rangle}{\partial z} - \langle p' \frac{\partial \Theta'}{\partial z} \rangle \quad , \quad (4.15)$$

$$P_z = - \langle u'_r \Theta' \rangle \frac{\partial \langle u_z \rangle}{\partial r} - \langle u'_r u'_z \rangle \frac{\partial \langle \Theta \rangle}{\partial r} + \langle u'_z u'_z \rangle \frac{\partial \langle T_w \rangle}{\partial z} \quad , \quad (4.16)$$

$$D_z = \frac{\nu}{r} \frac{\partial}{\partial r} \left(r \langle \Theta' \frac{\partial u'_z}{\partial r} \rangle \right) + \frac{\nu}{Pr} \frac{1}{r} \frac{\partial}{\partial r} \left(r \langle u'_z \frac{\partial \Theta'}{\partial r} \rangle \right) \quad , \quad (4.17)$$

$$T_z = - \frac{\partial \langle u'_r u'_z \Theta' \rangle}{\partial r} - \frac{\langle u'_r u'_z \Theta' \rangle}{r} \quad , \quad (4.18)$$

$$\varepsilon_z = - \frac{\nu(Pr+1)}{Pr} \left(\left\langle \frac{\partial u'_z}{\partial r} \frac{\partial \Theta'}{\partial r} \right\rangle + \frac{1}{r^2} \left\langle \frac{\partial u'_z}{\partial \theta} \frac{\partial \Theta'}{\partial \theta} \right\rangle + \left\langle \frac{\partial u'_z}{\partial z} \frac{\partial \Theta'}{\partial z} \right\rangle \right) \quad . \quad (4.19)$$

Budget terms for $\langle u'_r \Theta' \rangle$

$$\Pi_r = - \frac{\partial \langle p' \Theta' \rangle}{\partial r} + \langle p' \frac{\partial \Theta'}{\partial r} \rangle \quad , \quad (4.20)$$

$$P_r = - \langle u'_r u'_r \rangle \frac{\partial \langle \Theta \rangle}{\partial r} + \langle u'_r u'_z \rangle \frac{\partial \langle T_w \rangle}{\partial z} \quad , \quad (4.21)$$

$$D_r = \nu \left(\frac{1}{r} \frac{\partial}{\partial r} \left(r \langle \Theta' \frac{\partial u'_r}{\partial r} \rangle \right) - \frac{\langle u'_r \Theta' \rangle}{r^2} \right) + \frac{\nu}{Pr} \frac{1}{r^2} \frac{\partial}{\partial r} \left(r \langle u'_r \frac{\partial \Theta'}{\partial r} \rangle \right) \quad , \quad (4.22)$$

$$T_r = - \frac{\partial \langle u'_r u'_r \Theta' \rangle}{\partial r} - \frac{\langle u'_r u'_r \Theta' \rangle}{r} + \frac{\langle u'_\theta u'_\theta \Theta' \rangle}{r} \quad , \quad (4.23)$$

$$\varepsilon_r = - \frac{\nu(Pr+1)}{Pr} \left(\left\langle \frac{\partial u'_r}{\partial r} \frac{\partial \Theta'}{\partial r} \right\rangle + \frac{1}{r^2} \left\langle \frac{\partial u'_r}{\partial \theta} \frac{\partial \Theta'}{\partial \theta} \right\rangle + \left\langle \frac{\partial u'_r}{\partial z} \frac{\partial \Theta'}{\partial z} \right\rangle \right) \quad . \quad (4.24)$$

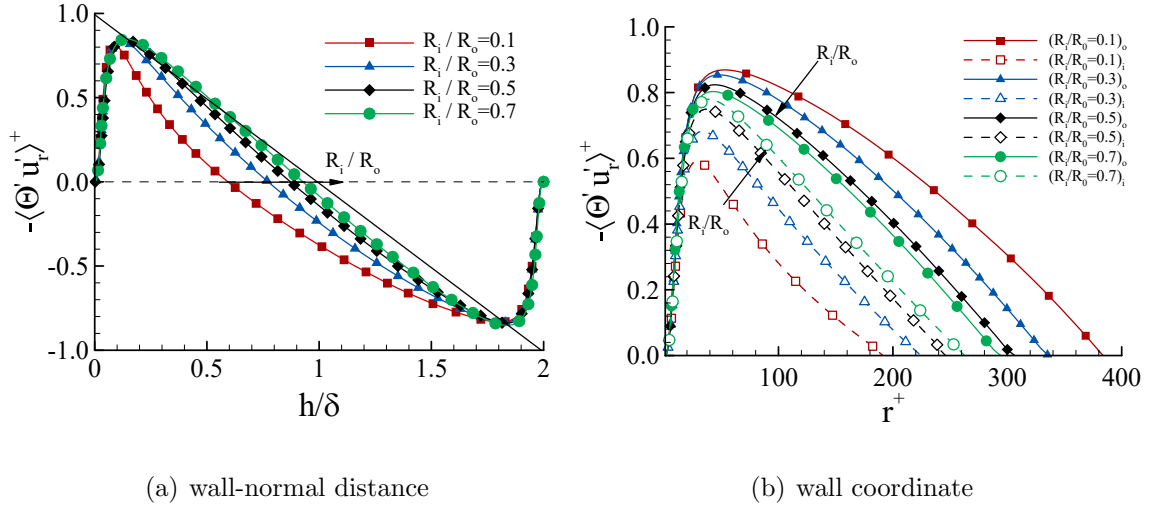
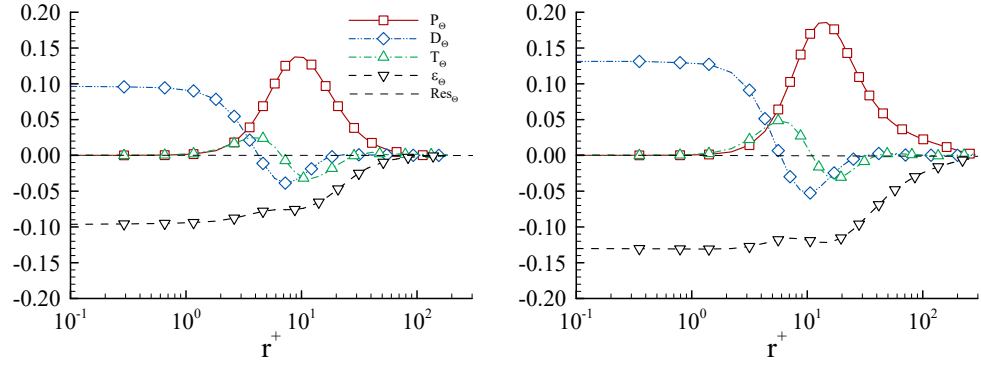


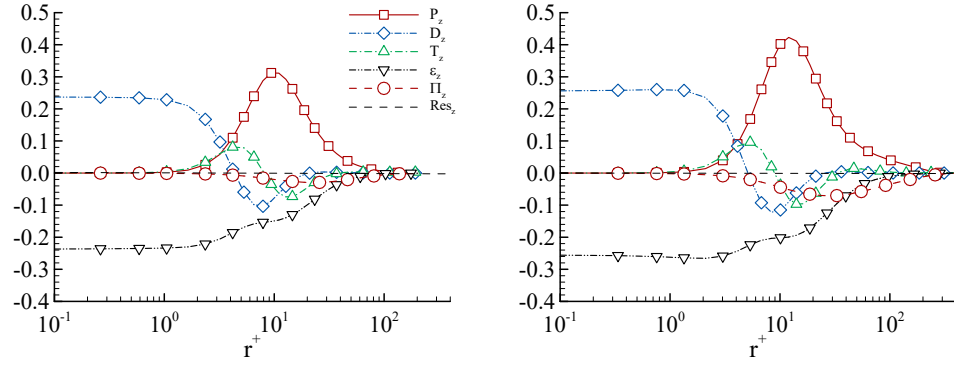
Figure 4.7: Profiles of radial turbulent heat flux $-\langle\Theta'u_r'\rangle^+$ at various radius ratios with respect to (a) wall-normal distance h/δ (measured from the inner cylinder wall, the radial turbulent heat flux is non-dimensionalized by the average friction temperature $T_\tau u_\tau$), (b) wall coordinate (both the radial turbulent flux and wall coordinate are non-dimensionalized based on the local wall friction velocity and local friction temperature, i.e. $T_{\tau i} u_{\tau i}$ or $T_{\tau o} u_{\tau o}$ for the inner or outer cylinder side, respectively). Arrow points to the direction of an increasing radius ratio R_i/R_o .

and axial and radial turbulent heat fluxes, respectively. It should be noted that the transport equation of k_Θ is free from the pressure-temperature gradient term (i.e., $\Pi_\Theta \equiv 0$).

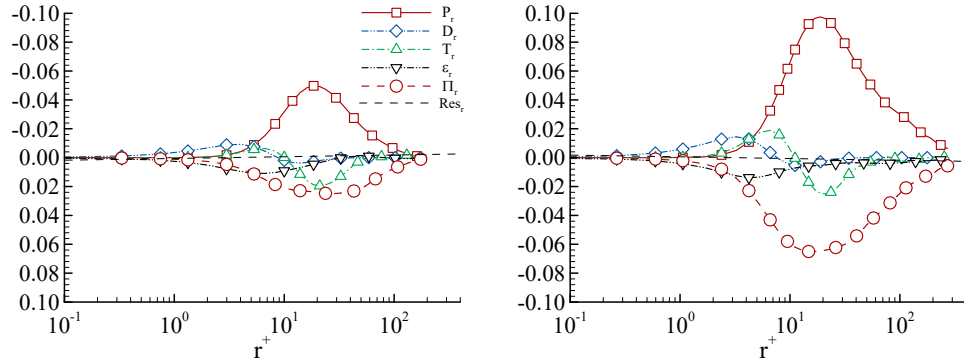
To effectively demonstrate the radius ratio effects on the budget balance of the temperature variance k_Θ and turbulent heat fluxes $\langle u'_z \Theta' \rangle$ and $\langle u'_r \Theta' \rangle$, the case of $R_i/R_o = 0.1$ is considered, which has the largest curvature difference between the inner and outer cylinder walls. Fig. 4.8 compares the profiles of the budget terms of k_Θ^+ , $\langle u'_z \Theta' \rangle^+$ and $\langle u'_r \Theta' \rangle^+$ on the inner and outer cylinder sides for the case of $R_i/R_o = 0.1$. To demonstrate the predictive accuracy of the DNS, the residual term as a result of the balance between the left- and right-hand-sides of Eq. (4.25) is also shown in the figure. The budget terms of the temperature variance is non-dimensionalized by $u_{\tau i}^2 T_{\tau i}^2 / \nu$ or $u_{\tau o}^2 T_{\tau o}^2 / \nu$, and those of the turbulent heat fluxes are non-dimensionalized by $u_{\tau i}^3 T_{\tau i} / \nu$ or $u_{\tau o}^3 T_{\tau o} / \nu$ on the inner or the outer cylinder side,



(a) Budget of $\langle u'_z \Theta' \rangle^+$ on the inner cylinder (b) Budget of $\langle u'_z \Theta' \rangle^+$ on the outer cylinder



(c) Budget of $\langle u'_z \Theta' \rangle^+$ on the inner cylinder (d) Budget of $\langle u'_z \Theta' \rangle^+$ on the outer cylinder



(e) Budget of $\langle u'_r \Theta' \rangle^+$ on the inner cylinder (f) Budget of $\langle u'_r \Theta' \rangle^+$ on the outer cylinder

Figure 4.8: Profiles of the budget terms of temperature variance (k_Θ^+), axial turbulent heat flux ($\langle \Theta' u'_z \rangle^+$) and radial turbulent heat flux ($\langle \Theta' u'_r \rangle^+$) on the inner and outer cylinder sides of the case $R_i/R_o = 0.1$. The budget terms of the temperature variance is non-dimensionalized by $u_{\tau_i}^2 T_{\tau_i}^2 / \nu$ or $u_{\tau_o}^2 T_{\tau_o}^2 / \nu$, and those of the turbulent heat fluxes are non-dimensionalized by $u_{\tau_i}^3 T_{\tau_i} / \nu$ or $u_{\tau_o}^3 T_{\tau_o} / \nu$ on the inner or the outer cylinder side, respectively.

respectively. In order to clearly demonstrate the effects of radius ratio on the budget terms in the near-wall region, their profiles are displayed in a semi-logarithmic wall coordinate. From Fig. 4.8, it is clear that there is a general trend that the magnitudes of the budget terms are larger on the outer cylinder side than on the inner cylinder side. This trend is consistent with that of the RMS temperature and turbulent heat fluxes shown previously in Fig. 4.6.

Figs. 4.8(a) and 4.8(b) compare the profiles of temperature variance on the inner and outer cylinder sides. From Fig. 4.8(a), it is seen that in the vicinity of the inner cylinder wall (for $r^+ < 3$), the budget balance is dominated by the molecular diffusion term D_Θ and molecular dissipation term ε_Θ . However, further away from the inner cylinder wall (for $r^+ > 3$), the turbulent production term P_Θ gradually becomes the dominant source for temperature fluctuations, balanced by ε_Θ , turbulent diffusion term T_Θ and molecular diffusion term D_Θ . At $r^+ = 10$, the production term P_Θ reaches its peak value. Also around this radial position, both T_Θ and D_Θ reach their negative peak values. Clearly, the role of the molecular diffusion term D_Θ is to drain the TSE (or, temperature variance) generated by the turbulent production term P_Θ at the radial position $r^+ \approx 7$ and then diffuse it to the near-wall region for further dissipation (by ε_Θ). A careful examination of the profile of the turbulent diffusion term T_Θ displayed in Fig. 4.8(b) indicates that T_Θ has a primary positive peak at $r^+ \approx 4$ and a much smaller secondary positive peak around $r^+ = 50$. Thus, it is understood that the role of the turbulent diffusion term T_Θ is to drain the production term P_Θ at $r^+ \approx 10$ and then transport the TSE primarily towards the wall and secondarily towards the center of the concentric annular passage. By comparing Fig. 4.8(a) with 4.8(b), it is clear that the profile patterns of the budget terms are similar. However, the near-wall region dominated by the molecular diffusion and dissipation is larger on the outer cylinder side than on the inner cylinder side. As a result, the peak value of the turbulent production term P_Θ is extended to $r^+ \approx 15$ on the outer cylinder side (compared to that at $r^+ \approx 10$ on the inner cylinder side).

Figs. 4.8(c) and 4.8(d) compare the profiles of axial turbulent heat flux $\langle u'_z \Theta' \rangle^+$ on the inner and outer cylinder sides for the case of $R_i/R_o = 0.1$. In general, the budget profiles of $\langle u'_z \Theta' \rangle^+$ exhibit a similar pattern to those of the temperature variance shown in Figs. 4.8(a) and 4.8(b). This is not surprising. As detailed in section 4.1, the flow (as represented by velocity \vec{u}) is driven by a constant axial pressure gradient Π , and similarly, the thermal energy (as indicated by the deficit temperature Θ) is driven by a constant axial temperature gradient (under the constant wall heat flux condition). Furthermore, the boundary conditions for the velocity field and deficit temperature are identical, which are periodic in the axial direction and zero identically at the wall. As such, for a passive heat transfer process, there is an analogy between the transport processes of the axial velocity u_z and deficit temperature Θ , and consequently, between the transport processes of $\langle \Theta' \Theta' \rangle / 2$ and $\langle u'_z \Theta' \rangle$. However, there is a difference. In the transport equation of axial turbulent heat flux $\langle u'_z \Theta' \rangle$, there is an additional term, i.e. the pressure-temperature gradient term Π_z . From Figs. 4.8(c) and 4.8(d), it is apparent that the role of the Π_z term is to reduce the axial turbulent heat flux, especially in the logarithmic region. By comparing Figs. 4.8(c) and 4.8(d), it is seen that the magnitude of Π_z is larger on the outer cylinder side than on the inner cylinder side. Furthermore, from Fig. 4.8(d), it is evident that Π_z is the primary sink term that balances the production term P_z in the logarithmic region (for $r^+ > 40$).

Figs. 4.8(e) and 4.8(f) compare the budget balances of radial turbulent heat flux $\langle u'_r \Theta' \rangle^+$ on the inner and outer cylinder sides for the case of $R_i/R_o = 0.1$. Although the profile patterns are similar between Figs. 4.8(e) and 4.8(f), the magnitudes of budget terms are much larger on the outer cylinder side than on the inner cylinder side. Furthermore, compared to Figs. 4.8(c) and 4.8(d), the impact of the pressure-temperature gradient term Π_r is significantly enhanced. In fact, as is evident in Figs. 4.8(e) and 4.8(f), Π_r is the dominant sink term in the budget balance of $\langle u'_r \Theta' \rangle^+$, especially in the central region of the concentric annular pipe.

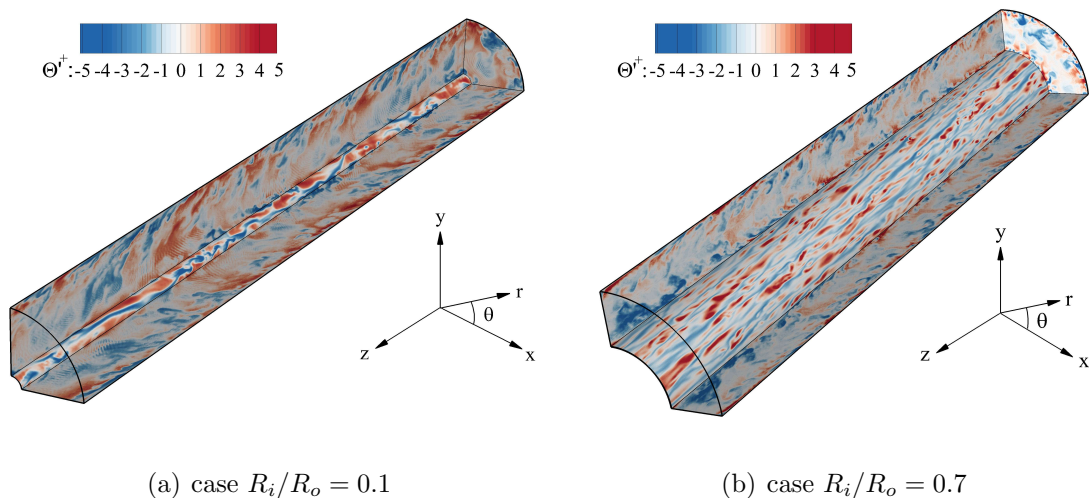


Figure 4.9: Contours of the instantaneous non-dimensionalized temperature fluctuations Θ'^+ , displayed over the cylindrical surface (or, $z-\theta$ plane) located at $r^+ = 15$ on the inner inside, and over the $z-r$ and $r-\theta$ planes on the boundaries for cases of (a) $R_i/R_o = 0.1$ and (b) $R_i/R_o = 0.7$.

4.3 Coherent structures associated with the temperature field

Fig. 4.9 shows the turbulence structures visualized using the instantaneous contours of non-dimensionalized temperature fluctuations Θ'^+ over the cylindrical surface (or, $z-\theta$ plane) located at $r^+ = 15$ on the inner cylinder side, and over the $z-r$ and $r-\theta$ planes on the boundaries for cases of $R_i/R_o = 0.1$ and 0.7 . The radius ratio effect on thermal structures can be effectively demonstrated by comparing these two test cases, as they have the smallest and largest radius ratios among the four test cases. From both Figs. 4.9(a) and 4.9(b), it is seen that at the near-wall position of $r^+ = 15$, the low- and high-TSE level thermal streaky structures alternate and are uniformly distributed in both axial and azimuthal directions. On the $z-r$ and $r-\theta$ planes displayed in Fig. 4.9, the presence of large-scale turbulent thermal structures in the log-law region referred to as ‘temperature front’ (TF) by Chen and Blackwelder (1978) is evident. These large-scale structures protrude from the near-wall

region to the log-law region, characterized by rapid temperature fluctuations associated with upwards edged turbulence structures. The spread of TSE through TFs is coupled with the hairpin structures characteristic of near-wall turbulence. The curvature difference between the inner and outer cylinder surfaces is the largest in the case of $R_i/R_o = 0.1$, but the smallest in the case of $R_i/R_o = 0.7$ among the four test cases. Consequently, as shown in the z - r and r - θ planes of Figs. 4.9(a) and 4.9(b), the protruded TF structures from outer cylinder wall are considerably more intense than those from the inner cylinder wall in the case of $R_i/R_o = 0.1$. By contrast, the intensity of protruded TF structures from the inner and outer cylinder walls is similar in the case of $R_i/R_o = 0.7$.

In order to refine the study of the effects of radius ratio on the distribution of TSE and the characteristic length scales of turbulent thermal structures, Fig. 4.10 compares the contours of 1D premultiplied spectra of temperature fluctuations in the axial ($k_z^+ \tilde{E}_{\Theta\Theta}^+$) and azimuthal ($k_\theta^+ \tilde{E}_{\Theta\Theta}^+$) directions for cases of $R_i/R_o = 0.1$ and $R_i/R_o = 0.7$. In this figure, the premultiplied spectra are presented as a function of wavelength (λ_z^+ or λ_θ^+) and wall coordinate (r^+) from the inner or outer cylinder wall. In their DNS study of turbulent plane-channel flow of Hoyas and Jiménez (2006), turbulent Couette flow of Avsarkison et al. (2014) and streamwise-rotating plane-channel flow of Yang and Wang (2018), the energetic eddy motions are distinguished at three energy levels, which correspond to the 7/8-th, 5/8-th and 3/8-th of the modal value the premultiplied spectrum of streamwise velocity fluctuations. This method of analysis of premultiplied spectrum is useful for identifying the length scales of the energetic eddy motions of fluid flows, and can be further extended to the current analysis of turbulence structures associated with temperature fluctuations in a concentric annular pipe. As such, three levels of the premultiplied spectrum are identified in Fig. 4.10, which correspond to $0.875 \max(k_i^+ \tilde{E}_{\Theta\Theta}^+)$, $0.625 \max(k_i^+ \tilde{E}_{\Theta\Theta}^+)$ and $0.375 \max(k_i^+ \tilde{E}_{\Theta\Theta}^+)$. Here, subscript “ i ” can be replaced by z or θ to indicate the axial or azimuthal direction, respectively. These three energy levels of the premultiplied spectrum correspond

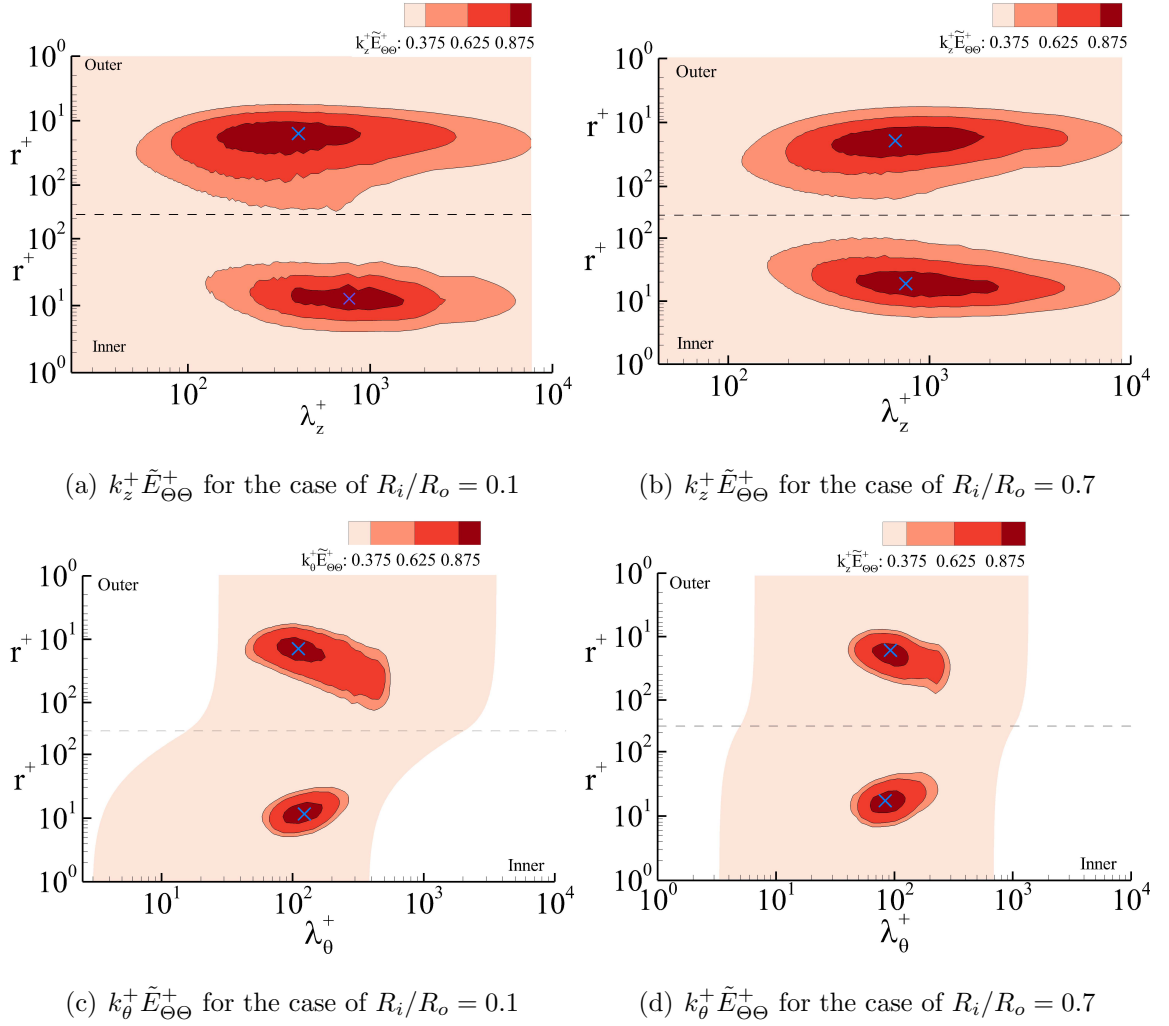


Figure 4.10: Contours of 1D premultiplied spectra of temperature fluctuations ($k_z^+ \tilde{E}_{\Theta\Theta}^+$) and ($k_\theta^+ \tilde{E}_{\Theta\Theta}^+$) in the axial and azimuthal directions, respectively, for cases of $R_i/R_o = 0.1$ and $R_i/R_o = 0.7$. The cross symbol ‘ \times ’ pinpoints the location of the mode. Three energy levels are distinguished, and the innermost, middle and outermost isopleths correspond to $0.875 \max(k_i^+ \tilde{E}_{\Theta\Theta}^+)$, $0.625 \max(k_i^+ \tilde{E}_{\Theta\Theta}^+)$ and $0.375 \max(k_i^+ \tilde{E}_{\Theta\Theta}^+)$, respectively. Besides these three isopleths which show three magnitude levels of the premultiplied spectrum relative to its peak value, the absolute magnitude of the non-dimensionalized premultiplied spectrum is also shown using a color legend. In the non-dimensionalization, the value of the wall friction velocity and temperature equal to either $u_{\tau i}$ and $T_{\tau i}$, or $u_{\tau o}$ and $T_{\tau o}$ depending on the convex (inner) or the concave (outer) cylinder side in consideration. The horizontal black dashed line demarcates the border that separates premultiplied spectrum on the inner and outer cylinder sides.

to the high-, intermediate- and low-intensity cores of turbulent thermal structures. In each figure panel, the mode is demarcated using a cross symbol “×”, and the ranges of the three energy levels are distinguished using colors and thin black borderlines. It should be indicated that although the thermal structures the low-intensity region (encompassed by the isopleth of $0.375 \max(k_i^+ \tilde{E}_{\Theta\Theta}^+)$, or the outermost isopleth of the pre-multiplied spectrum) are comparatively speaking, less energetic eddies, they still contribute significantly to the total TSE of the temperature field. This can be understood from the following identity: $\langle \Theta' \Theta' \rangle = \int_0^\infty \tilde{E}_{\Theta\Theta}(k_i, r) \cdot dk_i = \int_0^\infty [k_i \tilde{E}_{\Theta\Theta}(k_i, r)] \cdot d[\ln(k_i)]$. From this identity, it is clear that the pre-multiplied spectrum $k_i \tilde{E}_{\Theta\Theta}(k_i, r)$ can be used for identifying the characteristic length scales of the most energetic thermal structures in a logarithmic coordinate system (based on $\ln(k_i)$).

The radius ratio effects on the axial scales of turbulent thermal structures can be investigated by comparing the distribution of $k_z^+ \tilde{E}_{\Theta\Theta}^+$ in the $\lambda_z^+ - r^+$ plane of cases $R_i/R_o = 0.1$ and $R_i/R_o = 0.7$ in Figs. 4.10(a) and 4.10(b), respectively. The mode (indicated using a cross symbol “×”) of $k_z^+ \tilde{E}_{\Theta\Theta}^+$ occurs at $(r^+, \lambda_z^+) \approx (15, 800)$ and $(r^+, \lambda_z^+) \approx (15, 500)$ on the inner and outer cylinder sides, respectively, for the case of $R_i/R_o = 0.1$. However, it occurs $(r^+, \lambda_z^+) \approx (15, 700)$ and $(r^+, \lambda_z^+) \approx (15, 600)$ on the inner and outer cylinder sides for the case of $R_i/R_o = 0.7$, respectively. From Figs. 4.10(a) and 4.10(b), it is evident that the characteristic axial length scale of the thermal streaky structures (as indicated by the modal value of λ_z^+) is larger on the inner cylinder side than on the outer side. The difference in the modal value of λ_z^+ between the inner and outer cylinder sides is about 300 wall units in the case of $R_i/R_o = 0.1$, but reduces to approximately 100 wall units in the case of $R_i/R_o = 0.7$. This significant reduction in the difference of the modal values of λ_z^+ is a clear reflection of the reduced curvature difference between the inner and outer cylinder walls as the radius ratio increases from $R_i/R_o = 0.1$ to 0.7. The effects of radius ratio on the characteristic azimuthal scales of turbulent thermal structures can be identified by comparing Figs. 4.10(c) and 4.10(d). The mode of

$k_\theta^+ \tilde{E}_{\Theta\Theta}^+$ occurs at $(r^+, \lambda_\theta^+) \approx (15, 110)$ and $(r^+, \lambda_\theta^+) \approx (15, 90)$ on the inner and outer cylinder sides, respectively, in the case $R_i/R_o = 0.1$; but at $(r^+, \lambda_\theta^+) \approx (15, 100)$ on the both inner and outer cylinder sides in the case $R_i/R_o = 0.7$. Clearly, the radial distance ($r^+ \approx 15$) where the mode is located is consistent between inner and outer cylinder sides in both test cases of $R_i/R_o = 0.1$ and 0.7 . At the near-wall position of $r^+ \approx 15$, the thermal streaky structures are the most energetic. This is consistent with the previous observation of the peak position of the RMS temperature Θ_{rms} in Fig. 4.6(a). The underlying reason for this phenomenon is that the turbulent production rate is the maximum at this particular wall-normal position (see Fig. 4.8). By comparing Figs. 4.10(c) and 4.10(d), it is also clear that as the radius ratio increases from $R_i/R_o = 0.1$ to 0.7 , the characteristic azimuthal length scale of the most energetic thermal streaks remains stable, which is about $\lambda_\theta^+ \approx 100$ wall units.

From the above discussion, it is understood that at the near-wall radial position of $r^+ \approx 15$, both the temperature variance and turbulent production rate peak due to dominance of the energetic thermal streaky structures. As shown previously in Fig. 4.9, at an arbitrary higher radial position for $r^+ > 15$, the TF structures become popular, which facilitate a transport of TSE from the near-wall region to the domain center. The spectral information associated with the TFs, however, cannot be effectively shown at the near-wall radial position of $r^+ = 15$, where the thermal streaks dominate. In order to develop an understanding of the characteristic length scales of TF structures, the premultiplied temperature spectrum should be studied at a much higher radial position. To this purpose, Fig. 4.11 displays two-dimensional (2D) premultiplied spectra of temperature fluctuations on the inner and outer cylinder sides for the case of $R_i/R_o = 0.1$ at a much elevated position of one-half the thermal boundary layer (i.e., at $\delta_{ti}^*/\delta = 0.5$ or $\delta_{to}^*/\delta = 0.5$) relatively far away from each wall. Similar to Fig. 4.10, three levels of the premultiplied temperature spectrum are identified, which demarcate the high- (7/8-th of peak), intermediate- (5/8-th of

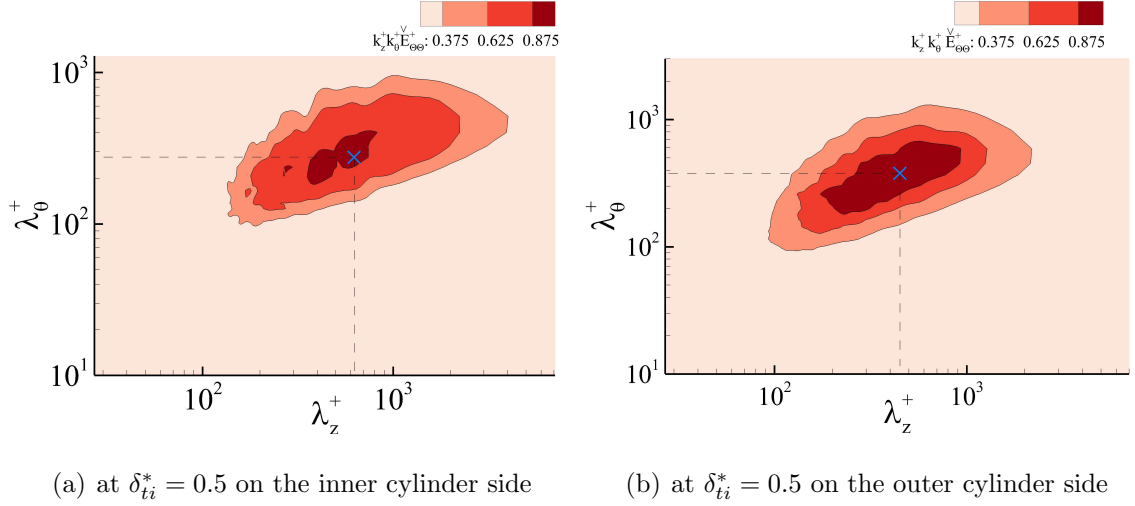


Figure 4.11: Premultiplied 2D spectra $k_z^+ k_\theta^+ \check{E}_{\Theta\Theta}^+$ on the inner and outer cylinder sides of the concentric annular pipe for the case of $R_i/R_o = 0.1$ at one-half the thermal boundary layer from the inner or outer cylinder wall (i.e., at $\delta_{ti}^*/\delta = 0.5$ or $\delta_{to}^*/\delta = 0.5$). The cross symbol ‘ \times ’ pinpoints the location of the mode. Three energy levels are distinguished, and the innermost, middle and outermost isopleths correspond to $0.875 \max(k_z^+ k_\theta^+ \check{E}_{\Theta\Theta}^+)$, $0.625 \max(k_z^+ k_\theta^+ \check{E}_{\Theta\Theta}^+)$ and $0.375 \max(k_z^+ k_\theta^+ \check{E}_{\Theta\Theta}^+)$, respectively. In the non-dimensionalization, the value of the wall friction velocity and temperature equal to either $u_{\tau i}$ and $T_{\tau i}$, or $u_{\tau o}$ and $T_{\tau o}$ depending on the convex (inner) or the concave (outer) cylinder side in consideration.

peak) and low-intensity (3/8-th of peak) cores. From Fig. 4.11, it is seen that at the high elevation of one-half thermal boundary layer away from the cylinder wall, the full ranges of axial and azimuthal wavelengths of the TF structures at all three TSE levels are well captured by DNS using the selected computational domain. Furthermore, it is observed that the modes of $k_z^+ k_\theta^+ \check{E}_{\Theta\Theta}^+$ occur at $(\lambda_z^+, \lambda_\theta^+ = 600, 280)$ and $(\lambda_z^+, \lambda_\theta^+ = 450, 180)$ on the inner and outer cylinder sides, respectively. The modal values of λ_z^+ and λ_θ^+ represent the characteristic length scales of the TF structures in the axial and azimuthal directions. The differences in the modal values of λ_z^+ and λ_θ^+ between Figs. 4.11(a) and 4.11(b) is a consequence of the surface curvature difference between the inner and outer cylinder walls. Clearly, both axial and azimuthal characteristic length scales of the TF structures are larger on the inner cylinder side than on the outer cylinder side.

Chapter 5

Conclusions and Future Work

5.1 Conclusions

In this chapter, major conclusions of this research are summarized, which include a summary of the influence of domain size on predictive accuracy of velocity and temperature fields and, the effects of radius ratio on turbulent flow, heat transfer and coherent structures in a concentric annular pipe.

5.1.1 Influence of domain size on DNS of turbulent flow in a moderately-curved concentric annular pipe

The effect of computational domain size on the predictive accuracy of DNS results of a moderately-curved turbulent concentric annular pipe flow has been studied in both physical and spectral spaces. In order to study the Reynolds number effects on the flow physics, two nominal Reynolds numbers are compared for $Re_{D_h} = 8900$ and 17700. The effects of domain size on the flow field are investigated based on a comparative study of 12 test cases (including one reference case) at the lower nominal Reynolds number. If we solely focus on the mean velocity profiles, it would be very tempting to conclude that the axial and azimuthal domain sizes of $L_z = \pi\delta$ and

Table 5.1: Summary of the minimum computational domain sizes required for performing DNS for accurate calculations of different types of turbulence statistics at the nominal Reynolds number of $Re_{D_h} = 8900$.

Criterion of turbulence statistics	Minimum domain sizes
Mean velocity	$L_z = \pi\delta$ and $L_\theta = \pi/6$
Reynolds stresses	$L_z = 6\pi\delta$ and $L_\theta = \pi/4$
Two-point correlations	$L_z = 6\pi\delta$ and $L_\theta = \pi/2$
1D and 2D premultiplied energy spectra	$L_z = 12\pi\delta$ and $L_\theta = 3\pi/4$

$L_\theta = \pi/6$ are sufficient for conducting DNS. However, based on an analysis of second-order statistical moments, it becomes apparent that the results of Reynolds stresses would not be accurate unless the minimum computational domain is extended to $L_z = 6\pi\delta$ and $L_\theta = \pi/4$. To determine if the computational domain is proper for capturing the length scales of energetic eddy motions, the 1D axial and azimuthal two-point correlation coefficients are examined, which indicate that the minimum computational domain needs to be kept at $L_z = 6\pi\delta$ and $L_\theta = \pi/2$. The study of the minimum computational domain size for conducting DNS is further refined by investigating the characteristic wavelengths of turbulent flow structures in the spectral space. It is observed that an adequate computational domain that allows for capturing the most energetic eddy motions is that of case B4 (i.e., $L_z = 12\pi\delta$ and $L_\theta = 3\pi/4$) based on the analysis of the 1D and 2D premultiplied spectra. Table 5.1 summarizes these results of minimum computational domains sizes required for accurately calculating turbulence statistics and for reproducing turbulence flow structures. As the nominal Reynolds number increases from $Re_{D_h} = 8900$ and 17700, the dimensional characteristic wavelengths of the most energetic streaky structures reduce, and in consequence, the minimum domain for properly performing DNS can be reduced to that of case D (i.e., $L_z = 8\pi\delta$ and $L_\theta = \pi/2$).

In the current literature, there has been some disagreement on whether the radial position corresponding to the maximum velocity collocates with that of the zero

mean shear stress in a turbulent concentric annular pipe flow. The inconsistency of the literature can now be concluded. Through a relatively simple approach, we show analytically that the radial positions of the maximum velocity and zero shear stress are, in fact, strictly collocated. This analytical result has been further validated using our DNS data.

Based on the aforementioned investigation of the minimum computational domain size, coherent flow structures of the concentric annular pipe flow are investigated at the lower nominal Reynolds number of $Re_{D_h} = 8900$. The scales of energetic turbulent flow motions such as near-wall streaks and hairpin structures are visualized using instantaneous and conditionally-averaged axial velocity fluctuations (u'_z), instantaneous axial vorticity (ω'_z) and swirling strength (λ_{ci}). The scales of these structures are further studied by examining the 1D axial and azimuthal two-point correlation coefficients, and 1D and 2D premultiplied energy spectra. The 2D energy spectra show that the both axial and azimuthal characteristic length scales of the near-wall streaks are larger on the convex side than on the concave side. This leads to an important conclusion that the challenge involved in accurately performing DNS of a concentric annular pipe flow mostly stems from the need of capturing large streaky structures on the convex side.

At a higher elevation of $\delta/2$ away from the walls, hairpin packets are dominant energy-containing structures. The scales of these structures are similar on both convex and concave sides of the concentric annular pipe with a mode of approximately $(\lambda_z^+, \lambda_\theta^+) = (405, 190)$. The cycle of the generation of PHV from SHV and destruction of PHV into DHV is observed by showing a side view of hairpin packets. The pattern of generation and destruction of hairpin packets can be identified precisely by studying the axial mode of the 1D or 2D premultiplied spectrum of axial velocity fluctuations, or vividly by displaying hairpin structures using the λ_{ci} criterion. The characteristic wavelength of either PHV or SHV is approximately 400 wall units, and therefore, the axial separation of the hairpin necks (of PHV and SHV) is typically

around 200 wall units. At $r^+ = 30$, there exist azimuthally-oriented vortex filaments, which connect hairpin legs and are the most energetic around this elevation. These azimuthally-oriented vortex filaments lay further away from the wall than the near-wall streaks, perturbed and pushed away by ejections to form hairpin arches at higher elevations. There is an interesting observation associated with the premultiplied 1D azimuthal energy spectrum $k_\theta^+ \tilde{E}_{\theta\theta}^+$ of case B5: although the azimuthal domain size is a full circle with $L_\theta = 2\pi$, the value of $k_\theta^+ \tilde{E}_{\theta\theta}^+$ does not decay to zero at the cutoff wavelength (after one period). This indicates that there are some low-energy turbulence structures with azimuthal periods that are larger than 2π .

5.1.2 The effects of radius ratio on turbulent concentric annular pipe flow and structures

The effects of radius ratio on the turbulence statistics and structures of concentric annular pipe flow have been studied in both physical and spectral spaces. Four test cases (of $R_i/R_o = 0.1, 0.3, 0.5$ and 0.7) are compared at a nominal Reynolds number of $Re_{D_h} = 8900$. To ensure that the most energetic turbulence structures are captured in DNS, the axial length of the pipe is set to $L_z = 12\pi\delta$, while the azimuthal domain size varies from $L_\theta = 2\pi$ to $\pi/2$ as the radius ratio increases from $R_i/R_o = 0.1$ to 0.7 . The radius ratio effects on the characteristics of the boundary layers developed over the inner and outer cylinder walls are investigated by examining the mean velocity, skin friction coefficient, boundary layer thickness, magnitudes and budget balance of Reynolds shear stress, and turbulent flow structures.

The curvature difference between the inner and outer cylinder walls vary with the radius ratio. The thicknesses of boundary layers developed over the inner and outer cylinder walls are calculated analytically and compared against the DNS data. It is concluded that the boundary layer thicknesses on the inner and outer cylinder sides are functions of radius ratio R_i/R_o and friction velocity ratio $u_{\tau i}/u_{\tau o}$. In general, the

boundary layer developed over the outer wall is thicker than that over the inner wall (i.e., $\delta_{to} > \delta_{ti}$). As the radius ratio increases, the curvature difference between the two cylinder surfaces reduces, and as a result, the difference between the values of δ_{ti} and δ_{to} and that between Re_{τ_i} and Re_{τ_o} decrease monotonically. The mean axial velocity profile $\langle u_z \rangle^+$ varies considerably with the radius ratio, and deviates from the familiar law-of-the-wall for a ZPG boundary layer over a flat plate. At the lowest radius ratio tested ($R_i/R_o = 0.1$), the logarithmic layer is apparently wider on the outer cylinder side than on the inner cylinder side, and the magnitude of Reynolds shear stress $-\langle u'_z u'_r \rangle^+$ is higher on the outer cylinder side than on the inner cylinder side. However, as the radius ratio value increases from $R_i/R_o = 0.1$ to 0.7, the profiles of both $\langle u_z \rangle^+$ and $-\langle u'_z u'_r \rangle^+$ become increasingly symmetrical, indicating that the degree of curvature difference between the two cylinder walls reduces. The transport equation of Reynolds shear stress is further investigated to study the interaction of boundary layers developed above the inner and outer cylinder surfaces. It is observed that the magnitudes of the dominant source and sink terms (i.e., the production term P_{zr} and velocity-pressure-gradient term Π_{zr} , respectively) are higher on the outer side than on the inner cylinder side. As the radius ratio increases from $R_i/R_o = 0.1$ to 0.7, the differences in the magnitudes of these two terms between the outer and inner cylinder side decrease, which is also a reflection of the fact that the curvature difference between the two cylinder walls reduces as the radius ratio increases.

The effects of radius ratio on the coherent flow structures are examined in physical and spectral spaces. The scales of energetic turbulent flow motions such as streamwise-elongated vortical structures and hairpin structures are visualized using time-averaged axial vorticity fluctuations ($\overline{\omega'_z}^+$) and instantaneous swirling strength (λ_{ci}). The scales of these structures are further studied by examining the 1D axial and azimuthal spectra of vorticity and velocity fluctuations. In the near-wall region (around $r^+ = 20$), streamwise vortical structures (or, streaks) dominate. It is observed that as the radius ratio increases from $R_i/R_o = 0.1$ to 0.7, the characteristic

length scale of streamwise vortical structures (as indicated by the axial mode of $k_z^+ \tilde{\phi}_z^+$) varies from $\lambda_z^+ = 200$ on the outer cylinder side to $\lambda_z^+ = 400$ on the inner cylinder side in the case of $R_i/R_o = 0.1$ in the near-wall region. In core turbulent regions at a higher elevation of $\delta_{ti}/2$ or $\delta_{to}/2$ away from the inner or outer cylinder wall, respectively, hairpin structures become dominant. In general, hairpin structures are less populated on the inner cylinder side than on the outer cylinder side. The hairpin structures are longer on the inner cylinder side than on the outer cylinder side at all radius ratios. As the radius ratio increases, the axial characteristic length scales of hairpin structure decreases monotonically on the inner cylinder side but increases on the outer cylinder side. The characteristic axial length scale of the hairpin structures as indicated by the axial mode of $k_z^+ \tilde{E}_{zz}^+$ varies from $\lambda_z^+ = 400$ on the cylinder outer side to $\lambda_z^+ = 700$ on the inner cylinder side in the case of $R_i/R_o = 0.1$. Meanwhile, the azimuthal mode of $k_\theta^+ \tilde{E}_{zz}^+$ does not vary significantly with the radius ratio, which occurs at $\lambda_\theta^+ = 200-300$. The energy level of the hairpin structures is lower on the inner cylinder side than on the other cylinder side. As the radius ratio increases, the difference in the energy level between the inner and outer cylinder sides reduces monotonically, which is a reflection of decreased curvature difference between the two cylinder walls.

5.1.3 Direct numerical simulation of turbulent heat transfer in concentric annular pipe flows

Turbulent heat transfer and thermal structures in a concentric annular pipe have been studied using DNS. In order to study the effects of radius ratio on turbulent heat transfer in a concentric annular pipe flow, four test cases (of $R_i/R_o = 0.1, 0.3, 0.5$ and 0.7) are compared at a nominal Reynolds number of $Re_{D_h} = 17700$. The radius ratio effects on the characteristics of the thermal boundary layers developed over the inner and outer cylinder walls are investigated by examining the first- and

second-order statistics of the temperature field, Nusselt number, thermal boundary layer thickness, temperature spectra, budget balance of temperature variance and turbulent heat fluxes, and axial and azimuthal characteristic length scales of turbulent thermal structures.

It is observed that the thicknesses of thermal boundary layers developed over the inner and outer cylinder walls are sensitive to the radius ratio. In general, the thermal boundary layer developed over the outer wall is thicker than that over the inner wall (i.e., $\delta_{to}^* > \delta_{ti}^*$). The mean temperature profile $\langle \Theta \rangle$ varies significantly with the radius ratio, and becomes increasingly asymmetric as the radius ratio decreases from $R_i/R_o = 0.7$ to 0.1. At the lowest radius ratio tested (i.e., at $R_i/R_o = 0.1$), the mean temperature profile on the inner cylinder side deviates significantly from the familiar logarithmic law; however, a logarithmic law holds well on the concave outer cylinder side. This is because the surface curvature is much smaller on the outer cylinder side, and as a result, the wall scaling behavior of the mean temperature on the outer cylinder side tends to be similar to that over a flat plate.

It is observed that the magnitudes of the RMS temperature Θ_{rms}^+ and axial turbulent heat flux $\langle u'_z \Theta' \rangle^+$ show a consistent pattern in all four test cases, which are larger on the outer cylinder side than on the inner cylinder side. Both Θ_{rms}^+ and $\langle u'_z \Theta' \rangle^+$ reach their maximum values at $r^+ \approx 15$, as a direct result of a large local turbulent production rate in the near-wall region. The investigation into the behaviors of the RMS temperature and turbulence heat fluxes is refined by examining the budget balance of the transport equations of temperature variance and turbulent heat fluxes. It is observed that in the transport process of the axial turbulent heat flux $\langle u'_z \Theta' \rangle$, the role of the pressure-temperature gradient term Π_z is to reduce the axial turbulent heat flux, especially in the logarithmic region. The magnitude of Π_z is larger on the outer cylinder side than on the inner cylinder side, and furthermore, it serves as the primary sink term that balances the production term P_z in the logarithmic region (for $r^+ > 40$).

The effects of radius ratio on the thermal structures associated with the turbulent temperature field are studied in both physical and spectral spaces. Both near-wall thermal streaks and TF structures at higher elevations are investigated. The characteristic length scales of thermal structures are quantified using both 1D and 2D pre-multiplied spectra of temperature fluctuations. In the near-wall region (of $r^+ = 15$), thermal streaky structures are dominant. It is observed that the streamwise characteristic length scale of thermal streaky structures (as indicated by the axial mode of $k_z^+ \tilde{E}_{\Theta\Theta}^+$) varies from $\lambda_z^+ \approx 800$ on the inner cylinder side to $\lambda_z^+ \approx 500$ on the outer cylinder side in the case of $R_i/R_o = 0.1$. However, in the case of $R_i/R_o = 0.7$, the streamwise characteristic length scales of thermal streaky structures are similar, which are approximately $\lambda_z^+ \approx 600$ – 700 on the inner and outer sides. These trends reflect the curvature difference between the inner and outer cylinder walls, which is the largest at $R_i/R_o = 0.1$ and the smallest at $R_i/R_o = 0.7$ among the four test cases. At a much higher elevation relatively far away from the inner or outer cylinder walls (specifically, at one-half the thermal boundary layer thicknesses, for $\delta_{ti}^* = \delta_{to}^* = 0.5$), the TF structures became dominant. The characteristic length scales of the TF structures vary from $(\lambda_z^+, \lambda_\theta^+) \approx (600, 280)$ on the inner side to $(\lambda_z^+, \lambda_\theta^+) \approx (450, 180)$ on the outer side in the case of $R_i/R_o = 0.1$. It is concluded that as a result of the curvature difference between the two cylinder walls, both axial and azimuthal characteristic length scales of the TF structures are larger on the inner cylinder side than on the outer cylinder side.

5.2 Future work

To continue the research work of this thesis, I have the following suggestions:

1. The effects of radius ratio on transport of Reynolds stresses in concentric annular pipe flow can be further studied in both physical and spectral spaces. In this thesis, the effect of radius ratio on the magnitude of Reynolds stresses has

been studied in Physical space. It would be interesting to study the underlying mechanism of the Reynolds stress transport processes in the wall-normal direction and wall-parallel directions by examining the budget balance terms of the Reynolds stresses in the spectral space.

2. The turbulent flow and heat transfer studied in this thesis were done at two low and moderate Reynolds numbers. The physical of the heat and fluid flow can be better understood by testing more Reynolds numbers to systematically study the Reynolds number effects on the heat and fluid flows.
3. In the turbulent heat transfer study, the temperature field has been treated as a passive scalar. It would be interesting to also test the buoyant effects on the turbulent velocity and temperature fields.
4. In the present research, the concentric annular pipe is stationary (fixed to the ground). In future studies, it would be interesting to investigate the effect of system rotation (about the axial center and the radial axis) on the turbulence statistics and coherent flow structures. In this proposal, the effects of Coriolis forces on the transport processes of the momentum and thermal energy are to be studied.

Bibliography

- Adrian, R. (1994). Stochastic estimation of conditional structure: a review. *Appl. Sci. Res.*, 53(3-4):291–303.
- Adrian, R. (2007). Hairpin vortex organization in wall turbulence. *Phys. Fluids*, 19(4):041301.
- Avsarkison, V., Hoyas, S., Oberlack, M., and García-Galache, J. P. (2014). Turbulent plane Couette flow at moderately high Reynolds number. *J. Fluid Mech.*, 751.
- Bagheri, E., Wang, B.-C., and Yang, Z. (2020). Influence of domain size on direct numerical simulation of turbulent flow in a moderately curved concentric annular pipe. *Phys. Fluids*, 32(6):065105.
- Blackburn, H. and Sherwin, S. J. (2004). Formulation of a Galerkin spectral element–Fourier method for three-dimensional incompressible flows in cylindrical geometries. *J. Comp. Phys.*, 197(2):759–778.
- Boersma, B. J. and Breugem, W.-P. (2011). Numerical simulation of turbulent flow in concentric annuli. *Flow Turbul. Combust.*, 86(1):113–127.
- Brighton, J. A. and Jones, J. B. (1964). Fully developed turbulent flow in annuli. *J. Basic Eng.*, 86(4):835–842.
- Canuto, C., Hussaini, M. Y., Quarteroni, A., Thomas Jr, A., et al. (2012). *Spectral Methods in Fluid Dynamics*. Springer Science & Business Media.

- Chen, C.-H. P. and Blackwelder, R. F. (1978). Large-scale motion in a turbulent boundary layer: a study using temperature contamination. *J. Fluid Mech.*, 89(1):1–31.
- Chernyshenko, S. I. and Baig, M. F. (2005). The mechanism of streak formation in near-wall turbulence. *J. Fluid Mech.*, 544:99–131.
- Chin, C., Ooi, A. S. H., Marusic, I., and Blackburn, H. M. (2010). The influence of pipe length on turbulence statistics computed from direct numerical simulation data. *Phys. Fluids*, 22(11):115107.
- Chung, S. Y., Rhee, G. H., and Sung, H. J. (2002). Direct numerical simulation of turbulent concentric annular pipe flow: Part 1: Flow field. *Int. J. Heat Fluid Flow*, 23(4):426–440.
- Chung, S. Y. and Sung, H. J. (2003). Direct numerical simulation of turbulent concentric annular pipe flow: Part 2: Heat transfer. *Int. J. Heat Fluid Flow*, 24(3):399–411.
- Fang, X. and Wang, B.-C. (2018). On the turbulent heat transfer in a square duct subjected to spanwise system rotation. *Int. J. Heat Fluid Flow*, 71:220–230.
- Fornberg, B. (1998). *A Practical Guide to Pseudospectral Methods*, volume 1. Cambridge University Press.
- Francisco, A., Hoyas, S., and Jezabel, P. M. (2018). DNS of thermal channel flow up to $Re_\tau = 2000$ for medium to low Prandtl numbers. *Int. J. Heat Fluid Flow*, 127:349–361.
- Fukuda, T. and Tsukahara, T. (2020). Heat transfer of transitional regime with helical turbulence in annular flow. *Int. J. Heat Fluid Flow*, 82:108555.
- Grossmann, S., Lohse, D., and Sun, C. (2016). High-Reynolds number Taylor-Couette turbulence. *Annu. Rev. Fluid Mech.*, 48:53–80.

- Heikal, M., Walklate, P., and Hatton, A. (1977). The effect of free stream turbulence level on the flow and heat transfer in the entrance region of an annulus. *Int. J. Heat Fluid Flow*, 20(7):763–771.
- Hoyas, S. and Jiménez, J. (2006). Scaling of the velocity fluctuations in turbulent channels up to $Re_\tau = 2003$. *Phys. Fluids*, 18(1):011702.
- Jiménez, J. (2012). Cascades in wall-bounded turbulence. *Annu. Rev. Fluid Mech.*, 44:27–45.
- Jiménez, J. and Moin, P. (1991). The minimal flow unit in near-wall turbulence. *J. Fluid Mech.*, 225:213–240.
- Kaneda, M., Yu, B., Ozoe, H., and Churchill, S. W. (2003). The characteristics of turbulent flow and convection in concentric circular annuli. Part I: flow. *Int. J. Heat Fluid Flow*, 46(26):5045–5057.
- Karniadakis, G. E., Israeli, M., and Orszag, S. A. (1991). High-order splitting methods for the incompressible Navier-Stokes equations. *J. Comp. Phys.*, 97(2):414–443.
- Kasagi, N., Tomita, Y., and Kuroda, A. (1992). Direct numerical simulation of passive scalar field in a turbulent channel flow. *J. Heat Trans.*, 114(3):598–606.
- Kays, W. and Leung, E. (1963). Heat transfer in annular passages—hydrodynamically developed turbulent flow with arbitrarily prescribed heat flux. *Int. J. Heat Fluid Flow*, 6(7):537–557.
- Kim, J., Moin, P., and Moser, R. (1987). Turbulence statistics in fully developed channel flow at low Reynolds number. *J. Fluid Mech.*, 177:133–166.
- Kleiser, L. and Schumann, U. (1980). Treatment of incompressibility and boundary conditions in 3-D numerical spectral simulations of plane channel flows. In *Conf. on Numer. Meth. in Fluid Mech.*, pages 165–173. Springer.

- Knudsen, J. G. and Katz, D. L. (1950). Velocity profiles in annuli. *in Proc. Midwes. Conf. on Fluid Dynamics*, pages 175–203, Univ. of Illinois, Michigan.
- Monty, J. P., Stewart, J. A., Williams, R. C., and Chong, M. S. (2007). Large-scale features in turbulent pipe and channel flows. *J. Fluid Mech.*, 589:147–156.
- Moser, R. D., Kim, J., and Mansour, N. (1999). Direct numerical simulation of turbulent channel flow up to $Re_\tau = 590$. *Phys. Fluids*, 11(4):943–945.
- Moser, R. D. and Moin, P. (1987). The effects of curvature in wall-bounded turbulent flows. *J. Fluid Mech.*, 175:479–510.
- Mujeeb, M. and Richard, P. (1981). A study of some turbulence models for flow and heat transfer in ducts of annular cross-section. *J. Heat Trans.*, 103(1):146–152.
- Neves, J. C., Moin, P., and Moser, R. D. (1994). Effects of convex transverse curvature on wall-bounded turbulence. Part 1. the velocity and vorticity. *J. Fluid Mech.*, 272:349–382.
- Nouri, J., Umur, H., and Whitelaw, J. (1993). Flow of Newtonian and non-Newtonian fluids in concentric and eccentric annuli. *J. Fluid Mech.*, 253:617–641.
- Orszag, S. A. and Patera, A. T. (1983). Secondary instability of wall-bounded shear flows. *J. Fluid Mech.*, 128:347–385.
- Ould-Rouiss, M., Redjem-Saad, L., and Lauriat, G. (2009). Direct numerical simulation of turbulent heat transfer in annuli: Effect of heat flux ratio. *Int. J. Heat Fluid Flow*, 30(4):579–589.
- Ould-Rouiss, M., Redjem-Saad, L., Lauriat, G., and Mazouz, A. (2010). Effect of Prandtl number on the turbulent thermal field in annular pipe flow. *Int. J. Heat Fluid Flow*, 37(8):958–963.

- Pallares, J. and Davidson, L. (2002). Large-eddy simulations of turbulent heat transfer in stationary and rotating square ducts. *Phys. Fluids*, 14(8):2804–2816.
- Quadrio, M. and Luchini, P. (2002). Direct numerical simulation of the turbulent flow in a pipe with annular cross section. *Eur. J. Mech. B.-Fluid*, 21(4):413–427.
- Rehme, K. (1974). Turbulent flow in smooth concentric annuli with small radius ratios. *J. Fluid Mech.*, 64(2):263–288.
- Robinson, S. K. (1991). Coherent motions in the turbulent boundary layer. *Annu. Rev. Fluid Mech.*, 23(1):601–639.
- Sanz-Serna, J. (1995). Fourier techniques in numerical methods for evolutionary problems. In *Third Granada Lectures in Computational Physics*, pages 145–200. Springer.
- So, R. M. and Mellor, G. L. (1973). Experiment on convex curvature effects in turbulent boundary layers. *J. Fluid Mech.*, 60(1):43–62.
- Taylor, G. I. (1923). Stability of a viscous liquid contained between two rotating cylinders. *Philos. Trans. Royal Soc. A*, 223(605-615):289–343.
- Taylor, G. I. (1936). Fluid friction between rotating cylinders, I-torque measurements. *Proc. Royal Soc. Lond.*, 157(892):546–564.
- Trefethen, L. N. (2000). *Spectral methods in MATLAB*. SIAM.
- Wilson, N. W. and Medwell, J. (1968). An analysis of heat transfer for fully developed turbulent flow in concentric annuli. *J. Heat Trans.*, 44:1185–1199.
- Wu, X., Baltzer, J., and Adrian, R. (2012). Direct numerical simulation of a 30R long turbulent pipe flow at $R^+ = 685$: large-and very large-scale motions. *J. Fluid Mech.*, 698:235–281.

Yang, Z. X. and Wang, B.-C. (2018). Capturing Taylor–Görtler vortices in a streamwise-rotating channel at very high rotation numbers. *J. Fluid Mech.*, 838:658–689.

Yu, B., Kawaguchi, Y., Kaneda, M., Ozoe, H., and Churchill, S. W. (2005). The computed characteristics of turbulent flow and convection in concentric circular annuli. Part ii. uniform heating on the inner surface. *Int. J. Heat Fluid Flow*, 48(3-4):621–634.

Appendix A

Computer Code and Numerical Algorithm

In order to conduct DNS of turbulent flow and heat transfer in a concentric annular pipe, a new computer code has been developed based on a highly-accurate pseudo-spectral method. This appendix describes the numerical algorithm for developing this computer code. FORTRAN 90/95 programming language is used to develop the computer code. The P3DFFT library is used to perform fast Fourier transform (FFT), and the message passing interface (MPI) libraries are employed to parallelize the computing processes.

Pseudo-spectral methods are highly-efficient and highly-accurate for solving the partial differential equations that govern the thermal fluid flows (Fornberg, 1998; Trefethen, 2000; Sanz-Serna, 1995). The pseudo-spectral methods are global, meaning that the solution at each node depends on all the other computational nodes. Comparatively speaking, the finite volume and finite difference methods are local and the solution at each point depends on the neighbouring nodes. Therefore, pseudo-spectral methods can achieve much higher accuracy than do the finite difference and finite volume methods, given the same number of grid points of a discretized domain. A wide range of pseudo-spectral methods (i.e. Galerkin, collocation, and tau methods) have

been utilized for numerical simulation of the turbulent flow and heat transfer in the literature. In this thesis, the collocation pseudo-spectral method is used for solving the governing equations.

There are many theoretical studies on implementing pseudo-spectral methods to study a turbulent plan-channel flow (Kleiser and Schumann, 1980; Kim et al., 1987). However, the number of works on implementing pseudo-spectral methods to investigate the turbulent flow in concentric-annular and circular-pipe is still lacking. The goal of this appendix is to present an accurate scheme for solving an incompressible flow confined within a concentric annular pipe.

The organization of this appendix is as follows: in Section A.1, the governing equations for compressible flow in cylindrical coordinates are presented. In Section A.2, the spatial discretizations of the velocity and pressure fields are presented in the physical and spectral spaces. In section A.3, the temporal discretizations are described. In section A.4, treatment of boundary conditions is implemented. In Section A.5, the results of a test case are compared against the reference data to validate the developed code. In Section A.6, the implementation of the P3DFFT library and result of a scaleability of study of the code are presented.

A.1 Test cases and numerical algorithm

Figure 4.1 shows the schematic diagram and coordinate system of the concentric annular flow under testing. Here z , θ , and r represent the axial, azimuthal and radial coordinates, respectively. Correspondingly, u_z , u_θ and u_r represent velocity components in these three directions. The fluid properties, including density and viscosity, are assumed to be constant. Hence, the temperature is considered to be a passive scalar. The continuity, momentum and thermal energy equations for an incompressible flow for a cylindrical coordinate system are expressed as

$$\nabla \cdot \vec{u} = 0 \quad , \quad (\text{A.1})$$

$$\frac{\partial \vec{u}}{\partial t} + \vec{u} \cdot \nabla \vec{u} = -\frac{1}{\rho} \nabla p + \nu \nabla^2 \vec{u} - \frac{\Pi}{\rho} \hat{\mathbf{e}}_z \quad , \quad (\text{A.2})$$

$$\frac{\partial \Theta}{\partial t} + \vec{u} \cdot \nabla \Theta = u_z \frac{dT_w}{dz} + \alpha \nabla^2 \Theta \quad . \quad (\text{A.3})$$

Here \vec{u} , p , ρ , ν and α represent the velocity vector, pressure, density, kinematic viscosity and thermal diffusivity of the fluid, respectively. In equations (A.2), $\hat{\mathbf{e}}_z$ is the base unit vector of the z -direction, with $|\hat{\mathbf{e}}_z| \equiv 1$. In equations (A.2) and (A.3), Π and dT_w/dz denote the constant mean axial pressure gradient that drives the flow, and the mean axial wall-temperature gradient characteristic of surface heating under a constant surface heat flux condition. Here, $T_w = T_w(z)$ represents the local mean wall temperature of the inner and outer cylinder surfaces at a given axial position, and $\Theta = T - T_w$ is the excess temperature relative to T_w . By definition, $\Theta \equiv 0$ holds at the walls.

As shown in Fig. 4.1, the flow is fully developed both hydraulically and thermally. No-slip boundary conditions are enforced at the cylinder walls for the velocity field. Periodic boundary conditions are applied in the axial and azimuthal directions for both the velocity field and the excess temperature (Θ) field. This treatment method for the temperature field is similar to that used in the numerical studies of turbulent heat transfer in rotating square duct flows by Pallares and Davidson (2002) and Fang and Wang (2018). Given a uniform surface heat flux boundary condition ($\dot{q}_w = \dot{q}_{wi} = \dot{q}_{wo}$), both the bulk mean temperature (T_b) and the local mean peripheral temperature of the wall ($\langle T_w \rangle$) increase linearly in the axial direction at a same constant rate (i.e., $dT_w/dz = dT_b/dz$). Furthermore, for a thermally fully developed flow, the excess temperature Θ is invariant along the axial direction such that $dT_w/dz = d\langle T \rangle/dz$. The mean axial wall-temperature gradient can be evaluated by applying the principle of energy conservation to a differential control volume to obtain

$$\frac{d\langle T \rangle}{dz} = \frac{dT_b}{dz} = \frac{dT_w}{dz} = \frac{2(\dot{q}_{wi}R_i + \dot{q}_{wo}R_o)}{\rho C_p U_b (R_o^2 - R_i^2)} \quad . \quad (\text{A.4})$$

where, C_p is the specific heat of the fluid under constant pressure and U_b is the bulk mean velocity.

A.2 Spatial discretization

For the pseudo-spectral method code, Fourier series are applied to the streamwise and azimuthal directions and the Legendre polynomials are used the wall-normal direction to expand the velocity, pressure, and temperature fields. The Fourier transform converts a velocity, pressure, and temperature field from a space domain representation to a frequency domain representation as

$$\hat{u}(k_z, k_\theta, r, t) = \frac{1}{N_z N_\theta} \sum_{-N_z/2}^{N_z/2-1} \sum_{-N_\theta/2}^{N_\theta/2-1} u(z, \theta, r, t) e^{-i(k_z z + k_\theta \theta)}, \quad (\text{A.5})$$

where $i = \sqrt{-1}$ indicates the imaginary unit, and $k_z = n_1 k_{0z}$ and $k_\theta = n_1 k_{0\theta}$ are the streamwise and azimuthal wavenumbers, respectively. Here, $n_z \in [-N_z/2, N_z/2 - 1]$ and $n_\theta \in [-N_\theta/2, N_\theta/2 - 1]$ are two integers, and $k_{0z} = 2\pi/L_z$ and $k_{0\theta} = 2\pi/L_\theta$ are the lowest wavenumbers. In practice, only a finite number of modes are retained in the calculation, and the conjugate-symmetric property of the Fourier transforms of real variables (Canuto et al., 2012) is exploited, so that the negative-k modes are not required. The corresponding inversion formula for the velocity field is

$$u_k(z, \theta, r, t) = \sum_{-N_z/2}^{N_z/2-1} \sum_{-N_\theta/2}^{N_\theta/2-1} \hat{u}_k(k_z, k_\theta, r, t) e^{i(k_z z + k_\theta \theta)} \quad . \quad (\text{A.6})$$

Using Fourier series in wall parallel directions, spatial derivatives in z and θ directions can be obtained by differentiating equation (A.5) with respect to z and θ . The derivative of a function ϕ_n in the wall-normal direction can be written as

$$\frac{\partial \phi_i}{\partial r} = \sum_{j=0}^{n_r} D_{ij} \phi_j \quad , \quad (\text{A.7})$$

where matrix D is known as the (Chebyshev) derivative matrix.

An explicit form of $n_r \times n_r$ matrix of D is given in Trefethen (2000) , which follows

$$c_i = \begin{cases} 2 & \text{for } i = 0 \text{ or } n_r \\ 1 & \text{for } 1 \leq i \leq n_r - 1 \end{cases} , \quad (\text{A.8})$$

$$D_{00} = \frac{2n_r^2 + 1}{6} , \quad (\text{A.9a})$$

$$D_{n_r n_r} = -\frac{2n_r^2 + 1}{6} , \quad (\text{A.9b})$$

$$D_{ii} = -\frac{-x_i}{2(1 - x_i^2)} \text{ for } 1 \leq i \leq n_r - 1 , \quad (\text{A.9c})$$

$$D_{ij} = \frac{c_i (-1)^{i+j}}{c_j x_i - x_j} \text{ for } i \neq j . \quad (\text{A.9d})$$

A.3 Temporal discretization

The high-order splitting method developed by Karniadakis et al. (1991) is used for the time integration. The governing equations of velocity components (equations (A.2)) can be presented alternatively in the following form,

$$\frac{\partial \vec{u}}{\partial t} + \mathbf{N}(\vec{u}) = -\frac{1}{\rho} \nabla p + \nu \mathbf{L}(\vec{u}) + -\frac{\Pi}{\rho} \hat{\mathbf{e}}_z . \quad (\text{A.10})$$

Here, $\mathbf{L}(\vec{u})$ and $\mathbf{N}(\vec{u})$ represent the linear viscous and non-linear advection terms, respectively. The governing equations of the temperature field can also be written in the same format as,

$$\frac{\partial \Theta}{\partial t} + \mathbf{N}(\Theta) = \alpha \mathbf{L}(\Theta) + u_z \frac{dT_w}{dz} . \quad (\text{A.11})$$

The velocity, pressure, and excess temperature are decoupled using a time-splitting scheme, which consists of the following three sub-steps,

$$\hat{u}^* - \sum_{q=0}^2 \alpha_q \hat{u}^{n-q} = \Delta t \sum_{q=0}^2 \beta_q N(\hat{u}^{n-q}) , \quad (\text{A.12})$$

Table A.1: Scheme coefficient.

β_0	β_1	β_2	α_0	α_1	α_2
3	-3	1	3	-3/2	1/3

$$\hat{\Theta}^* - \sum_{q=0}^2 \alpha_q \hat{\Theta}^{n-q} = \Delta t \sum_{q=0}^2 \beta_q N(\hat{\Theta}^{n-q}) \quad , \quad (\text{A.13})$$

$$\hat{u}^{**} = \hat{u}^* - \Delta t \nabla \hat{p}^{n+1} \quad , \quad (\text{A.14})$$

$$\hat{\Theta}^{**} = \hat{\Theta}^* + \Delta t (u_z^{**} \frac{dT_w}{dz}) \quad , \quad (\text{A.15})$$

$$\hat{u}^{n+1} = \frac{6}{11} (\hat{u}^{**} - \Delta t \nu L(\hat{u}^{n+1})) \quad , \quad (\text{A.16})$$

$$\hat{\Theta}^{n+1} = \frac{6}{11} (\hat{\Theta}^{**} - \Delta t \alpha L(\hat{\Theta}^{n+1})) \quad . \quad (\text{A.17})$$

where \hat{u}^* , $\hat{\Theta}^*$, \hat{u}^{**} and $\hat{\Theta}^{**}$ are intermediate velocity and excess temperature fields defined in equations (A.12-A.17). The superscript index n refers to time level. The weight coefficients α_q and β_q for a 3rd order scheme are given in Table A.1.

Let, $\mathbf{N}(\vec{u})$ represent the Fourier transform of advection terms. The non-linear terms are calculated at the first step with no boundary condition. In the first step, non-linear terms are calculated explicitly. They are taken in the form of a skew-symmetric formulation based on the proposal of Karniadakis et al. (1991) in order to minimize aliasing effects. The skew-symmetric form is the most tolerable for the aliasing errors and the most expensive to compute. The non-linear terms are calculated using the convective and divergence forms alternatively, which is commonly known to be a good compromise between stability and computational cost (Blackburn and Sherwin, 2004). The convective form of non-linear terms in the cylindrical coordinates read

$$\mathbf{N}(\vec{u}) = \vec{u} \cdot \nabla \vec{u} = \begin{bmatrix} u_z \frac{\partial u_z}{\partial z} + u_r \frac{\partial u_z}{\partial r} + \frac{u_\theta}{r} \frac{\partial u_z}{\partial \theta} \\ u_z \frac{\partial u_\theta}{\partial z} + u_r \frac{\partial u_\theta}{\partial r} + \frac{u_\theta}{r} \frac{\partial u_\theta}{\partial \theta} + \frac{u_r u_\theta}{r} \\ u_z \frac{\partial u_r}{\partial z} + u_r \frac{\partial u_r}{\partial r} + \frac{u_\theta}{r} \frac{\partial u_r}{\partial \theta} - \frac{u_\theta u_\theta}{r} \end{bmatrix} \quad , \quad (\text{A.18})$$

and the divergence form of non-linear terms in the cylindrical coordinates is read

$$\mathbf{N}(\vec{u}) = \nabla \cdot \vec{u}\vec{u} = \begin{bmatrix} \frac{\partial u_z u_z}{\partial z} + \frac{\partial u_r u_z}{\partial r} + \frac{1}{r} \frac{\partial u_z u_\theta}{\partial \theta} + \frac{u_z u_z}{r} \\ \frac{\partial u_z u_\theta}{\partial z} + \frac{\partial u_r u_\theta}{\partial r} + \frac{1}{r} \frac{\partial u_\theta u_\theta}{\partial \theta} + \frac{2u_r u_\theta}{r} \\ \frac{\partial u_z u_r}{\partial z} + \frac{\partial u_r u_r}{\partial r} + \frac{1}{r} \frac{\partial u_r u_\theta}{\partial \theta} + \frac{u_r u_r - u_\theta u_\theta}{r} \end{bmatrix} . \quad (\text{A.19})$$

$\hat{\mathbf{u}}^{**}$ satisfies the incompressibility constraint, thus

$$\nabla \cdot \hat{\mathbf{u}}^{**} = 0 \quad . \quad (\text{A.20})$$

This velocity field should also satisfy the no-slip boundary condition in the wall-normal direction. Therefore,

$$\hat{\mathbf{u}}^{**} \cdot \hat{\mathbf{e}}_r = 0 \quad . \quad (\text{A.21})$$

Incorporating these assumptions into Eq. (A.14), a separately solvable elliptic equation for the pressure with Neumann boundary conditions is obtained,

$$\nabla^2 \hat{p}^{n+1} = \nabla \cdot \left(\frac{\hat{\mathbf{u}}^*}{\Delta t} \right) \quad , \quad (\text{A.22})$$

$$\frac{\partial \hat{p}^{n+1}}{\partial r} = 0 \quad . \quad (\text{A.23})$$

The final field $\hat{\mathbf{u}}^{n+1}$ is obtained by solving the Helmholtz equation Eq. A.16 with $\hat{\mathbf{u}}^{**}$ acting as a forcing term. The linear viscous term of the Fourier transformed momentum equation (A.2) can now be written as

$$\mathbf{L}(\hat{\mathbf{u}}) = \nabla^2 \hat{\mathbf{u}} = \begin{bmatrix} (-k_z^2 - \frac{k_\theta^2}{r^2} + \frac{1}{r} \frac{\partial}{\partial r} + \frac{\partial^2}{\partial r^2}) \hat{u}_z \\ (-k_z^2 - \frac{k_\theta^2 + 1}{r^2} + \frac{1}{r} \frac{\partial}{\partial r} + \frac{\partial^2}{\partial r^2}) \hat{u}_\theta - \nu \frac{2ik_\theta}{r^2} \hat{u}_r \\ (-k_z^2 - \frac{k_\theta^2 + 1}{r^2} + \frac{1}{r} \frac{\partial}{\partial r} + \frac{\partial^2}{\partial r^2}) \hat{u}_r - \nu \frac{2ik_\theta}{r^2} \hat{u}_\theta \end{bmatrix} . \quad (\text{A.24})$$

Note the coupling of $L(\hat{u}_\theta)$ with $L(\hat{u}_r)$ in the viscous terms of Eq. (A.24). it arises through taking a divergence of the viscous stress tensor in cylindrical coordinates. The variables are related as

$$\tilde{u}_r = \hat{u}_r + i\hat{u}_\theta, \quad \tilde{u}_\theta = \hat{u}_r - i\hat{u}_\theta, \quad \tilde{u}_z = \hat{u}_z \quad , \quad (\text{A.25})$$

which can be used to diagonalise the linear terms (Orszag and Patera, 1983). The diagonalised equations can therefor be presented as follows:

$$\frac{\partial \hat{u}_z}{\partial t} + N(\hat{u}_z) = -\frac{ik_\theta}{\rho} \hat{p} + \nu L(\hat{u}_z) \quad , \quad (\text{A.26})$$

$$\frac{\partial \tilde{u}_\theta}{\partial t} + N(\tilde{u}_\theta) = -\frac{1}{\rho} \left(\frac{\partial \hat{p}}{\partial r} - k_\theta \frac{\hat{p}}{r} \right) + \nu L(\tilde{u}_\theta) \quad , \quad (\text{A.27})$$

$$\frac{\partial \tilde{u}_r}{\partial t} + N(\tilde{u}_r) = -\frac{1}{\rho} \left(\frac{\partial \hat{p}}{\partial r} + k_\theta \frac{\hat{p}}{r} \right) + \nu L(\tilde{u}_r) \quad , \quad (\text{A.28})$$

$$ik_z \hat{u}_z + \frac{\partial \hat{u}_r}{\partial r} + \frac{\hat{u}_r}{r} + \frac{ik_\theta \hat{u}_\theta}{r} = 0 \quad . \quad (\text{A.29})$$

A.4 Implementation of boundary conditions

The velocity, pressure, and temperature fields are periodic in the streamwise and azimuthal directions. However, in the wall-normal direction the Dirichlet boundary condition is applied to the velocity and temperature fields, and Nuemann boundary condition is applied to the pressure field. In the steamwise and azimuthal directions, periodic boundary condition can be satisfied naturally through Fourier transform to discretize the variables. However, in wall-normal direction, a special treatment is required to impose the Dirichlet boundary condition on the velocity and temperature fields and Nuemann boundary condition on the pressure field. Here, detailed treatment methods are presented. However, for the sake of brevity, only detailed treatment of u_z in terms of the Dirichlet boundary condition is presented, and the same treatment method extends to u_θ , u_r , and Θ .

Considering Eq. (A.22), the coefficient matrix of pressure at given k_z and k_θ reads

$$CP = D^2 + \text{diag}(1/r) \times D + \text{diag}(k_z^2 + \frac{k_\theta^2}{r^2}) \quad (\text{A.30})$$

Here, CP is a coefficient matrix of the pressure solver, $\text{diag}(\cdot)$ denotes a diagonal matrix, and D is the (Chebyshev) derivative matrix that was previously defined by

Eq. (A.9). Based on the intermediate velocity \hat{u}^* given by Eq. (A.12), the right hand side (RHS) of Eq. (A.22) at arbitrary wave numbers k_z and k_θ reads

$$RP = D \times \hat{u}_r^* + \text{diag}(1/r) \times \hat{u}_r^* + \text{diag}(ik_z) \times \hat{u}_z^* + \text{diag}\left(\frac{ik_\theta}{r}\right) \times \hat{u}_\theta^* \quad . \quad (\text{A.31})$$

Here, RP is the RHS vector of pressure solver. To impose the Neumann boundary condition the first and last rows of CP and RP should modified as follow,

$$\begin{bmatrix} D_{1,1} & D_{1,2} & \cdots & D_{1,nz-1} & D_{1,nz} \\ CP_{2,1} & CP_{2,2} & \cdots & CP_{2,nz-1} & CP_{2,nz} \\ \vdots & \vdots & \ddots & \vdots & \vdots \\ CP_{nz-1,1} & CP_{nz-1,2} & \cdots & CP_{nz-1,nz-1} & CP_{nz-1,nz} \\ D_{nz,1} & D_{nz,2} & \cdots & D_{nz,nz-1} & D_{nz,nz} \end{bmatrix} \begin{bmatrix} \hat{p}(r_1) \\ \hat{p}(r_2) \\ \vdots \\ \hat{p}(r_{nz-1}) \\ \hat{p}(r_{nz}) \end{bmatrix} = \begin{bmatrix} 0 \\ RP(r_2) \\ \vdots \\ RP(r_{nz-1}) \\ 0 \end{bmatrix} \quad . \quad (\text{A.32})$$

Using the linear solver provided by the LAPACK library, Eq. (A.32), the pressure field with a specific boundary condition can be obtained.

Considering Eq. (A.16), the coefficient matrix of streamwise velocity (\hat{u}_z^{n+1}) at given k_z and k_θ reads

$$CV = I + \frac{6}{11} \cdot \Delta t \cdot \nu \cdot (D^2 + \text{diag}(1/r) \times D + \text{diag}(-k_z^2 - \frac{k_\theta^2}{r^2})) \quad . \quad (\text{A.33})$$

Here, CV is a coefficient matrix of the streamwise velocity solver. Once the intermediate velocity \hat{u}^{**} is obtained from Eq. (A.14), the streamwise velocity at given k_z and k_θ reads

$$RV = \frac{6}{11} \hat{u}_z^{**} \quad , \quad (\text{A.34})$$

where RV is the RHS vector of the streamwise velocity solver. To impose no-slip boundary condition on the streamwise velocity field, the first and last rows of CV and RV are modified as follows:

$$\begin{bmatrix} 1 & 0 & \cdots & 0 & 0 \\ CV_{2,1} & CV_{2,2} & \cdots & CV_{2,nz-1} & CV_{2,nz} \\ \vdots & \vdots & \ddots & \vdots & \vdots \\ CV_{nz-1,1} & CV_{nz-1,2} & \cdots & CV_{nz-1,nz-1} & CV_{nz-1,nz} \\ 0 & 0 & \cdots & 0 & 1 \end{bmatrix} \begin{bmatrix} \hat{u}(r_1) \\ \hat{u}(r_2) \\ \vdots \\ \hat{u}(r_{nz-1}) \\ \hat{u}(r_{nz}) \end{bmatrix} = \begin{bmatrix} 0 \\ RV(r_2) \\ \vdots \\ RV(r_{nz-1}) \\ 0 \end{bmatrix} \quad . \quad (\text{A.35})$$

Then with the linear solver provided by the LAPACK library, the streamwise velocity field with a specific boundary condition can be obtained.

A.5 Validation based on concentric annular pipe with $R_i/R_o = 0.5$

The new pseudo-spectral code has been validated based on the test case of turbulent concentric annular pipe flow at $Re_{D_h} = 8900$ and $Pr = 0.71$, and the results are compared against the DNS data of Chung et al. (2002) and Kasagi et al. (1992). The numerical simulations were set up under the condition of a constant mean streamwise pressure gradient, which can be determined as

$$\Pi = -\frac{2(\tau_{wi}R_i + \tau_{wo}R_o)}{(R_o^2 - R_i^2)} . \quad (\text{A.36})$$

In the above equation, the values of τ_{wi} and τ_{wo} can be further determined based on the values the skin friction coefficients (C_{fi} and C_{fo}) at the inner the outer cylinder walls, respectively. In order to set up the numerical simulation, we used the skin friction coefficient values given in the DNS study of Chung et al. (2002) for Reynolds number case of $Re_{D_h} = 8900$, which is $C_{fi} = 0.00941$ and $C_{fo} = 0.00849$ at the inner and outer cylinder walls, respectively. From equation (A.36), it is straightforward that the value of the mean streamwise pressure gradient can be alternatively determined as $\Pi = -C_f \rho U_b^2 / (R_o - R_i)$, based on the averaged friction coefficient defined as $C_f = C_{fi}R_i / (R_i + R_o) + C_{fo}R_o / (R_i + R_o)$. The value of C_f can be also estimated from the empirical equation given by Nouri et al. (1993), i.e. $C_f = 0.36(Re_{D_h})^{-0.39}$. Test runs were conducted and minor adjustments to the value of Π were made to ensure that the value of Re_{D_h} calculated from DNS converges to its nominal value within a reasonable range of error tolerance. The numerical setup parameters are summarized in table A.2, . For this particular test case, the domain size is $L_z \times L_\theta \times L_r = 6\pi\delta \times \pi/2 \times 2\delta$, and a total number of grids of $N_z \times N_\theta \times N_r = 192 \times 128 \times 64$ are used in the z -, θ - and

Table A.2: Summary of test cases and grid resolutions. The nominal Reynolds number is $Re_{D_h} = 8900$ for the C and Ca test cases.

Case	$L_z \times L_\theta \times L_r$	Δz^+	$(R_i \Delta \theta)^+$	$(R_o \Delta \theta)^+$	Δr_{\min}^+	Δr_{\max}^+
C	$6\pi\delta \times \pi/2 \times 2\delta$	14.422	3.607	7.215	0.180	7.377

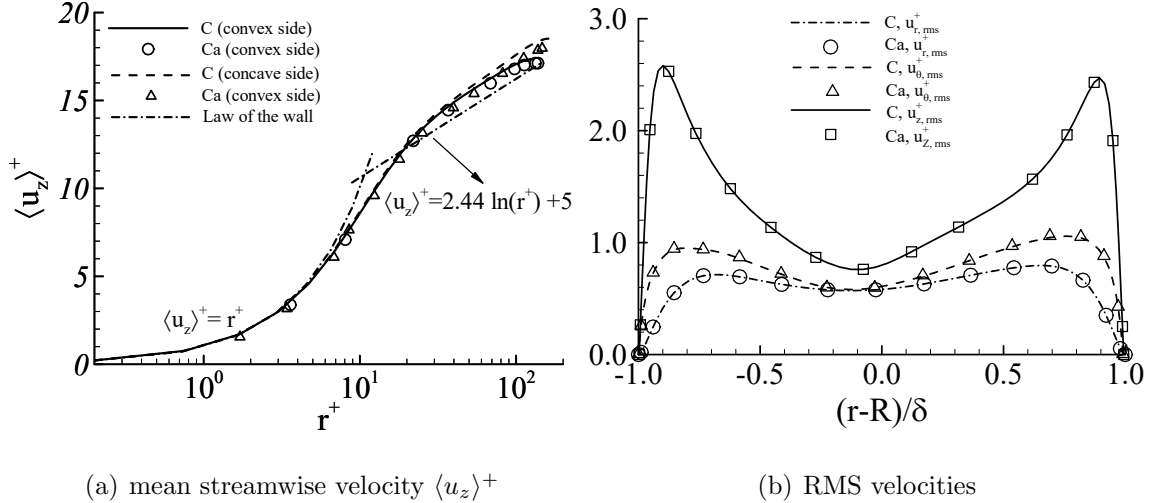


Figure A.1: Comparison of wall-normal profile of mean velocity and Reynolds normal stress against the DNS results by Chung et al. (2002), labeled as the case of Ca.

r - directions, respectively.

Figure A.1 compares the profiles of mean velocity and Reynolds normal stress against DNS data of Chung et al. (2002). Figure A.2 compares the profiles of mean temperature of the inner and outer sides against DNS data of Chung et al. (2002). In both figures A.1(a) and A.1(b), the DNS data set of Chung et al. (2002) is labeled as the case Ca. Also, the root mean square (RMS) of temperature fluctuations is compared against DNS results of Kasagi et al. (1992), labeled as the case Cb. The boundary condition used for the temperature fluctuation in the study of Chung et al. (2002) is zero gradients at wall, while in this study we used zero temperature fluctuation at the walls. More recent studies of heat transfer consider zero temperature fluctuations at the walls, such as the study of Kasagi et al. (1992), which the produced results by the code are compared against it. Here, the RMS of fluctuating

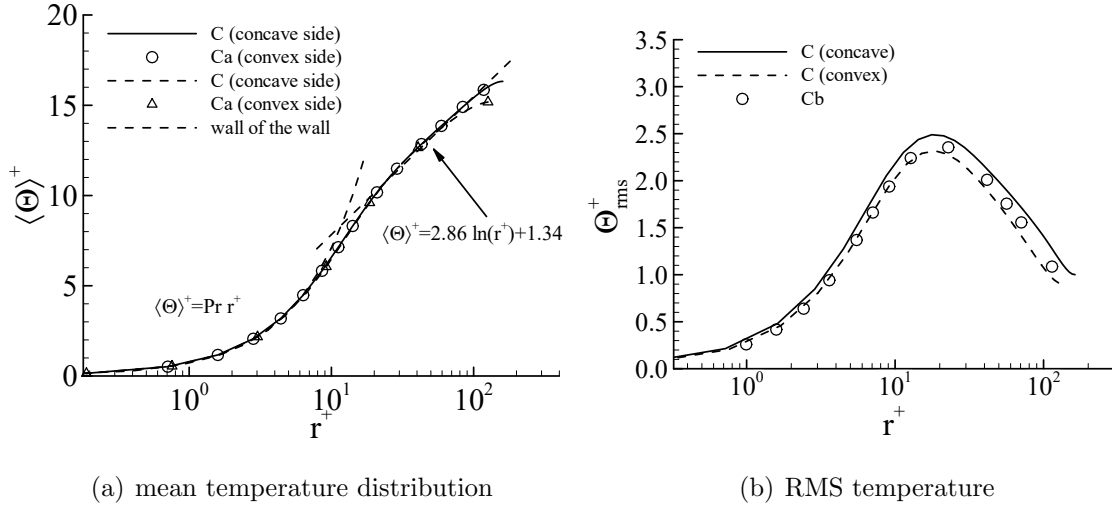


Figure A.2: Comparison of wall-normal profile of mean velocity and Reynolds normal stress against the DNS results by Chung et al. (2002)

temperature is compared against DNS data of Kasagi et al. (1992), which used the same boundary condition we used for a channel flow with iso-flux heating at the walls. A good agreement between the results from the current pseudo-spectral code and the reference data is apparent. Based on the above results, it is concluded that the pseudo-spectral code developed in this thesis has been validated and can be used for DNS simulation.

A.6 Implementation of the P3DFFT library

In this thesis, the P3DFFT library is used for performing of Fast Fourier Transformation (FFT) in a three dimensional space (3D). With the employment of P3DFFT, data can be transformed forward (real-to-complex) and backward (complex-to-real) in a 3D space. The P3DFFT library consists of three major components: initialization, array decomposition, , and forward (real-to-complex) and backward (complex-to-real) 3D Fourier transforms.

The P3DFFT library uses MPI library for communication between processors.

Before initializing the P3DFFT library, the MPI library should be initialized. Fortran programs use include “mpif.h” to define various constants and variables that are necessary in every MPI Fortran program. The following code with abundant comments shows how to initialize the MPI library.

```
1  include 'mpif.h'
2
3  call MPI_INIT (ierr)
4  call MPI_COMM_SIZE (MPI_COMM_WORLD, nproc, ierr)
5  call MPI_COMM_RANK (MPI_COMM_WORLD, proc_id, ierr)
```

The call to `MPI_INIT` is required in every MPI program and must be the first MPI call. It establishes the MPI “environment”, and its only argument is an error status. The call `MPI_COMM_SIZE` returns `nproc`, the number of processes that the user has started for this program. `MPI_COMM_WORLD` is the default communicator, which defines a set of rules that dictates how processors can communicate with each other. `MPI_COMM_WORLD` is one of the items defined in “mpif.h”. By calling `MPI_COMM_RANK`, each process finds out its rank in the group associated with a communicator. Thus, although each process in this program will get the same number in `nprocs`, each will have a different number for `proc_id`.

Only after initializing the MPI library, can the P3DFFT library be initialized. The following code with abundant comments shows how to initialize the P3DFFT library.

```
1  ! INITIALIZE P3DFFT
2
3  use p3dfft
4
5  ! nproc = total number of processors
6  dims(1) = nint(sqrt(real(nproc)))
7  dims(2) = dims(1)
8
9  ! Send dims, nx, ny, nz to p3dfft and get array dimensions (
```

Table A.3: Arguments of `p3dfft_setup`.

Arguments	intent	Descriptions
<code>dims</code>	Input	An array of two integers, specifying how the processor grid should be decomposed.
<code>nx, ny, nz</code>	Input	(Integer) Dimensions of the 3D transform (also the global grid dimensions).

```

10   istart, iend, fstart, fend) and size of each array (isize, fsize)
11   call p3dfft_setup (dims, nx, ny, nz, MPI_COMM_WORLD)
12   call p3dfft_get_dims (istart, iend, isize, 1)
    call p3dfft_get_dims (fstart, fend, fsize, 2)

```

The number of `nprocs` specified must be even (except if one core is used) as a square root (i.e., $nprocs = i^2, i \in \mathbb{Z}$). The required arguments to call `p3dfft_setup` are explained in Table A.3.

The `p3dfft_setup` routine sets up a two-dimensional (2D) array decomposition. P3DFFT employs 2D block decomposition whereby processors are arranged into a 2D grid $dims(1) \times dims(2)$, based on their MPI rank. Two dimensions of the 3D grid are block-distributed across the processor grid, by assigning the blocks to tasks in the rank order. The third dimension of the grid remains undivided, i.e. contained entirely within local memory (see Fig. A.3). This scheme is sometimes called pencil decomposition. A block decomposition is defined by dimensions of the local portion of the array contained within each task, as well as the beginning and ending indices for each dimension defining the array's location within the global array. This information is returned by `p3dfft_get_dims` routine.

The data are decomposed in z-pencil (see Fig. A.3(b)) in the real physical space, this will allow each processor to have access to data in the wall-normal direction, which is needed to perform differentiation (i.e., $\partial/\partial r$). The forward transform (real-to-complex) takes the array and transposes it into x-pencil (x -direction in computational space, see Fig. A.3(a)) to perform differentiation in the wall-parallel directions

Table A.4: Arguments of `p3dfft_get_dims(start, end, size, ip)`.

Arguments	Intent	Descriptions
<code>start</code>	output	An array containing 3 integers, defining the beginning indices of the local array for the given task within the global grid.
<code>end</code>	output	An array containing 3 integers, defining the ending indices of the local array within the global grid.
<code>size</code>	output	An array containing 3 integers, defining the local array's dimensions.
<code>ip</code>	input	<code>ip=1</code> : "Original": a "real space" array of real numbers <code>ip=2</code> : "Transposed": a "complex space" array of real numbers

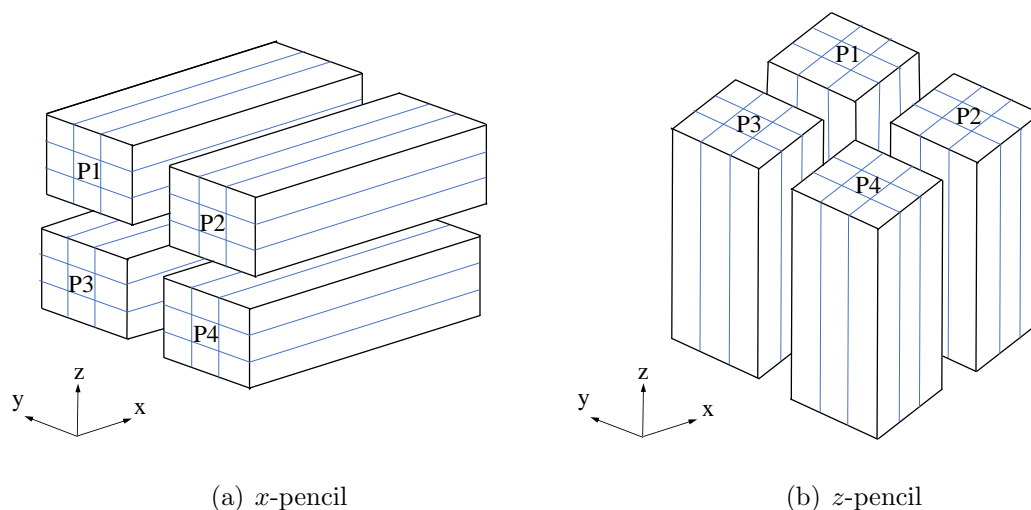


Figure A.3: The pencil decomposition of data.

(i.e. $\partial/\partial z$ or $\partial/\partial\theta$). The backward (complex-to-real) transform takes the array in a transposed form and produces a real array in the original form.

A block decomposition is defined by dimensions of the local portion of the array contained within each task, as well as the beginning and ending indices for each dimension for defining the array's location within the global array. This information is returned by `p3dfft_get_dims` routine. The required arguments to call `p3dfft_get_dims`, in order of appearance, are explained in Table A.4.

Table A.5: Arguments of `p3dffft_ftran_r2c` (`in`, `out`, `opt`).

Arguments	Intent	Descriptions
<code>in</code>	input	array of complex number
<code>out</code>	output	array of complex number
<code>opt</code>	input	a 3- letter character string indicating the type of transform desired. array's dimensions.

Table A.6: Arguments of `p3dffft_ftran_c2r` (`in`, `out`, `opt`).

Arguments	Intent	Descriptions
<code>in</code>	input	array of complex number
<code>out</code>	output	array of real number
<code>opt</code>	input	a 3- letter character string indicating the type of transform desired.

Forward transform is implemented by calling `p3dffft_ftran_r2c` (`in`, `out`, `opt`) subroutine. The required arguments to call `p3dffft_ftran_r2c` are explained in Table A.5. The key point to use this subroutine currently is choosing a correct option. In order to perform Fourier transform in wall parallel directions (i.e., z - and θ - directions in physical space, or x and y directions in computational space) and no transformation in z direction `opt='nff'`. Backward transform is implemented by calling `p3dffft_ftran_c2r` (`in`, `out`, `opt`) subroutine as explained in Table A.6. In order to correctly perform backward transform, the option argument (`opt`) should be same as the one chosen for `p3dffft_ftran_r2c` (`opt='nff'`).

A.7 Scalability of the code

The scalability of a parallel code (or, speedup) can be evaluated using the equation $Speedup = T_1/T_N$, where T_1 is the execution time of the code on one processor and T_N

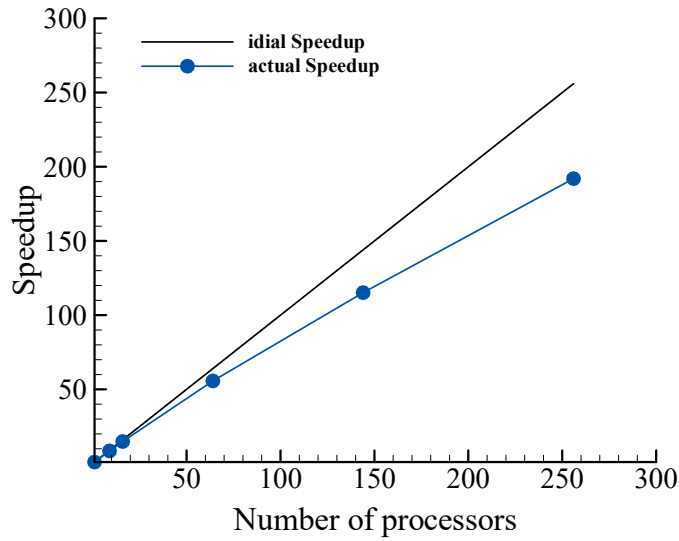


Figure A.4: Scalability of the parallel code obtained on the WestGrid (Orcinus) server.

is the execution time running on N processors. The test case is selected to assess the performance of the code is similar to case C presented in Table A.2. The preliminary speedup based on result 1 to 256 computer cores are shown in Fig. A.4. The perfect speedup corresponds to a 1-to-1 speedup is presented for a better comparison. The results show that the code scales fairly well upto at least 256 processors. The speedup is close to linear and does not exhibit a limiting value or a negative slope.